Advances in Optics and Photonics

Subwavelength interference of light on structured surfaces

XIANGANG LUO,[1,6] DINPING TSAI,[2,3,7] MIN GU,[4,8] AND MINGHUI HONG[5,9]

[1]State Key Laboratory of Optical Technologies on Nano-Fabrication and Micro-Engineering, Institute of Optics and Electronics, Chinese Academy of Sciences, Chengdu 610209, China
[2]Research Center for Applied Sciences, Academia Sinica, Taipei, Taiwan
[3]Department of Physics, National Taiwan University, Taipei, Taiwan
[4]Artificial-Intelligence Nanophotonics Laboratory, School of Science, RMIT University, Melbourne, VIC 3001, Australia
[5]Department of Electrical & Computer Engineering, National University of Singapore, Engineer Drive 3, Singapore 117576, Singapore
[6]e-mail: lxg@ioe.ac.cn
[7]e-mail: dptasi@sinica.edu.tw
[8]e-mail: min.gu@rmit.edu.au
[9]e-mail: elehmh@nus.edu.sg

Received June 22, 2018; revised September 5, 2018; accepted September 24, 2018; published November 13, 2018 (Doc. ID 335704)

This paper presents a review of the subwavelength interference effects of light in structured surfaces. Starting from the anomalous interference in simple structures such as double nanoslits, thin films, and catenary apertures, the theories and applications of light–matter interaction in layered, periodic, and aperiodic subwavelength structures are discussed. Two basic platforms, i.e., Young's double slits and the Fabry–Perot cavity, are used as prototypes for the investigation of the complex interference of surface waves. It is shown that these novel phenomena could dramatically reduce the characteristic lengths of functional devices and increase the resolution of optical imaging. By engineering the dispersion of surface waves, broadband responses beyond traditional limits in both temporal and spatial regimes have been demonstrated. As a final remark, the current challenges and future trends of subwavelength interference engineering are addressed. © 2018 Optical Society of America

https://doi.org/10.1364/AOP.10.000757

Subwavelength interference of light on structured surfaces

XIANGANG LUO, DINPING TSAI, MIN GU, AND MINGHUI HONG

1. INTRODUCTION

As one of the most essential characteristics of all kinds of waves, including light, sound, matter waves, and gravitational waves, the interference effects have always been the hotspot of research activities in scientific history. However, some wavelength-dependent properties such as the diffraction limit and delay-bandwidth limitation [1–3] hinder their applications in high-precision measuring, manufacturing, and functional optical devices. Over the last three decades, the emergence of subwavelength physics, including research into photonic crystals, plasmonics, and metamaterials, has led to renewed interest and a wealth of breakthroughs in the fields of optics, photonics, and even acoustics [4–14]. The main aim of this paper is to review recent progress of research on the anomalous light–matter interaction in subwavelength structures. Among various intriguing effects, subwavelength interference is the core of the subject, which in general refers to the constructive or destructive interference on a scale much smaller than the wavelength, accompanied by greatly enhanced evanescent fields. On such a scale, classical limitations regarding imaging resolution, device size, and operating bandwidth could be relaxed.

Perhaps the most famous subwavelength interference effect is related to the collective excitation of electrons and photons on a thin film made of noble metal, i.e., surface plasmon polaritons (SPPs) [5,15]. In an interference experiment with a silver mask perforated with nanoslits, it was shown that the period of the interference fringes on a thin metallic film was reduced to a feature smaller than one quarter of the vacuum wavelength, which is half the value predicted by classical interference theory [16,17]. In order to clarify the underlying mechanism, Young's double slits interference was re-investigated with finite-difference time domain (FDTD) simulations. Surprisingly, it was found that the fringe period can be even pushed down to smaller than $\lambda/15$ [18]. In another experiment, Schouten *et al.* proved that the mutual coupling of the two slits via SPPs will lead to a periodic fluctuation in the overall transmittance when the wavelength or distance between the two slits is changed [19]. From the dispersion curve lying below the light line, it is seen that the effective wavelength of the SPP may be much smaller than the vacuum wavelength [16]; thus the diffraction effect is suppressed. This property is in accordance with the earlier discussion on the negative refraction perfect lens [20] and extraordinary optical transmission (EOT) of light in a subwavelength aperture array [21]. As Pendry proposed in 2000, a single layer of silver film with negative permittivity could amplify the evanescent wave and form sub-diffraction-limited images in the near field [20]. The EOT phenomenon, originally reported in 1998 by Ebbesen *et al.* [21], was also explained using the interference and coupling of SPPs [22,23]. Based on the great promise of nanoscale light manipulation with noble metals, the term plasmonics was adopted to name this new discipline [24]. Great efforts have been spent to study various plasmonic devices, with greatly expanded applications such as bio-chemical sensors, nanolithography, photovoltaic devices, and photonic integrated circuits [1,25–28].

Apart from overcoming the diffraction limit, subwavelength interference of SPPs also plays an important role in local phase modulation and wavefront manipulation. Based on the near-field coupling of SPPs on adjacent metal–dielectric interfaces [16],

light transmission through double nanoslits with variant width was theoretically investigated [29,30]. The Fabry–Perot (F-P) interference inside the slits is responsible for the high-efficiency transmission, while the phase shift can be constantly varied by changing the slit width. Notably, the evanescent coupling of SPPs in the metallic slits results in a catenary-shaped intensity distribution (hyperbolic cosine function), which not only explains the width-dependent propagation constant but also enables high-contrast nanolithography with plasmonic cavity [31–33]. By arranging nanoslits and nanoholes with gradient geometric parameters, a set of flat optical components such as planar lenses, deflectors, and vortex beam generators was designed and experimentally validated by various groups [34–37], which finally led to the formation of the generalized laws of reflection and refraction [38–40]. More recently, the subwavelength slits were extended to include the "catenary of equal strength" [41,42], which generates a linear phase distribution by transforming the spin state of circularly polarized incidence via space-variant nanoslits perforated in metallic films. Because the induced geometric phase shift is switchable with the polarization states, similar structures are useful in the design of multifunctional planar devices with polarization selectivity [43–47].

The subwavelength interference effect also exists in circumstances beyond the metal–dielectric interfaces mentioned above. Taking the F-P type interference in a three-layered optical system as an example, there are periodic transmission maxima when the thickness of the slab equals the integer times half the wavelength. Similarly, both Salisbury-type electromagnetic absorbers and anti-reflection coatings have a minimal thickness of one quarter wavelength. From the most fundamental interference condition, it is known that the key for either constructive or destructive interference is phase matching. In classical F-P resonators, the phase shift relies exclusively on the propagation delay along transmission; thus a rigid restriction on the thickness is derived. With the emergence of phase-shifting surface structures [48], additional degrees of freedom are introduced to meet the phase-matching requirement and construct subwavelength interference for various applications. For example, Sievenpiper *et al.* showed that a thin metal-backed structure (high-impedance surface) has a 180° phase change at the resonant condition [49], which was intensively studied to reduce the thickness of antennas and radar absorbers [50–52]. Using a configuration consisting of a lossy metasurface with tailored frequency dispersion [53], one can introduce frequency-dependent phase change, resulting in destructive interference and near-perfect absorption over a continuous and broad spectrum [54,55].

In addition to the above anomalous interference effects associated with subwavelength structures, it should be noted that there are similar phenomena in quantum and statistical optics [56,57]. In coincidence measurement, high-order interference patterns with reduced interference periods have been observed. By using N entangled photons, the interference pitch may be shrunk to be $\lambda/2N$ [58]. Unfortunately, this quantum or coincidence interference is still very weak and relies on specific measurement conditions [59]; thus much work is still needed to meet the requirements of engineering applications.

As a result of the explosion of scientific discoveries and theoretical and experimental advancements in areas related to subwavelength structures, it is hard to give a comprehensive survey of all the results. Although several nice reviews on similar topics have already been presented [1,7,9,10,26,28,60–63], little attention was paid to the subwavelength interference effects. In this paper, we would like to provide a concise discussion of the phenomena and principles of subwavelength interference as well as their engineering applications. The structure of the paper is as follows. In the introduction, we present a brief description of the research history and classification of

subwavelength interference. In Section 2, anomalous interference phenomena in subwavelength structures are reviewed. In Section 3, basic theories of diffraction, refraction, and reflection at the subwavelength scale are provided based on the interference principle. In Section 4, the subwavelength interference in layered structures is reviewed. In Sections 5 and 6, periodic and aperiodic subwavelength structures with embedded subwavelength interference are discussed in detail. In Section 7, the challenges of current technologies and future developing trends are outlined.

2. ANOMALOUS INTERFERENCE IN SUBWAVELENGTH STRUCTURES

The formation of new theories in sciences generally starts with the observation of abnormal effects or phenomena that could not be explained by conventional theories. Among various theories about the generation, propagation, and absorption of light, the interference of light plays an extremely significant role. In this section, we show that both Young's double slits and the F-P cavity can find their counterparts in the subwavelength scale, featuring novel physical properties different from classical cases. Of course, it should be remembered that in many complex structures, the interference phenomena are rather intricate and cannot be simply described using these elementary concepts.

2.1. Extraordinary Young's Interference

As the heart of wave physics, Young's double slits experiment was thought of as one of the most beautiful physical experiments in history [64]. It has been used to validate the wave physics of both photons and electrons. To date, there has still been much research on the quantum physics of the multiple photon interference experiment with such a simple configuration [65,66]. In this review, we would like to constrain ourselves in classical optics and not be involved in quantum entanglement and related phenomena. Even in this condition, we will show that there are still many new physics when the scale of light–matter interaction is scaled down to smaller than the wavelength. At the beginning of the discussion, we note that the classical Young's double slits experiment has made some assumptions. First of all, the material of the screen is often assumed to be a perfect absorber or perfect electric conductor (PEC); second, the mutual coupling of the slits is ignored; third, the influence of the slit width and the polarization of incident light on the interference fringes is often ignored. These conditions are keys to understand the following anomalies, which are referred to as extraordinary Young's interference (EYI) for simplicity.

For a typical standing wave created by two counter-propagating waves, the period of the intensity peaks is generally known to be half of the wavelength. As a consequence, one can assume that there will be no observable interference patterns when two slits are placed with a distance smaller than half a wavelength, and this condition is also required for effective medium theory to be applicable [67,68]. When the period of the metamaterial becomes larger than $\lambda/2$ but smaller than λ, higher-order diffraction may occur for off-axis illumination. When the period is larger than λ, these structures must be considered as diffraction gratings.

To investigate the Young's interference on the deep-subwavelength scale, i.e., when the geometric parameters are much smaller than the wavelength, the light field distribution for a pair of double slits separated by 100 nm and perforated in a 20-nm-thick silver film is shown in Fig. 1 [18]. A very interesting phenomenon can be seen: at a wavelength of 365 nm, the peak-to-peak distance is close to 100 nm, and no interference pattern is observed; at a wavelength of 385 nm, the peak-to-peak distance is decreased to about 25 nm, which is almost $\lambda/15$. The electric field distribution implies that surface plasmon resonance has been excited. If the localized fields in the bottom

left figure are taken as an interference pattern, a more counterintuitive conclusion may be drawn: the increase of wavelength has led to a much smaller interference pattern. This EYI effect means that one need not reduce the wavelength to achieve higher resolution; thus the classical diffraction limit could be overcome. Note that the above phenomena can only be observed for transverse magnetic (TM) but not transverse electric (TE) polarization, which is also distinct from the macroscopic experiment.

In practice, subwavelength interference is difficult to record with traditional instruments such as charge coupled devices (CCD) and complementary metal oxide semiconductor (CMOS) detectors. By placing a photoresist (PR) layer below the perforated silver film, a simple method was proposed to record the subwavelength interference fringes. This configuration also functions as a novel scheme for sub-diffraction-limited nanofabrication. As illustrated in Fig. 2, with a light source operating at 436 nm, the width of the one-dimensional (1D) interference fringe was reduced to smaller than 50 nm [17], which is almost only 1/9 of the vacuum wavelength. According to numerical simulations and dispersion diagram of the SPP, this

Figure 1

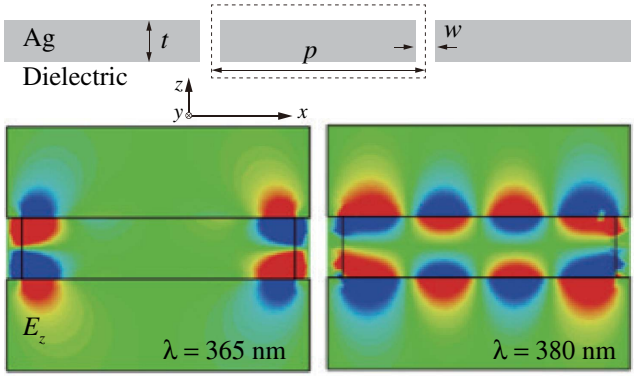

EYI on a thin silver film. The top panel displays the geometric configuration. The values of p, w, and t are set as 100, 10, and 20 nm. The dielectric constant is supposed to be 2.89. The bottom panel displays the z component of the electric fields with the same magnitude scale. Adapted with permission from Pu *et al.*, ACS Photon. **5**, 3198–3204 (2018) [18]. Copyright 2018 American Chemical Society.

Figure 2

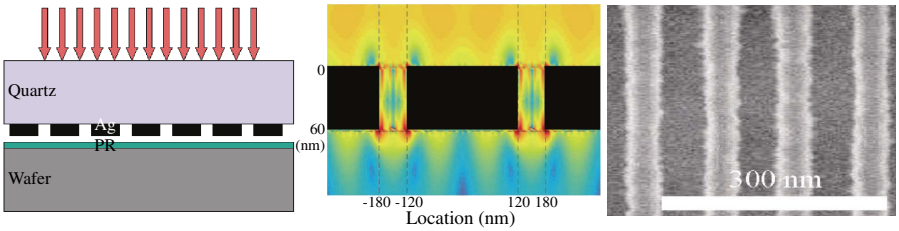

Plasmonic interference with 1D grating on a metallic mask. From left to right: the experimental configuration, simulated intensity distribution, and scanning electron microscope (SEM) image of the photoresist pattern. Adapted with permission from Luo and Ishihara, Appl. Phys. Lett. **84**, 4780–4782 (2004) [17]. Copyright 2004 AIP Publishing LLC.

approach may provide a promising alternative to traditional bulky and costly photolithographic systems [26,69].

The excitation and interference process in the above experiment can be separated to realize more flexible modulation of the interference patterns. Figure 3 shows a method to realize two-dimensional (2D) interference [70]. By using a 266 nm exposing light and four mutually perpendicular 1D aluminum (Al) gratings with a 130 nm periodicity, a square lattice of 2D dot array with a 90 nm periodicity and a 40 nm feature size was realized. By arranging many different gratings and employing the holography principle, more complex 2D interference patterns were subsequently demonstrated [71,72].

To render the subwavelength interference effect into practical imaging or lithographic devices, the energy efficiency must be optimized. In general, the separation distance and width of the slits, together with the film thickness, will influence the efficiency at a given wavelength. As a result, these geometric parameters have been optimized in previous simulations and experiments [16,17]. In a follow-up work, the Young's interference at the metal surface was revisited with a detailed discussion of the influence of the incident wavelength [19]. It was found that the total intensity of the far-field diffraction pattern is reduced or enhanced as a function of the wavelength of the incident light beam, as shown in Fig. 4. Such a phenomenon is attributed to the constructive and destructive interference of SPPs propagating along the surfaces. When the incident field is TE-polarized, the transmission of the double slits is small and weakly modulated as a function of wavelength. This experiment is also an additional physical explanation of the famous EOT effect [21]. From the perspective of electromagnetics, this unusual interference effect is related to the mutual coupling of antennas [73], which has been widely known in antenna theory. As a result, surface waves in microwave frequency could also result in similar fluctuation [74].

Using the dispersion relations of waveguide modes derived from boundary conditions, it is straightforward to show that the effective wavelength of the SPP, defined by the vacuum wavelength divided by the mode index, is dependent on the film thickness [16] or the gap width for the nanoslits [29]. As shown in Fig. 5, when light passes through two slits with the same thickness and different widths (w_1 and w_2), light in two channels may acquire a phase shift of π; thus the intensity at the center of the two slits becomes zero. This is in contrast to the bright line formed in the traditional interference experiment, where the slit width only influences the transmitted intensity

Figure 3

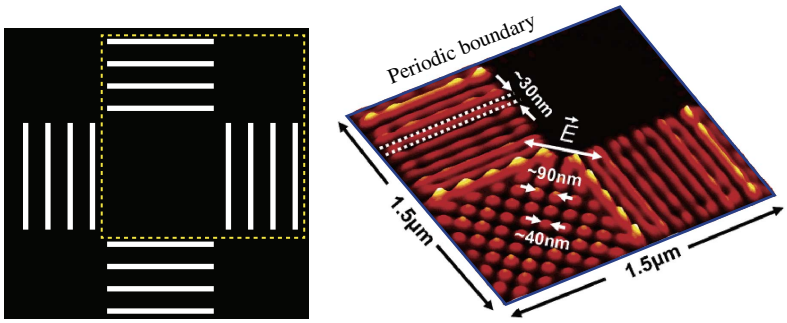

2D interference patterns generated by four mutually perpendicular gratings. Periodic boundary conditions are used in the simulation (depicted by the dashed lines shown in the left panel). The incident light polarization is aligned along the diagonal. Adapted with permission from Liu *et al.*, Nano Lett. **5**, 957–961 (2005) [70]. Copyright 2005 American Chemical Society.

but not the phase shift. Furthermore, by properly tuning the geometric parameters of these nanoslits, constructive and destructive interference was used to direct the energy flow to one particular direction [30]. Meanwhile, more slits or wider slits filled with dielectrics have been adopted to increase the exciting efficiency [75].

In another regime, anisotropic apertures were used to excite SPPs and the interference is dependent on the incident light polarization. Based on the complex photonic spin-orbit interaction, polarization-controlled unidirectional excitation of SPPs and holographic pattern generation are demonstrated [76,77]. Figure 6 shows a simple configuration for switchable directional excitation. Two arrays of rectangular nanoslits with a relative rotation of $\theta = \theta_2 - \theta_1$ are placed adjacent to each other with a horizontal distance of $\lambda_{spp}/4$. Under circularly polarized illumination, the phase difference between the two scattering channels is shown to be $\pi/2 \pm \theta$. If θ is set to $\pi/2$, the interference may be switched from constructive to destructive when the incident light

Figure 4

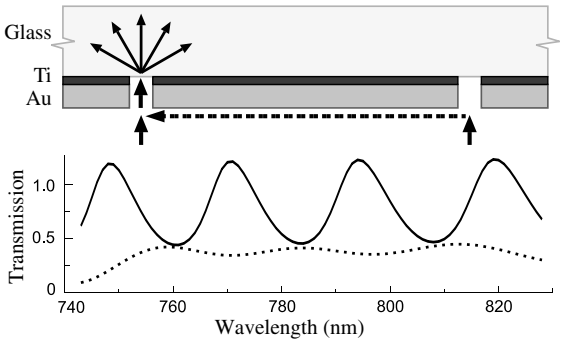

Mutual coupling in Young's double slits experiments. The normalized transmission oscillates as the change of wavelength. The solid and dashed lines indicate the transmission for TM and TE polarization, respectively. Figures 2 and 3 adapted with permission from Schouten *et al.*, Phys. Rev. Lett. **94**, 053901 (2005) [19]. Copyright 2005 American Physical Society.

Figure 5

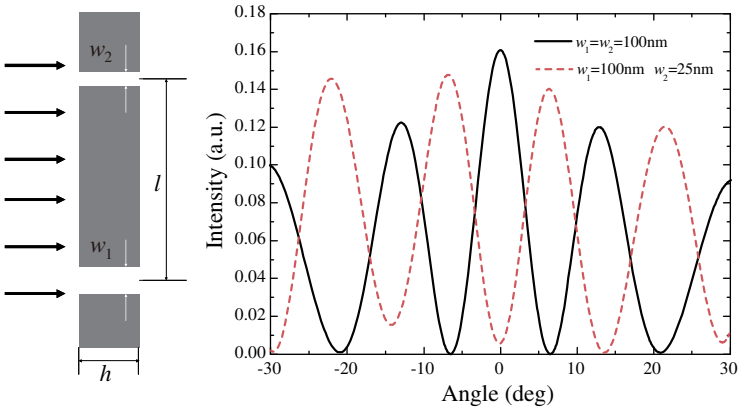

EYI experiment with non-equal widths. The angular shift of far-field energy distribution leads to a dark fringe at the normal direction ($\theta = 0°$). Adapted with permission from [29]. Copyright 2007 Optical Society of America.

is changed from left-handed circular polarization (LCP) to right-handed circular polarization (RCP), or vice versa.

Another interesting interference effect occurs in continuously deformed slits [41,78]. As shown in Fig. 7, circularly polarized light illuminated on this aperture is turned into its cross-polarization, and then deflected into one side determined by the handedness of the incident light. Owing to the constant phase gradient along the x direction, the corresponding curve is also denoted as "catenary of equal phase gradient": $y = \Lambda/\pi \cdot \ln(|\sec(\pi x/\Lambda)|)$, where Λ is the horizontal size. Notably, this interference effect is rather different from both the above double slits experiment and the beaming effect [79]. Owing to the continuous and linear gradient phase in the aperture, only light along one particular direction is coherently enhanced. By shape deformation and

Figure 6

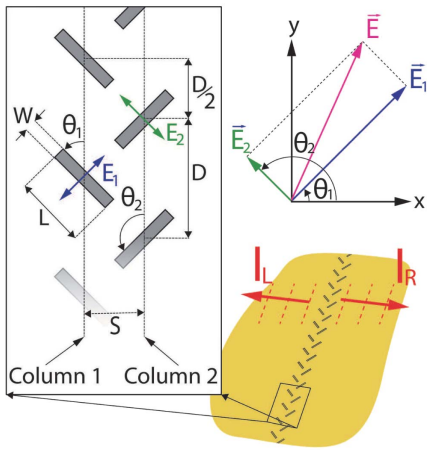

Switchable excitation of SPP by two columns of apertures with a rotation angle of 90° under circular polarized illumination. The apertures of the first and second columns are oriented at angles θ_1 and θ_2 with respect to the y axis. The combined SPP waves propagating away from the column pair (red arrows) have intensities I_R and I_L. From Lin *et al.*, Science **340**, 331–334 (2013) [76]. Adapted with permission from AAAS.

Figure 7

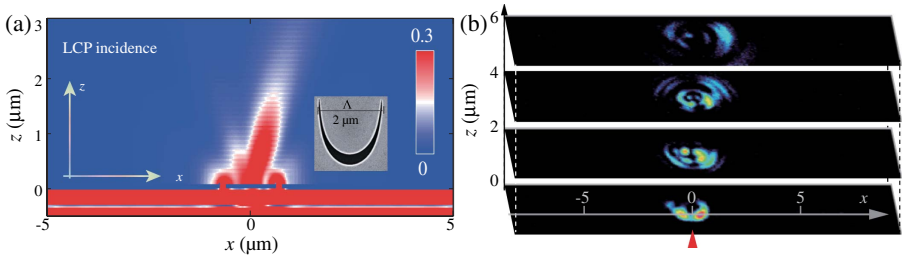

Spin Hall effect of light induced by a single catenary-shaped aperture. (a) Cross-polarized electric intensity in the xz plane ($y = 1$ μm). (b) Measured cross-polarized intensity patterns in the xy planes for $z = 0$, 2, 4, and 6 μm under LCP illumination ($\lambda = 632.8$ nm). Reproduced from [78] under the terms of the Creative Commons Attribution NonCommercial-NoDerivs 4.0 License.

arranging single elements into an array, miniaturized Bessel-like beam generators and flat lenses have also been designed and experimentally characterized [78]. Since the performance does not depend on the excitation of SPPs, it is straightforward to scale the device to other frequency bands by taking advantage of the scalability of Maxwell's equations.

The discovery of the EYI effect has led to a new concept termed "meta-surface-wave (M-wave)," which is defined as a special surface wave confined at the surface of structured materials [38,80]. In general, there are three typical properties that distinguish M-waves from other kinds of waves. First, the effective wavelength of the M-wave could be much smaller than the vacuum wavelength, which is beneficial for imaging and lithography beyond the diffraction limit; second, the propagation constant is tunable via changing the geometric parameters such as the slit width and film thickness, leading to a local controllable phase shift; third, for typical structures such as metallic thin films and slits, the field distribution tends to follow hyperbolic cosine (catenary) and sine functions, as a result of the evanescent coupling effect [18]. This forms one basis of the so-called catenary optics.

2.2. Subwavelength F-P Interferometer

In Young's double slits experiment, subwavelength interference takes place in the plane perpendicular to the original propagation direction of incident light. In contrary, F-P interferometers are characterized by interference along the propagation direction. By adding subwavelength surface structures on the two sides of the classical F-P cavity (a single dielectric slab), the interference phenomena would change dramatically. Figure 8(a) shows a simple configuration based on metallic slits separated by a dielectric slab of $\varepsilon = 2.25$. Without these subwavelength slits, a 10-mm-thick dielectric slab would have a transmission peak at $f = 10$ GHz ($\lambda = 20$ mm). However, the introduction of subwavelength slits makes the peak shift to 5.13 GHz owing to the additional phase shift induced by the localized fields, as shown in Fig. 8(b) [80]. Since the thickness is only about one sixth of the wavelength, this subwavelength interference provides an efficient approach to reduce the thickness of similar devices.

Figure 8

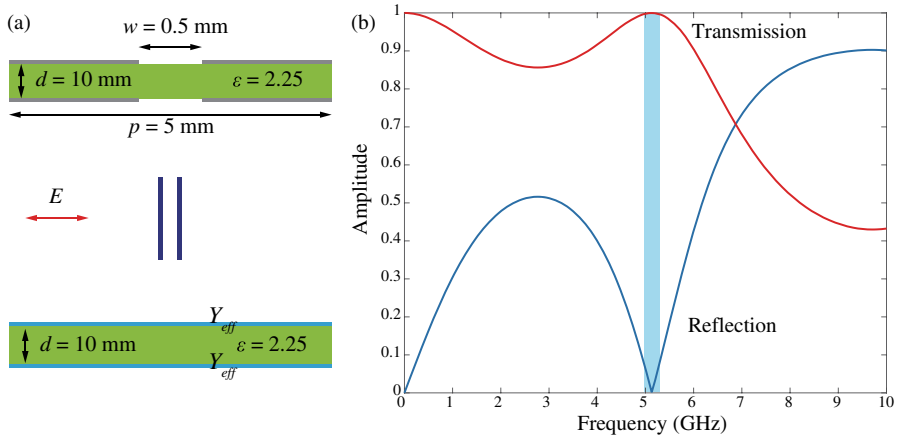

Subwavelength F-P interference. (a) Definition of the geometric parameters. The bottom shows an effective medium model based on effective admittance. Adapted with permission from [80]. Copyright 2018 Optical Society of America. (b) Calculated transmission and reflection coefficients for TM polarization. The transmission peak locates at $f = 5.13$ GHz.

As a reflective F-P cavity with a reflective layer on one side, the Gires–Tournois interferometer (GTI) could also be significantly modified by subwavelength structures. Figure 9(a) shows the simplest configuration that replaces the reflective layer by a metallic groove array known as a metamirror. As depicted in Fig. 9(b), it transforms the reflective phase from π to 0 when the depth of the groove equals one quarter of the wavelength. By defining the ratio of the tangential electric field to the tangential magnetic field at the surface, the surface impedance is transformed from 0 to infinity (high impedance) at the resonant frequency. Since the electric field reaches a peak at the top surface, such structures are useful in the design of thin antennas and solar cell absorbers [81]. Figures 9(c) and 9(d) show the measured absorption and simulated electric field distribution when a silver mirror is substituted by a metallic grating, demonstrating a clear enhancement of the photon absorption fraction in almost the entire visible range. Note that besides the simple groove array, many other types of structures, including mushrooms and patches arrays on the ground plane [49,53], can be used to realize high impedance with much smaller thickness than these grooves.

The high-impedance surfaces or the so-called artificial magnetic conductors (AMCs) typically operate in a narrow band. Using the small antenna theory [82], it is easy to prove that the relative bandwidth for a non-magnetic structure is expressed as $B \ll 2\pi d/\lambda$, where d is the overall thickness [51]. To increase the operational bandwidth, other degrees of freedom such as the top surface (metasurface) of the GTI may be utilized. Using the transfer matrix theory, it is seen that if the dispersion of the metasurface follows a specific rule, broadband response may be achieved for various kinds of devices such as absorbers, polarization converters, and wavefront

Figure 9

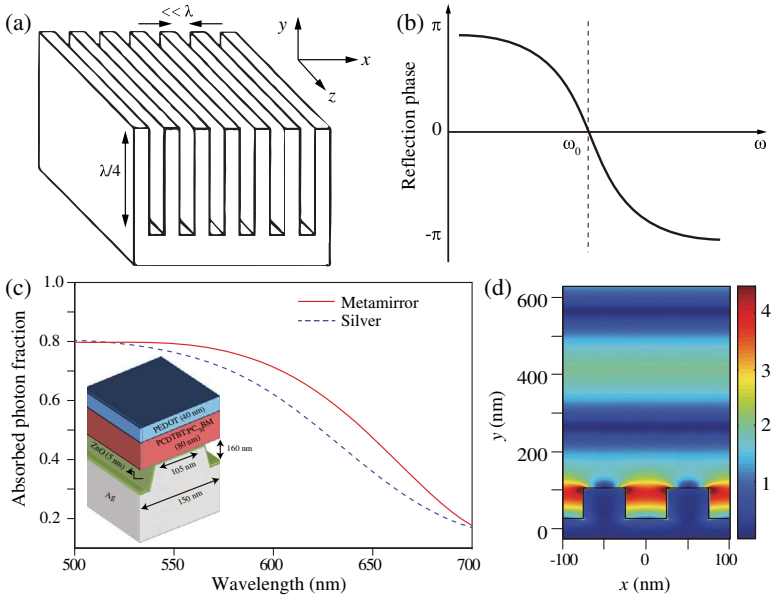

(a) Corrugated quarter-wavelength-deep metal slab with high surface impedance. (b) Reflection phase of a resonant textured surface. © 1999 IEEE. Adapted, with permission, from Sievenpiper *et al.*, IEEE Trans. Microwave Theory Tech. **47**, 2059–2074 (1999) [49]. (c) Absorption enhancement of solar cell by metamirror composed of metallic grating. (d) Simulated electric field distribution at a wavelength of 600 nm. Adapted with permission from Macmillan Publishers Ltd.: Esfandyarpour *et al.*, Nat. Nanotechnol. **9**, 542–547 (2014) [81]. Copyright 2014.

shapers [55,83–88]. As shown in Fig. 10, both the resistance (R) and reactance (X) of a perfectly impedance matched metasurface are dependent on the operating wavelength (or frequency) [53], which can be approached using a Lorentz-type resonance induced by a metallic patches array [55]. With this dispersion-engineered metasurface, the absorption bandwidth has been doubled without increasing the thickness.

Another interesting effect of the GTI is related to the evanescent waves. As shown in Fig. 11(a), when evanescent waves are excited at the front layer and reflected back by the ground plane, the intensity profile inside the dielectric spacer could be expressed as $A\ \exp(-2\alpha z) + B\ \exp(2\alpha z)$, where α is the attenuation constant, z is the propagation direction, and A and B are coefficients [18]. Clearly, the intensity profile resembles an ideal catenary shape, which could double the depth of field and lead to better pattern transfer characteristics for nanolithography [89,90]. As will be discussed in more detail in Subsection 4.1, a large number of current plasmonic lithographic designs are based on this simple configuration [32,33,91,92].

When both the reflecting surfaces of the GTI are not penetrable, the structure transforms into a metal–insulator–metal (MIM) waveguide [Fig. 11(b)]. In this case, catenary optical fields are just the eigenmodes of this waveguide. The change of width between the metal has a critical influence on the optical fields and the propagation constant [39]. Such an effect was extensively exploited to realize local phase

Figure 10

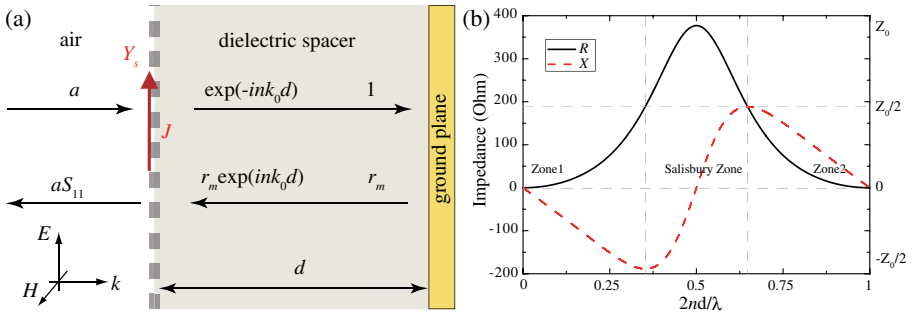

(a) Schematic of layered absorber based on a modified GTI composed of a metasurface, dielectric spacer, and metallic ground plane. (b) Ideal impedances for perfect absorption versus the effective thickness of the dielectric layer. Adapted with permission from [53]. Copyright 2011 Optical Society of America.

Figure 11

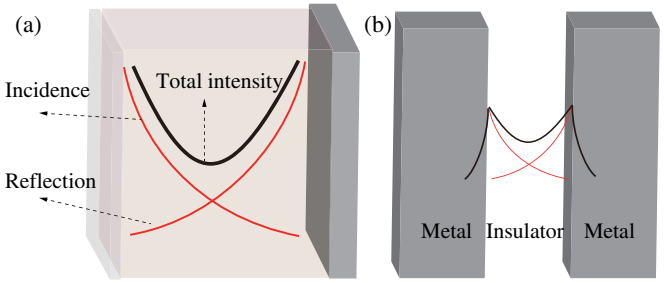

Coupled evanescent waves in (a) a GTI interferometer and (b) a MIM waveguide.

modulation for applications ranging from beam steering and flat lensing to orbital angular momentum (OAM) generation [34,35,37,39,93].

2.3. Inter-Mode Interference in Resonators Array

In 1935, Fano gave a hypothetical explanation of the asymmetric line shape of Rydberg spectral atomic lines and suggested a formula that predicts the shape of spectral lines based on quantum interference [61]. This effect was later widely exploited in many physical systems, and presented a powerful tool for analyzing mode interference. In some circumstances, the mode interference can be interpreted using Young's double slits interference. For instance, Young's interference has been observed in plasmonic structures when two or more nanoparticles with separation on the order of the wavelength are illuminated simultaneously by a plane wave [94,95]. The scattering fields in the intermediate region would interfere and lead to enhanced field intensity, absorption, and scattering. The localized intensity in a plasmonic dimer may be much larger than that in a single metallic nanoparticle [95,96], and the intensity enhancement factor is dependent on the geometry of each nanoparticle [97]. As illustrated in Fig. 12, in dimer plus monomer systems with separations less than 300 nm [94], two distinct resonances are attributed to the contributions of the dimer (around 790 nm) and monomer (around 660 nm), which is consistent with the scenario of plasmon hybridization between the dimer and the monomer. However, when the dimer–monomer separation is in the range of 400–700 nm, a new behavior emerges as indicated by the shallow pink region.

The mode interference is usually associated with the symmetry of the structures. By utilizing asymmetric structures such as asymmetrical split rings and bars [98,99], sharp trapped (or dark) modes may be excited and interfere with the bright mode; thus asymmetric spectral lines appear. Fano resonance can also be induced by breaking the translational symmetry, i.e., the periodicity of periodic structures. To illustrate this, three magnetic resonators composed of wire pairs are designed with slightly different resonant frequencies [100]; thus high-quality-factor trapped modes are introduced. In the ideal case, the dark mode cannot be accessed by far-field excitation,

Figure 12

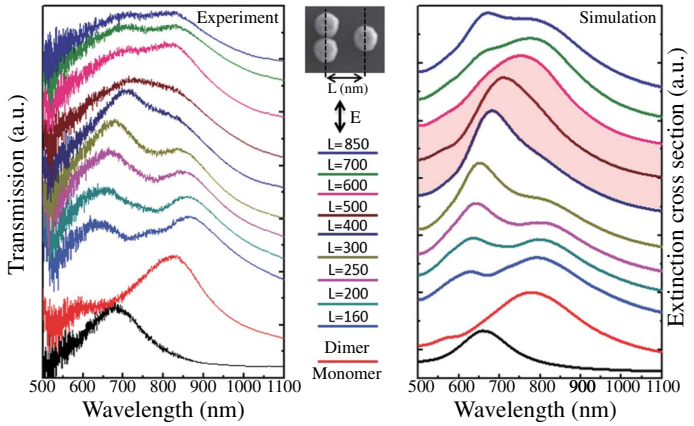

Experimentally measured transmission spectra (left) and simulated extinction cross sections (right) at several different separation distances L (corresponding to the SEM images in the middle panel) for the polarization direction perpendicular to the separation axis. The shadowed area in the right panel indicates the separation range where Young's resonance appears. Adapted with permission from Rahmani *et al.*, Small **10**, 576–583 (2014) [94]. Copyright 2013 Wiley-VCH Verlag.

as a result of destructive interference. However, the introduction of tiny asymmetry makes destructive interference not perfect; thus an asymmetric light spectrum is formed with huge local field enhancement, which may have far-reaching applications in bio-chemical sensors, nanolasers, and filters, among other electro-optical devices [61,101].

Note that the loss of material has a significant influence on the resonant spectrum, and the loss mechanism in the asymmetric structure can be utilized to realize a wideband and wide-angle absorber, as intensively studied in recent years [100,102] (see more details in Subsection 5.2). To reduce the optical loss, all-dielectric dimers have also been investigated [103,104]. Regardless of the fact that dielectric resonators often have larger sizes and a smaller field enhancement factor, the negligible absorption is helpful to avoid the heating problem in metallic structures [103].

3. GENERALIZED THEORIES

In this section, an overview of the general theories for the diffraction, refraction, and reflection behaviors of light is given based on the interference principle. Most contents in the following subsections can be described with the theories given here.

3.1. Interference Theories for Sub-Diffraction Imaging

Traditional optical imaging theory proposed by Abbe in 1873 is based on the interference of the spatial spectrum of the diffracted light [105]. The diffraction limit is a natural consequence of the loss of high-spatial-frequency components, such as the large off-axis components not collected by the imaging lens and the evanescent waves that decay exponentially away from the object [106,107]. Recent results show that the high-spatial-frequency components may be recovered via various near-field or far-field techniques; thus the barrier of the diffraction limit may be overcome [17,20,25].

In general, the physical model of Abbe imaging is outlined in Fig. 13. The light fields scattered or radiated by the objects are collected by the lenses or mirrors, while the

Figure 13

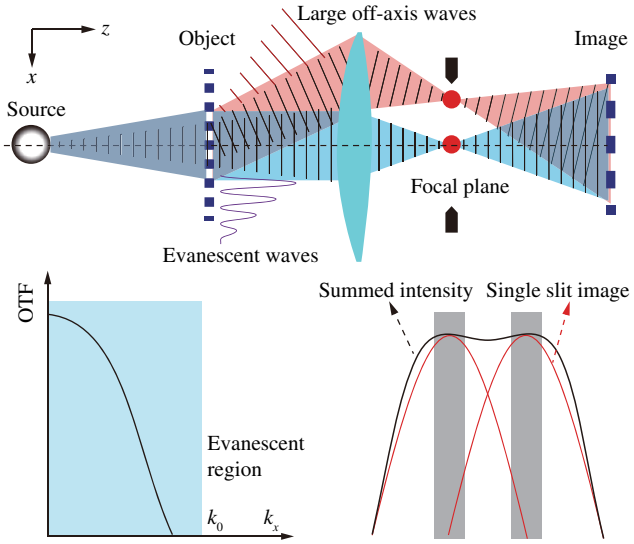

Interference theory of the image formation. The top panel shows the Abbe's imaging process, where larger off-axis components cannot be collected by the lens. The red dots represent the spatial-frequency spectrum. The bottom panel shows the OTF function and images for two slits placed at a distance equal to the diffraction limit.

CCD, CMOS, or other photosensitive materials are utilized to record the interference patterns [105]. Since high-order diffraction and evanescent waves are absent in the interference process, as shown in the optical transfer function (OTF), such lens systems are diffraction limited; i.e., the resolution is limited by $0.5\lambda/\mathrm{NA}$, where NA is the abbreviation for numerical aperture.

In Abbe's theory, the field distribution in the image plane is expressed using the Fourier transform of the vectorial spatial spectra:

$$\begin{bmatrix} E_x(x,y,z) \\ E_y(x,y,z) \\ E_z(x,y,z) \end{bmatrix} = \int_{-\infty}^{\infty}\int_{-\infty}^{\infty} \begin{bmatrix} A_x(k_x,k_y) \\ A_y(k_x,k_y) \\ -(k_xA_x + k_yA_y)/k_z \end{bmatrix} \times \exp(ik_xx + ik_yy)\mathrm{d}k_x\mathrm{d}k_y, \quad \textbf{(1)}$$

where

$$\begin{bmatrix} A_x(k_x,k_y) \\ A_y(k_x,k_y) \end{bmatrix} = \int_{-\infty}^{\infty}\int_{-\infty}^{\infty} \begin{bmatrix} O_x(x,y)T_x(k_x,k_y) \\ O_y(x,y)T_y(k_x,k_y) \end{bmatrix} \times \exp(-ik_xx - ik_yy)\mathrm{d}x\mathrm{d}y. \quad \textbf{(2)}$$

Here $O(x,y)$ represents the optical fields produced by the objects, $T(k_x,k_y)$ is the OTF of the optical system, and A_x and A_y are the spatial spectra for the x and y polarizations in the image plane.

One straightforward approach to surpass the classical diffraction limit is to utilize high-spatial-frequency components in the OTF. In microscopy imaging and nanolithography applications, metal–dielectric multilayers are promising candidates for such applications as a result of the strong plasmonic coupling effects, which lead to the amplification of evanescent waves. As early as 2000, Pendry proved that a single silver layer could work as a perfect lens [20]. For multilayers, it was shown that complex mode coupling could enable a broader transmission bandwidth in the evanescent region [108], as shown in Fig. 14(a). Interestingly, when one reduces the thickness of the layers, the transmission at higher spatial frequency will be significantly increased. In the deep-subwavelength limit, such multilayers can be considered as an effective medium.

Using effective medium theory, the equivalent anisotropic permittivities of the deep-subwavelength multilayers are written as

$$\varepsilon_z = \frac{\varepsilon_m t_m + \varepsilon_d t_d}{t_m + t_d}, \qquad \frac{1}{\varepsilon_x} = \frac{1}{\varepsilon_y} = \frac{t_m/\varepsilon_m + t_d/\varepsilon_d}{t_m + t_d}, \quad \textbf{(3)}$$

where ε_m and ε_d are the permittivities of metal and dielectric, and t_m and t_d are the thicknesses. According to the wave equation, the dispersion relation of the propagating wave becomes

$$\frac{k_x^2 + k_y^2}{\varepsilon_z} + \frac{k_z^2}{\varepsilon_x} = \left(\frac{\omega}{c}\right)^2. \quad \textbf{(4)}$$

Clearly, this dispersion curve is hyperbolic if $\varepsilon_z\varepsilon_x < 0$. Depending on the value of ε_z, there are two hyperbolic materials that exhibit all-pass ($\varepsilon_{xy} > 0, \varepsilon_z < 0$) and high-pass ($\varepsilon_{xy} < 0, \varepsilon_z > 0$) filtering property, respectively. On the one hand, the all-pass filter is suitable for super-resolution imaging, because both high and low spectral components can be used to reconstruct the images. On the other hand, the high-pass filters are often used to filter out undesired low spatial components, as shown in Fig. 14(b). On the condition of $\varepsilon_z \approx 0$, all spatial frequencies are forced to propagate along the z direction, which has been widely used in magnifying and demagnifying imaging systems

(see Subsection 4.2 for details) [109–113]. Note that here we are merely interested in the super-resolution imaging based on hyperbolic materials; readers can refer to other references for applications in the enhancement of spontaneous emissions [114–116].

Figure 14(c) illustrates a typical configuration for super-resolution lithography based on the combination of superlens/hyperlens, photoresist, and a reflective layer. As shown in the OTF curves [Fig. 14(d)], the superlens has a transmission peak located at the evanescent region accompanied with relatively high transmission in the propagating region, which helps to increase the resolution of imaging lithography. For the high-pass hyperlens, pure evanescent waves with large horizontal wavenumber are filtered; thus higher resolution is feasible especially for interference lithography [117].

The above OTF curves indicate that the use of plasmonic effects could amplify the evanescent waves that are otherwise lost, thus providing a route to break both the far-field and near-field diffraction limits. Similar to Abbe's definition, the near-field diffraction limit means that the resolution is limited by both the wavelength and the working distance, which is defined according to the working distance at which the highest evanescent component decays to its $1/e$ in vacuum [38]:

$$\delta \geq \frac{\lambda}{2} \frac{1}{\sqrt{1 + \left(\frac{\lambda}{2\pi d}\right)^2}}, \tag{5}$$

where δ is the resolution at a given working distance d between the image and lens. Obviously, this equation could be combined with the far-field diffraction limit to give a universal definition:

Figure 14

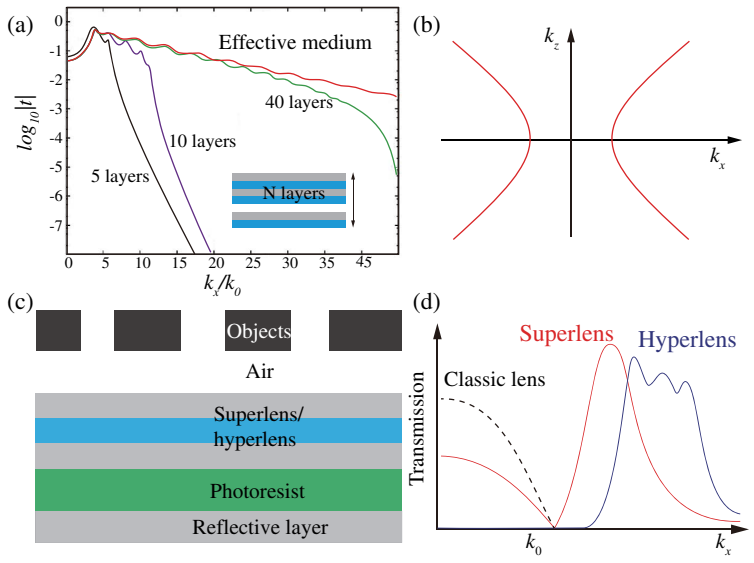

Optical properties of metal–dielectric multilayers. (a) OTF for a slab divided into 5, 10, and 40 layers. When the thickness of each layer becomes much smaller than the wavelength, it approaches the effective medium theory. Adapted with permission from Wood *et al.*, Phys. Rev. B **74**, 115116 (2006) [108]. Copyright 2006 American Physical Society. (b) Dispersion relation of the hyperbolic lens with $\varepsilon_z > 0$. (c) Schematic of the sub-diffraction imaging lithography based on plasmonic lens. (d) Optical transmission for typical superlens (red), hyperlens (blue), and traditional lens (dashed line).

$$\delta \geq \frac{\lambda}{2}\frac{\sqrt{D^2+4d^2}}{D\sqrt{1+\left(\frac{\lambda}{2\pi d}\right)^2}} = \frac{\lambda}{2\mathrm{NA}}\frac{1}{\sqrt{1+\left(\frac{\lambda}{2\pi d}\right)^2}}, \tag{6}$$

where D is the aperture diameter of the lens. When the working distance d is much larger than the wavelength, Eq. (6) is reduced to $\delta \geq 0.5\lambda/\mathrm{NA}$, i.e., the classical diffraction limit proposed by Abbe. To compare the resolution of plasmonic lenses with the near-field diffraction limit, a plasmonic cavity lens composed of Ag–photoresist–Ag incorporating high-spatial-frequency spectrum off-axis illumination was proposed [118]. This approach remarkably enhances the object's subwavelength information and damps negative imaging contributions from the longitudinal electric field component in the imaging region. Experimental images of well-resolved 60 nm half-pitch patterns under 365 nm ultraviolet light were demonstrated at an air distance of 80 nm between the mask patterns and the plasmonic cavity lens, approximately four-fold longer than that of the superlens scheme.

Although plasmonic effects are able to amplify evanescent fields by the excitation of highly localized modes, it is generally not suitable for telescopy applications since both the object and image are located in the far field of the lens system. In fact, the traditional roadmap for a higher resolution telescope is still based on the continuous increase of the lens aperture [8]. Fortunately, recent studies demonstrated that proper manipulation of the wavefront could lead to an exotic interference effect known as superoscillation, where the light intensity function could oscillate much quicker than its highest Fourier component [119]. Seemingly counterintuitive, this anomalous effect may be understood by investigating the difference between the complex amplitude and intensity. As depicted in Fig. 15, if one constructs an intensity function as $|\sin(2\pi x) + 0.99|^2$, a small peak can be obtained with very small width. Though this example is very simple, it reveals some important aspects of superoscillation interference. First, although the local intensity may oscillate more rapidly than the highest Fourier components, the complex amplitude often does not have this property. Notably, if one could record and reconstruct complex optical fields, the time-reversal process could be used to realize super-resolution focusing and imaging [120]. Second, the superoscillation is weak and accompanied by strong side lobes. In general, the narrower the superoscillatory lobe, the higher the side lobe will be, which poses a serious challenge for the practical applications [121].

In superoscillatory focusing and imaging with a flat metasurface, it is easy to control the interference effect by tuning the phase and amplitude of transmission or reflection coefficients by locally tuning the subwavelength structures. The physical process of far-field interference may be fully understood using the vectorial diffraction theory [41,122]. Assuming that light is propagating along the $+z$ direction and the field

Figure 15

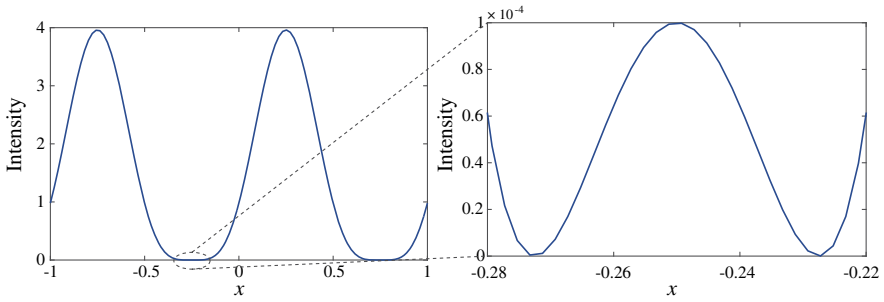

1D superoscillatory function (solid blue line) and its magnified view.

at $z = 0$ is known, the vectorial electric fields at any plane with $z > 0$ are calculated using Fourier transform of the spatial-frequency components. By optimizing the amplitude and phase function, superoscillatory focusing and imaging devices can be designed [121,123–125]. For instance, benefiting from the nearly dispersionless feature of phase modulations with metasurfaces, a superoscillatory metasurface filter was proposed for broadband super-resolution imaging. In demonstrative experiments, resolving ability of about 0.64 times of the Rayleigh criterion is obtained for visible light ranging from 400 to 700 nm [126]. This method is expected to potentially promote the development of super-resolving telescopes and microscopes.

3.2. Interference Theories for Reflection and Refraction

Formulated in 1621 and 1821, respectively, Snell's law and Fresnel's equations are two fundamental rules of the design of lenses and mirrors, and both of them are deduced from the electromagnetic boundary conditions. According to Snell's law of refraction, a refractive lens should be constructed using curved surfaces to bend light correctly. Consequently, the mass of the lens usually increases approximately by the cube of its diameter [8]. Although large reflective telescopes have much smaller weight than lenses at the same aperture, precise fabrication and measurement are still very challenging. Fortunately, it has been shown that the anomalous interference effects in subwavelength structures could dramatically change the optical responses at surfaces, based on which traditional equations governing the refraction and reflection must be cast into a new form. The so-called generalized Snell's law and generalized Fresnel's equations [38–40,127] form the basis of flat optical devices, which may completely change the rules for optical designs.

From a logical consecution, let us first discuss the reflection and transmission on a subwavelength periodic metasurface that could be treated as homogenous. Using impedance theory and matching the boundary conditions [100,128], the modified Fresnel's equations is written as

$$r = \frac{1}{2}\left(\frac{2Y_0 - Y_e}{2Y_0 + Y_e} + \frac{Z_m - 2Z_0}{Z_m + 2Z_0}\right),$$
$$t = \frac{1}{2}\left(\frac{2Y_0 - Y_e}{2Y_0 + Y_e} - \frac{Z_m - 2Z_0}{Z_m + 2Z_0}\right), \tag{7}$$

where $Y_0 = 1/Z_0$ is the admittance of vacuum (the surrounding space), and $Y_e = 1/Z_e$ and $Y_m = 1/Z_m$ are the effective electric and magnetic admittance of the metasurface (Z is the corresponding impedance). This equation provides a means to arbitrarily control the wavefront on a structured interface [128,129]. For a slab with non-negligible thickness, the optical properties cannot be fully described by a single impedance; thus Eq. (7) is not valid. Instead, the reflection and transmission should be calculated using the transfer matrix, as demonstrated in multilayered systems [53,130]. Note that this matrix approach is equivalent to the multiple interference method widely used in optical textbooks [52,131].

Figure 16 shows the generalized Snell's law, or the so-called M-wave-assisted laws of refraction and reflection (MLRR) obtained by tuning the Fresnel's reflection or transmission [38]:

$$n_1 k_0 \sin\theta_i + \nabla\Phi_r(T) = n_1 k_0 \sin\theta_r,$$
$$n_1 k_0 \sin\theta_i + \nabla\Phi_t(T) = n_2 k_0 \sin\theta_t, \tag{8}$$

where $\nabla\Phi$ is the phase gradient in the surface plane, which is determined by the arrangement of subwavelength structures, and may be changed with time T by external stimuli such as electric and mechanic tuning. n_1 and n_2 represent the refractive index

of media at the incident and transmit sides. θ_i, θ_t, and θ_r are the angles for incident, refracted, and reflected light. Combined with the generalized Fresnel's equations, the MLRR has been widely adopted in the generation and transformation of an arbitrary wavefront across a thin sheet.

Figure 17 illustrates a hybrid numerical methodology used to simulate the transmission and reflection in an array of subwavelength structures (either periodic or aperiodic) [41,122]. First of all, the near-field electromagnetic responses of subwavelength structures must be solved using Maxwell's wave equation with rigorous numerical approaches such as FDTD, the finite element method (FEM), and methods of moments (MoM). When the scattered waves leave the subwavelength structures, vectorial diffraction theory may be used to calculate the far-field diffractions (either reflection or transmission). Since the diffraction could be calculated more efficiently than FDTD, FEM, and MoM, this hybrid approach has been taken in the design of large-area flat devices.

In a previous discussion of Fresnel's equations, it is assumed that the period of the subwavelength structure is much smaller than the wavelength; thus no diffraction effect is considered. In many cases, the subwavelength structures are placed above

Figure 16

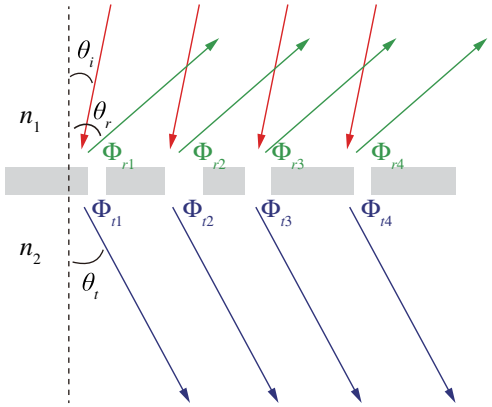

Beam deflection via constructive interference in a given direction. The transmitted and reflected phase shifts Φ_t and Φ_r are locally tuned by gradient subwavelength structures.

Figure 17

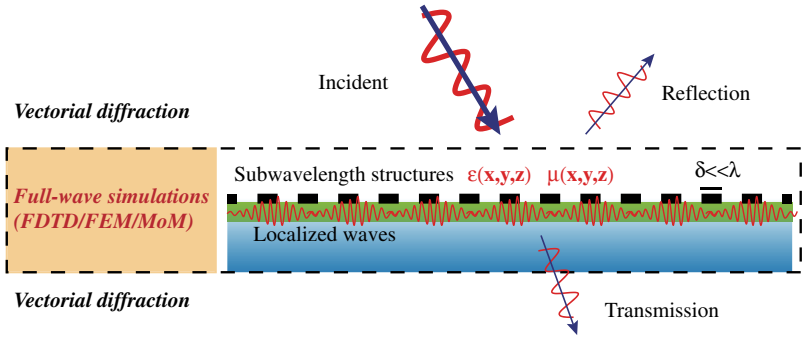

Hybrid simulation method. The re-radiation of the localized waves forms the reflection and transmission. For simplicity of discussion, periodic subwavelength structures are shown.

high-index substrates. When the effective wavelength of modes in the substrate becomes smaller than the period, diffraction in the substrate should be considered [44,132]. More interestingly, when the substrate forms waveguides, incident light may be converted to guiding modes via grating diffraction, leading to guided mode resonances [133,134]. According to the reciprocal principle, these guided modes may be reconverted into free space as reflection or transmission, which is similar to the leaky wave antenna. When the internal resonator loss equals the coupling loss, zero reflection could be expected. This condition is termed critical coupling, which has been observed as early as 1902 when Wood was investigating the diffraction spectrum [135], and utilized to design highly efficient optical absorbers [136,137] and couplers [138].

3.3. Localized Phase Modulation

As shown in Eq. (8), the key to realizing the generalized Snell's law is the gradient local phase shift. The following is a detailed discussion of three kinds of phase shift currently widely used in the literature [8,127,139].

3.3a. Propagating Phase

Plasmonic nanoslits shown in Fig. 18 are typical structures where propagating phase takes place. In general, these nanoslits are treated as F-P interferometers, where SPP modes propagate and bounce back many times to enhance the overall transmission. Using transfer matrix formalism, the phase retardation $\Delta\Phi$ is written as [34,39,140]

$$\begin{aligned} \Delta\Phi &= \mathrm{Re}(\beta h) + \delta, \\ \delta &= \arg[1 - (1 - \beta/k_0)^2(1 + \beta/k_0)^2 \exp(i2\beta h)], \end{aligned} \tag{9}$$

where δ originates from multiple reflections between the entrance and exit surface, h presents the length of the MIM waveguide, and β is the propagation constant of SPP. Both physical analysis and numerical simulation show that δ is small and βh

Figure 18

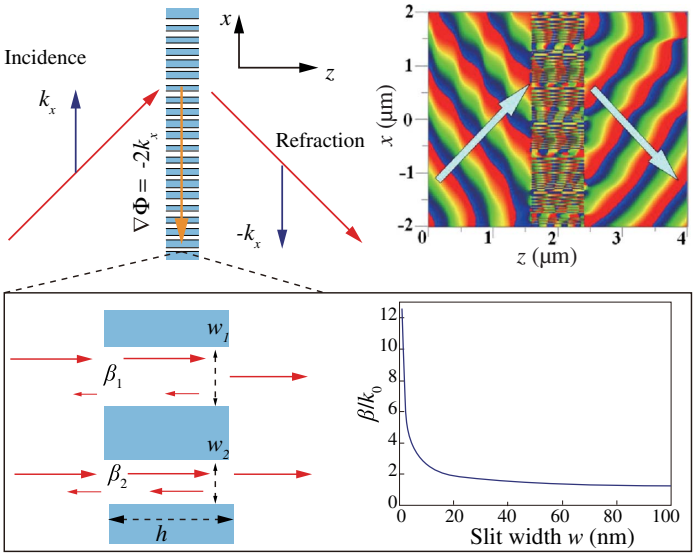

Schematic and numerical simulation of negative refraction based on gradient nanoslits array. The bottom panel shows surface plasmons propagating in the slits and the dependence of the propagation constant on the slit width. Adapted with permission from [39]. Copyright 2008 Optical Society of America.

plays a dominating role in the phase shift. As illustrated in the bottom of Fig. 18, β is a function of the slit width, and the phase retardation can be readily tuned by varying the width. Therefore, one can manipulate the wavefront almost arbitrarily, as demonstrated by a series of work including anomalous deflection [39], super-resolution focusing, and subwavelength imaging [34]. As an experimental demonstration, a TM-polarized wave with a wavelength of 637 nm was focused at the focal length of 5.3 μm with a full width at half magnitude (FWHM) of 0.88 μm and agreed well with the simulation results [35].

To remove the polarization dependence, 1D nanoslits may be replaced by circular or cross-shaped plasmonic holes with variable radius to generate polarization-independent phase modulation [36,37]. Besides lensing applications, such a holes array could also be used to realize optical vortices carrying spiral phase front [93]. Furthermore, simultaneous control of light polarization and phase distribution was achieved using more complex nanoslits [141]. Note that the focusing mechanism of these holes is completely different from the so-called photonsieves or nanosieves [142,143], which do not change the local phase front of the incoming waves.

Although metal supports strongly localized resonance through the coupling of photons and free electrons, unwanted loss of energy is inevitable owing to ohmic loss and inter-band transition in the visible regime [144]. Consequently, lots of efforts have been made to all-dielectric subwavelength structures to control the phase shift of light [145,146]. Similar to the plasmonic case, the dielectric rods or pillars can also be treated as waveguides and the propagation constant is tunable via the geometric parameters [147,148].

3.3b. Phase Shift Based on Surface Impedance

Huygens' principle is a well-known concept in optics that dates back to the 1690s. Recently, based on the generalized Fresnel's equations and Snell's law, it was applied to develop artificial surfaces that provide powerful control of electromagnetic wavefronts across electrically thin layers. These reflectionless surfaces, referred to as metamaterial Huygens' surfaces or Huygens' metasurfaces [128,129], provide new beam shaping, steering, and focusing capabilities. These metasurfaces are realized with 2D arrays of subwavelength structures that provide both electric and magnetic polarization currents to tune the impedances shown in the generalized Fresnel's equations.

In the microwave regime, pure metallic subwavelength structures commonly used in metamaterials are sufficient to tune the electric and magnetic resonances. This kind of Huygens' metasurface was demonstrated by a beam deflector with transmission efficiency of 86%, where copper lines provide the electric polarization currents while split-ring resonators provide the magnetic polarization currents [128], as illustrated in Fig. 19. By using stacked unit cells comprising aluminum-doped zinc oxide (AZO) and silicon and applying the optical nanocircuit concepts to metasurfaces, surfaces supporting both electric and magnetic polarization currents were also designed in the mid-infrared band [149].

Although Huygens' surfaces have been successfully demonstrated in the microwave and mid-IR spectral ranges, transferring it to near-IR and visible wavelengths remains challenging owing to the weak magnetic responses and considerable dissipation losses of plasmonic structures at optical frequencies. Recently, this concept was extended to the near-infrared band by using stacked gold structures to efficiently refract normally incident light at a wavelength of 1.5 μm [129]. Alternatively, dielectric resonators with Mie-type resonances have also been investigated owing to their smaller loss [150,151].

Besides Huygens' metasurfaces mentioned above, multilayered transmitarrays [152,153] and reflectarrays [154,155] composed of metallic subwavelength structures in transmission or reflection mode have been utilized to enhance the efficiency of the metasurface. In principle, the optical properties of these structures could be modeled by combining the generalized Fresnel's equations and the transfer matrix. Since the distance between each layer is large enough, the magnetic response could be ignored. Taking a three-layered reflective configuration, i.e., the generalized GTI, as an example (Fig. 20), the reflection coefficient is obtained using transfer matrix [53]:

Figure 19

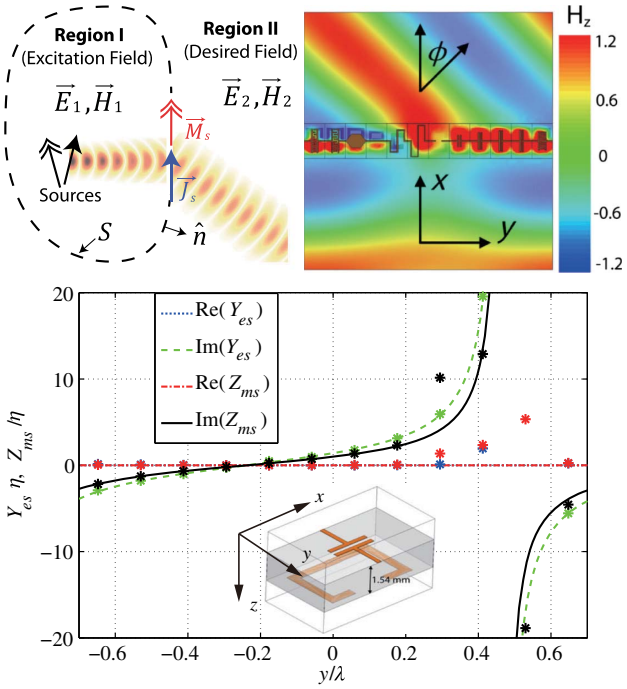

Huygens's metasurface with matched electric admittance (Y_{es}) and magnetic impedance (Z_{ms}). Top right shows the simulated magnetic field distribution, and the bottom shows the normalized impedances for each resonator in a period. Figures 1 and 2 adapted with permission from Pfeiffer and Grbic, Phys. Rev. Lett. **110**, 197401 (2013) [128]. Copyright 2013 American Physical Society.

Figure 20

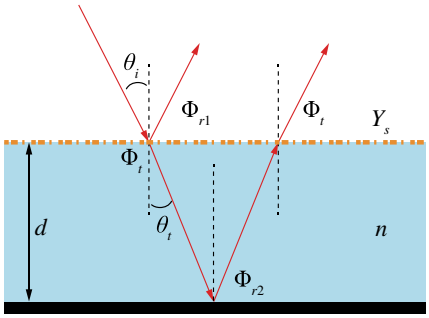

Schematic of the generalized GTI composed of a metasurface, a dielectric spacer, and reflective ground plane.

$$r = \frac{(Y_0 - Y_s - Y_1)\exp(-ink_0 d) + (Y_0 - Y_s + Y_1)\exp(ink_0 d)r_m}{(Y_0 + Y_s + Y_1)\exp(-ink_0 d) + (Y_0 + Y_s - Y_1)\exp(ink_0 d)r_m}, \tag{10}$$

where r_m is the reflection coefficient of the background plane; Y_0, Y_1, and Y_s are the admittance of free space, the dielectric spacer, and the metasurface; and n is the refractive index of the dielectric spacer. By controlling Y_s via geometric parameters, the reflection amplitude and phase could be tuned. More specifically, if the dielectric spacer is lossless and Y_s is pure imaginary, the reflection amplitude would be unity, leading to pure phase modulation. For an intuitive understanding, we shall consider the phase shift between the first and second reflection:

$$\Delta\Phi = \Phi_{r1} - \Phi_{r2} - 2nk_0 d\cos\theta_t - 2\Phi_t, \tag{11}$$

where Φ_{r1} and Φ_{r2} represent the reflection phase shift at the first and second interfaces, Φ_t is the transmission phase shift of the first interface, and θ_t is the refraction angle. Since both Φ_{r1} and Φ_t are tunable via the subwavelength surface structures, the phase-matching condition may be readily controlled.

For many metallic subwavelength structures, the impedance could be understood by equivalent circuit models comprising equivalent inductors, capacitors, and resistors [53,156]. The inductance L is related to the current distribution in metallic structures, and the capacitance C results from the electric fields in the gaps between metallic elements.

3.3c. Geometric Phase

Geometric phase is a novel phase shift not usually exploited in classical optics. Although there are only renewed interests in recent years [45,157], investigations of geometric phase actually date back to as early as 1947 [158], when a birefringent waveguide was used as a microwave phase shifter. In another work [159], it was also shown that the phase of the output voltage of a circularly polarized antenna was proportional to the angle of rotation of the antenna along its longitudinal axis. With regard to optics, Pancharatnam proved that the geometric phase is involved with the interference of polarized light in 1956 [160]. In the famous work of Berry [161], it was shown that an adiabatic change of the quantum state can introduce a geometric phase shift, and this phenomenon is related to the Aharonov–Bohm effect. In memory of the scientific contributions of Pancharatnam and Berry, the geometric phase is also known as the Pancharatnam–Berry phase [162,163].

As far as we know, the first functional optical components based geometric phase, or the so-called topological phase, was proposed in 1997 [164], although similar devices working at the microwave frequency were demonstrated earlier [154,159]. As plotted in Fig. 21, a geometric phase lens can be constructed by sandwiching a spatial-variant half waveplate (HWP) between two quarter waveplates (QWPs). The HWP is divided into annular rings so that the principal axis in a given annular ring at a radial distance r from the center is rotated through a certain calculated angle. When a 45° linearly polarized light passes through these cascaded devices, it is first converted to circular polarization and then transformed into its cross-polarization with designed phase profile, and finally converted back to linear polarization.

The geometric phase can be understood by applying the transfer matrix to two orthogonal directions in the local coordinates aligned with the main axes of the HWP. Under circular polarization incidence with the Jones matrix of $[1, i\sigma]^T$, the output fields passing through the HWP are [41]

$$\begin{bmatrix} E_x \\ E_y \end{bmatrix} = \frac{1}{2\sqrt{2}}\left((t_u + t_v)\begin{bmatrix} 1 \\ i\sigma \end{bmatrix} + (t_u - t_v)e^{2i\sigma\zeta}\begin{bmatrix} 1 \\ -i\sigma \end{bmatrix}\right), \tag{12}$$

where t_u and t_v are the transmission coefficients along the two main axes, and $\sigma = \pm 1$ denotes the LCP and RCP, respectively. Clearly, the output fields are composed of two circular polarizations with opposite handedness. The additional phase of the counter-rotating polarization $2\sigma\xi$ is purely geometrical and independent of the working frequency. Note that Eq. (12) is equally suitable for a reflective device when t_u and t_v are replaced by the reflection coefficients r_u and r_v.

Although very compact and efficient, the geometric lens is difficult to realize with traditional optical fabrication methods. As a simplification of this design, a polarizing grating that deflects differently polarized light into opposite directions was proposed [165]. Following this concept, a computer-generated optical subwavelength grating was designed and experimentally characterized for polarization-dependent beam deflection and focusing in the infrared band [166,167]. With the development of advanced micro/nano-fabrication technology in recent years, similar structures were extended to the visible band [168,169].

Since geometric phase relies on the anisotropic transmission, the thickness of anisotropic dielectric structures must be comparable to the wavelength to induce a significant effect. In contrast, metallic subwavelength structures could induce strong anisotropy with a nanometer thickness and broadband response. In an ideal condition, such geometric phase is only proportional to the orientation angle of nanoantennas; thus it is easy to obtain a phase variation covering the full 0–2π range without an extra look-up table. By arranging dipole antennas in an array with a constant phase gradient along an interface, broadband anomalous refraction was observed at visible to near-infrared wavelengths [170,171]. By combining the focusing phase and binary phase modulation, an ultra-broadband superoscillatory flat lens was further proposed and realized [125]. As demonstrative examples, sub-diffraction focal patterns for ultra-broadband wavelengths spanning visible and near-infrared were realized in experiments. In addition, the out-of-plane focusing metalens (the focal spot is not located on the plane of incidence) with three wavelengths in a multiplex unit cell was designed for a CMOS image sensor [172].

Although geometric phase is nearly achromatic, the effective bandwidth is often narrow since the spectrum of polarization conversion often shows a resonant line. In a recent work shown in Fig. 22, quasi-continuous metasurfaces for high-efficiency and broadband beam deflection were demonstrated based on the unique properties of catenary structures [41,173]. The geometric phase could be calculated using the local orientation angle, which is found to follow a perfect linear function. Far-field experimental results of both single and arrayed catenaries indicate that the incident beam

Figure 21

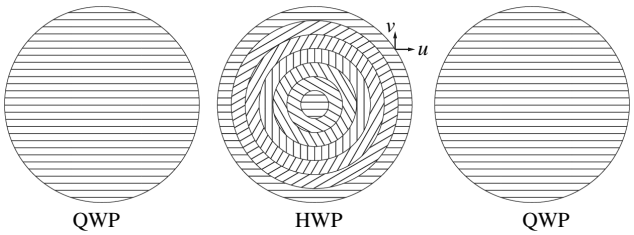

Cross sections normal to the beam of the three elements constituting a geometric phase lens. The first and the third elements are QWPs, and the middle element is a HWP whose principal axis is oriented at an angle that is a function of the radial distance from the center. Adapted with permission from Phys. Rep. **281**, Bhandari, "Polarization of light and topological phases," 1–64. Copyright 1997 [164].

deviates from the normal direction after transmitting through the nanoapertures [41,78,174]. Owing to the elimination of circuit resonance in discrete structures, the efficiency of this design approximates to the theoretical limit (25%) of the single-layer metasurface in a broad frequency range, which was also demonstrated in the microwave frequency [Figs. 22(c) and 22(d)] [173]. Note that a catenary-shaped chain of nanohole arrays with anisotropic coupling could also realize a similar effect but with less bandwidth and efficiency [175].

To achieve complete polarization conversion and high-purity geometric phase, the thickness of the resonators must be increased to realize both amplitude and phase modulation. As indicated by Eq. (12), the maximal efficiency is obtained when each unit cell behaves as a transmissive or reflective HWP. As shown in Fig. 23, there are

Figure 22

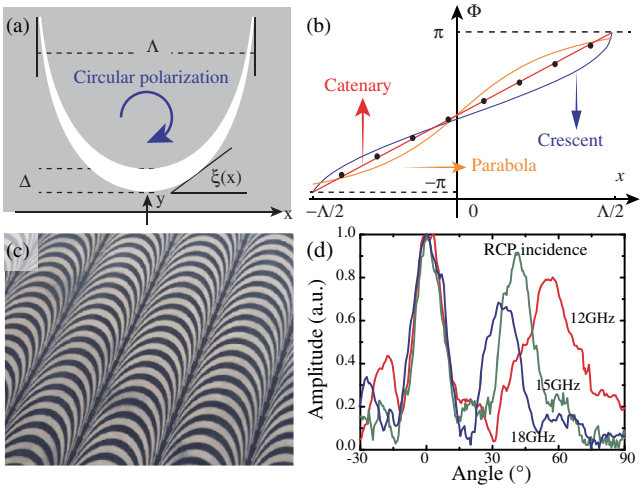

Geometric phase in catenary metasurfaces. (a), (b) A single catenary aperture and its geometric phase along the x direction. The phase functions for parabola and crescent shapes are also shown for comparison. Adapted with permission from [41] under the terms of the Creative Commons Attribution NonCommercial License. (c), (d) Photograph and measured results for a linear array to realize broadband beam deflection in the microwave frequency. Adapted with permission from [173] under the terms of the Creative Commons Attribution 4.0 License.

Figure 23

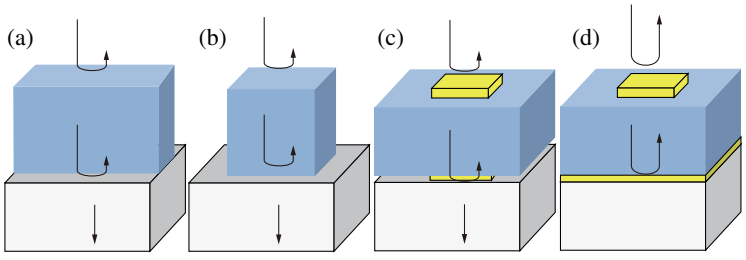

Four fundamental anisotropic structures for efficient geometric phase generation. (a), (b) Transmissive elements based on (a) high-index dielectric grating and (b) nanorods. (c) Transmissive element based on metal–dielectric multilayers. (d) Anisotropic reflective element.

generally two kinds of resonators: the first is dielectric, and the second is metallic. Obviously, the mechanism for efficiency enhancement is just the multiple interference of the reflection/transmission at each interface. As a result, when the subwavelength interference condition is met, the thickness of the overall structure is minimized. The early type geometric metasurface is based on form-birefringence in high-index dielectric material [Fig. 23(a)] [167,168], which has finally evolved into an anisotropic nanopillar array [Fig. 23(b)] [44,169]. The metallic resonators are built on previous studies on the polarization converters, either transmissive [Fig. 23(c)] [176,177] or reflective [Fig. 23(d)] [83,85,178,179].

Combining the surface resonance and geometric phase, it is also possible to change the phase in the process of polarization conversion from linear to its cross-polarized state [40,86,180]. As illustrated in Fig. 24, the anisotropic resonant properties of the V-shaped antennas allow one to design the amplitude, phase, and polarization state of

Figure 24

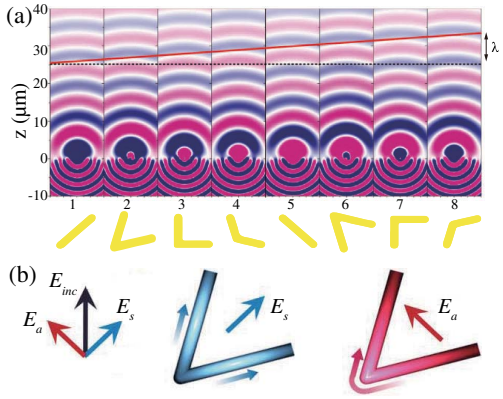

Phase modulation based on V-shaped antennas. (a) Instantaneous electric field distribution for eight V-shaped nanoantennas. (b) Symmetric and asymmetric resonant modes. From Yu *et al.*, Science **334**, 333–337 (2011) [40]. Adapted with permission from AAAS.

Figure 25

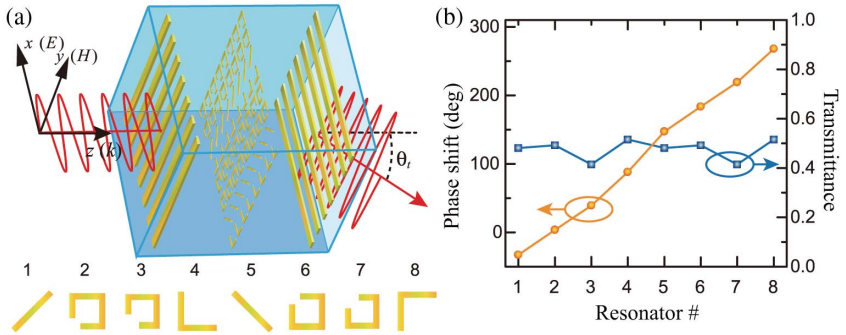

(a) Transmissive anomalous refraction based on linear polarization conversion. A normally incident x-polarized wave is converted to a y-polarized beam, which bends to an angle θ_t with respect to the z axis. (b) Calculated phase shifts and transmittance for the eight resonators. From Grady *et al.*, Science **340**, 1304–1307 (2013) [86]. Adapted with permission from AAAS.

the scattered light. By exploiting eight dedicatedly designed nanoantennas with phases in $\pi/4$ increment and nearly equal amplitude, anomalous reflection and refraction phenomena were experimentally demonstrated in the mid-infrared spectral range [40]. The tunability of such structures is associated with the symmetric and anti-symmetric resonant modes shown in Fig. 24(b). Meanwhile, geometric phase also exists in such structures, since a 90° rotation of elements 1–4 is used to generate an additional phase shift of 180° in elements 5–8 [38]. By simply scaling the geometric size, near-infrared demonstration and three-dimensional (3D) extension of the generalized laws with non-coplanar refraction and reflection were realized subsequently [181,182].

According to Babinet's principle, V-shaped apertures perforated in a metallic screen have a similar optical response to their complementary structures and have been used to create flat lenses to focus visible light [183]. Owing to the capability of simultaneous amplitude and phase modulation, they have also been utilized for high-fidelity computer-generated holography (CGH) with thickness down to 30 nm [184]. Besides, by designing a metasurface with a rapid gradient of phase discontinuity along the interface in the x direction, one can introduce a strong spin-orbit coupling and photonic spin Hall effect when light is refracted off the interface [185].

Single-layered metasurfaces based on either V-shaped or C-shaped [180] antennas operate in the cross-polarization conversion mode and thus suffer from limited polarization conversion efficiency. In principle, the efficiency could be raised at the cost of larger thickness. This was proved by constructing a bilayer plasmonic metasurface operating at visible frequencies by coupling a nanoantenna-based metasurface with its complementary Babinet-inverted copy [186]. Such a coupled bilayer metasurface experimentally yields conversion efficiency significantly larger than that of single-layer designs, as well as an extinction ratio larger than 0 dB, which means that anomalous refraction dominates the transmission response. In another design illustrated in Fig. 25, eight anisotropic resonators with various geometries and dimensions in a super-unit-cell are used to create a linear phase variation of the cross-polarized transmission. Two additional orthogonal gratings are used to boost the conversion efficiency.

Coherent illumination is also a promising way to overcome the above theoretical limit on efficiency. Inspired by the coherent perfect absorption [187,188], it was demonstrated that coherent control could be used to dramatically enhance the polarization conversion and phase modulation efficiency of metasurfaces [189–191]. Normal and anomalous beams following the generalized Snell's law can be strongly modulated and separately switched on/off by changing the phase difference between two counter-propagating coherent control and signal beams. In principle, anomalous deflection efficiency can increase up to 100% when the signal and control beams are in-phase, while the anomalous beams vanish when the phase difference is equal to 180° [191].

4. APPLICATIONS OF LAYERED STRUCTURES

The interference of light in layered structures has been well studied in classical optics and photonic crystals with applications including filters, anti-reflection films, and all-dielectric reflectors [192,193]. However, owing to the limited refractive index considered in traditional devices, the full potential of multilayered structures has only been exploited in recent years. In this section, the subwavelength interference in three kinds of layered structures is reviewed, with particular emphasis on their applications in optical imaging, nanolithography, and absorbing materials.

4.1. Superlens and Plasmonic Surface Lenses

In classical optics, metallic films are typically used as reflectors in mirrors. When the thickness of the film is larger than the skin depth, the transmission coefficient is

negligible. The early study of a translucent metal film dates back to the late 19th century, when Faraday found that gold leaf could transmit green light and reflect the yellow part of incident light [194]. In the middle of the 20th century, it was discovered that a thin metal film may support a collective excitation of free electrons, i.e., the SPP at metal surfaces. In principle, SPP can be excited using either an optical or an electronic approach [195–197]. Besides metallic film, metallic nanoparticles also support SPP, where light is localized and enhanced in a region much smaller than the wavelength [198].

In the early 2000s, the importance of SPP was brought back by interest in the EOT phenomenon [21], negative index material (NIM) [20], and the EYI effect [17]. In an EOT experiment, anomalous transmission peaks are observed when light is transmitted through nanoholes perforated in a metallic film. Compared with standard aperture theory, the overall transmission is enhanced by nearly 100 times. From a microscopic view [23], this was explained using the interplay of SPP propagating on surfaces. In an independent work to revisit the planar lens made of NIM proposed by Veselago half a century ago [Figs. 26(a) and 26(b)] [200], Pendry showed that SPP in a thin metallic film could increase the near-field resolution by amplifying the evanescent wave [Fig. 26(c)] [20,199]. As a quasi-static NIM, this metallic film is called a superlens.

In addition to continuous metal film, the optical properties of discontinuous film have also been investigated by many groups. By replacing typical chromium with silver in a photomask, Luo and Ishihara obtained an interference pattern much smaller than the traditional case at the metal surface (the center-to-center distance of the interference fringes is about 50 nm at a wavelength of 436 nm) [17], which is attributed to the excitation of SPP with greatly reduced effective wavelength. Resulting from the constructive interference at the front surface, light transmission through the photomask is boosted to be much higher than that predicted by standard aperture theory, as described in detail in another experiment [19].

In the rudimentary experiment of super-resolution surface plasmon lithography [17], the silver mask simultaneously acts as the object and the lens. In many other cases, the two roles are separated and the object–image relation is described using OTF curves.

Figure 26

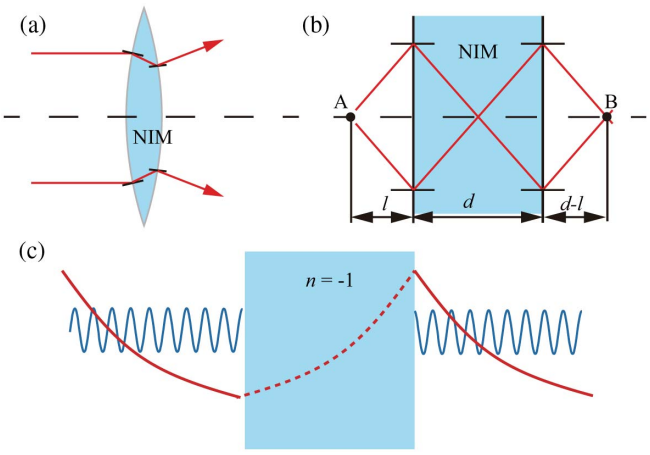

Perfect lens based on NIM. (a) NIM convex lens divergent incident collimated beam. (b) NIM flat slab acting as a lens. (c) Evanescent wave amplification. Adapted with permission from Macmillan Publishers Ltd.: Zhang and Liu, Nat. Mater. **7**, 435–441 (2008) [199]. Copyright 2008.

As outlined in Subsection 3.1, the imaging process can be treated as the interference of all the diffraction orders. In a continuous metallic film, the plasmonic resonances act as amplifiers for these rapidly decaying waves. Using a lithographic process similar to the previous configuration, other groups directly validated the superlens proposed by Pendry [201,202]. Besides 1D interference imaging, 2D patterns with a minimal linewidth of 89 nm have been obtained using a light source operating at 365 nm. Figure 27 describes the sketch map and OTF of a 35-nm-thick silver film for TE and TM polarizations. Clearly, the silver film has led to a high transmission peak located in the high-spatial-frequency region for TM polarization, owing to the excitation of SPP. Note that SPP in a continuous film can only be excited by near-field sources, such as the grating, prism, and photomask. This is why this phenomenon cannot be observed in the traditional far-field imaging process.

There are several methods to increase the resolution and imaging contrast of the superlens. First, high-quality silver film is pursued because the roughness of the silver film will enhance the random scattering of high spatial frequency [17,203]. Second, the loss of materials should be carefully designed to make a compromise of the resolution and fidelity, since low loss is not always wanted in the imaging process [204]. Third, multilayered structures could be employed to excite high-order SPP modes and realize higher resolution [117,205]. It has been demonstrated that a MIM cavity is a near-ideal candidate for super-resolution imaging. In such a system, the first metal layer acts as a superlens, and the second metal layer is used as a reflector to control the vectorial properties of light fields and to enhance the image quality. The combination of superlens and reflective layer is similar to the traditional catadioptric system, where both transmission and reflection are used to realize high-performance imaging [118]. The forward- and backward-propagating evanescent fields sum within the photoresist to produce a waveguide mode with an ideally symmetric catenary intensity profile, which is beneficial to increase the focal depth [18,33,89].

Figure 28 shows a plasmonic cavity lens operating at a wavelength of 365 nm, and the bottom shows the electric field distribution for the symmetric eigenmode (defined by the symmetry of E_x). Note that the anti-symmetric mode often used for interference lithography [31,117] is not shown. Owing to the resolution enhancing capability of such lenses, the air gap between the mask and substrate has been increased by about 10 nm compared with the classical superlens. As a result, damage to the mask in the

Figure 27

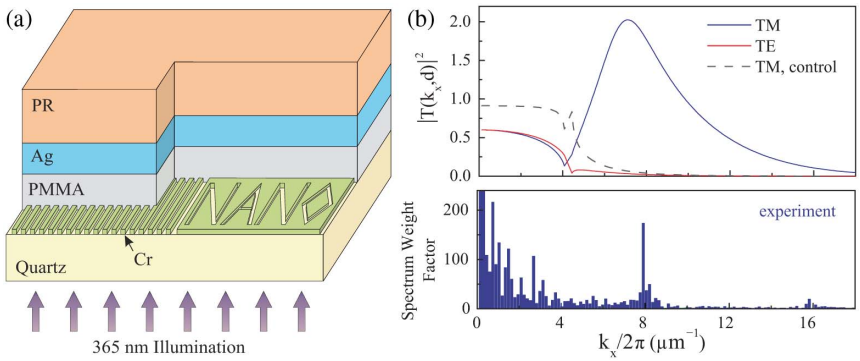

Super-resolution imaging with a single silver film. (a) Configuration of the experiment. (b) Theoretical and experimental transmittance spectrum. From Fang *et al.*, Science **308**, 534–537 (2005) [202]. Adapted with permission from AAAS.

photolithographic process would be minimized, thus ensuring batch fabrication of functional devices [69]. For example, meta-hologram devices composed of nanoapertures with unit size of about 95 nm × 175 nm and a period of 300 nm have been successfully fabricated by the plasmonic cavity lithography and multilayer etching transfer technologies [91].

For interference lithography, the anti-symmetric (odd) modes possess much higher transversal wavevector and greater inhibition of tangential electric field components, facilitating surface plasmon interference fringes with superior resolution and contrast in terms of electric field intensity [90]. An inverse design procedure employing a genetic algorithm (GA) was utilized to optimize the results at a wavelength of 193 nm [33]. Interference patterns with a half-pitch of 5.05 nm ($\sim\lambda/40$) corresponding to an effective NA of 20 have been numerically demonstrated.

Although electromagnetic fields of SPPs decay exponentially normal to the metal–dielectric interface, their transverse propagation lengths may reach tens to thousands of micrometers for noble metals, allowing the realization of 2D plasmonic components and even integrated photonic circuits. With appropriately designed subwavelength structures, SPPs may interfere constructively and focus into a highly confined spot with a size beyond the diffraction limit, as demonstrated by using circular slits [206] or nanometric holes arranged on a quarter circle [207]. Owing to the symmetry mismatch between the linearly incident polarization and circular structures, the longitudinal fields always have a minimum at the geometric focus due to destructive interference between counter-propagating SPPs; thus the overall intensity could not reach the maximum. To realize constructive interference at the focus, structures with broken symmetry have been adopted [208]. By generating an extra phase shift between counter-propagating SPPs via a radius mismatch of $\lambda_{spp}/2$, one can regulate the total phase of the electric field at the center, as shown in Figs. 29(a) and 29(b).

Based on the holography principle, complex surface structures beyond simple circles or spirals were designed to realize many functionalities, including controlling surface waves traveling on metal surfaces [210,211], detecting optical vortex beams with

Figure 28

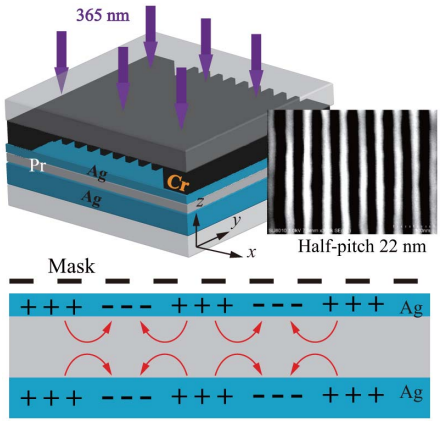

Top: schematic of the cavity lens and the SEM image of resist pattern with 22 nm half-pitch. Bottom: electric field and charge distribution for the symmetric mode. Although it has a relatively smaller horizontal wavenumber than the anti-symmetric mode, the symmetric mode can greatly increase the imaging contrast and working distance. Adapted with permission from Gao *et al.*, Appl. Phys. Lett. **106**, 093110 (2015) [32]. Copyright 2015 AIP Publishing LLC.

specific OAM [212], and exchanging information between surface waves and propagating waves [30,213,214]. In particular, by locating an array of metallic slits in a way that it matches the desired complex field distribution, an integrated device for 2D plasmonic Airy beam generation was obtained [215]. As shown in Fig. 29(c), a double-lined nanoslit array configuration could be employed for the generation of plasmonic complex fields [209], where each nanoslit has its own tilted angle. The amplitude of the SPP can be tuned via the angular difference between two nanoslits, whereas the phase is controlled by the offset rotation angle. Similarly, by creating a running wave of polarization along a list of subwavelength spaced rotated apertures that propagate faster than the SPP phase velocity, a 2D analogue of Cherenkov radiation was generated [216]. In addition, surface waves may be efficiently manipulated by referring to the transformation optics [217,218]. As a proof-of-concept example, a plasmonic Luneburg lens and an Eaton lens were demonstrated by solely modifying the thickness of a dielectric material on top of a metal [219]. The phase front appears flat when launched at the grating and starts to bend inside the lens, leading to focus on the perimeter.

4.2. Hyperbolic Lenses

SPPs are generally strongly confined to the near field of metallic film. However, when an additional film of noble metal is introduced, they tend to couple together to form complex waveforms, which may have a much smaller effective wavelength than common SPPs at a single interface. On the deep-subwavelength scale, these films can be homogenized as an effective material with unusual dispersion diagram (see Subsection 3.1), such as that dubbed hyperbolic dispersion [108,220]. In the last decade, multilayers with hyperbolic dispersion have been widely used to tailor the spatial frequency and form deep-subwavelength interference patterns.

In photonic crystals, the relation $\rho(\omega) \sim k^3$ presents the possibility of controlling the photonic density of states via tuning the dispersion relation [221]. By probing the

Figure 29

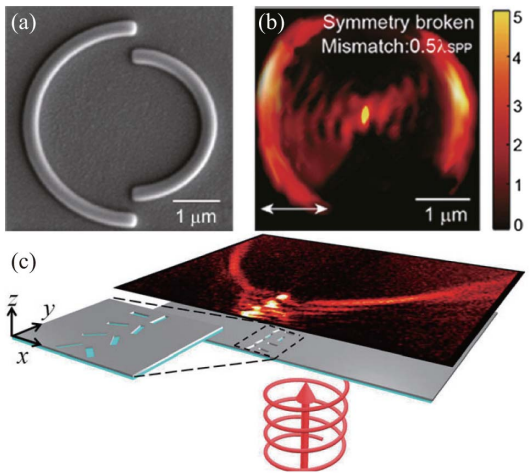

Surface plasmon focusing and beam shaping. (a), (b) SEM of the asymmetric structure and measured intensity distribution under linearly polarized incidence. Adapted with permission from Fang *et al.*, Nano Lett. **11**, 893–897 (2011) [208]. Copyright 2011 American Chemical Society. (c) Schematic and measured Airy beam produced by double-lined nanoslits array. Song *et al.*, Laser Photon. Rev. **10**, 299–306 (2016) [209]. Copyright Wiley-VCH Verlag.

available local density of states in the near field of the metamaterial using spontaneous emission of dyes, it was shown that the hyperbolic material has led to a strong decrease in the lifetime of emitters. Based on a similar mechanism, the near-field thermal radiation could be greatly enhanced to realize super-Planckian thermal emission [115]. According to the definition of group velocity $v_g = \nabla\omega_k$, the direction of the energy flow is restricted to be perpendicular to the tangent of the dispersion curve [108], which was experimentally demonstrated by using an Ag/SiO_2 multilayer [222]. As illustrated in Fig. 30, the direction of group velocity is perpendicular to the equi-frequency lines. The approximate propagation angle is calculated by $\tan\theta = \sqrt{-\mathrm{Re}(\varepsilon_x)/\varepsilon_z}$. When $|\varepsilon_x| \ll |\varepsilon_z|$, the dispersion curve is flattened and all spatial components will constructively interfere and propagate in a nearly straight line without diffraction; thus the ray optics could be scaled to a dimension smaller than the wavelength [109,110].

The directional propagation effect was also observed in a hyperbolic metasurface composed of a single-crystalline silver grating at visible frequency [223]. When SPPs are excited by the incoupling structure, they split into two separate (left- and right-ward) beams along symmetric directions and are detected at the outcoupling structure. More interestingly, surface plasmons in the surface grating bear circular polarization, and this directional propagation is also termed one kind of photonic spin Hall effect, which has potential applications ranging from imaging and sensing to quantum optics and quantum information science.

Hyperbolic lenses can be used to realize demagnifying interference lithography. Figure 31 shows dense lines with 45 nm half-pitch resolution ($\sim\lambda/8$) obtained by adding a multilayer on the plasmonic cavity lens [117]. As the layer number increases, the spatial spectrum becomes more pure, and the intensity distribution is more uniform.

The evanascent wave filtering property has many other applications, including asymmtric transmission [205], near-field Bessel beam generation [92], and surface microscopy [224,225]. As illustrated in Fig. 32, by changing the mask from a common grating to a concentric grating, such multilayers can be utilized to realize 2D spectral filtering and to generate near-field Bessel beams [92]. The experimental results proved that a focusing spot with diameter ~65 nm could be achieved at the distance of 0, 40, and 80 nm for an illumination wavelength of 365 nm. In another experiment, a deep-subwavelength bulk plasmon polariton mode was launched in metal/dielectric multilayers to realize surface microscopy with ultra-short illumination depth and uniform

Figure 30

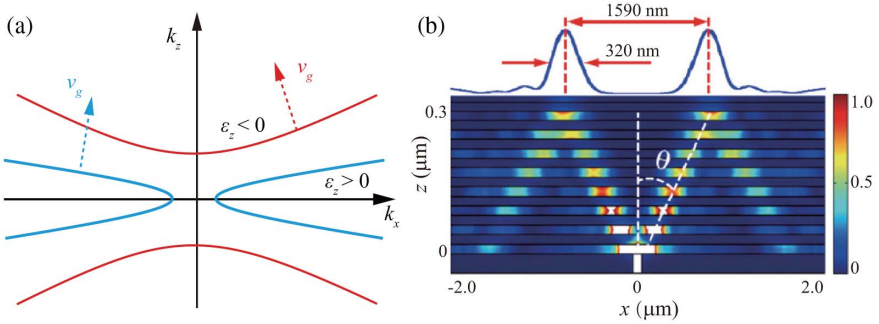

Directional propagation of light in hyperbolic multilayers. (a) Schematic of two hyperbolic dispersion curves. (b) Calculated intensity distribution corresponding to the blue dispersion curve shown in (a). Adapted with permission from Wang *et al.*, Appl. Phys. Lett. **103**, 031911 (2013) [222]. Copyright 2013 AIP Publishing LLC.

illumination field [224,225]. An illumination depth as short as 25 nm in air was achieved. Moreover, by simply changing the incidence angle of the excitation beam, the transverse wavevector of the launched single bulk plasmon polariton mode could be tuned.

Based on the directional propagation of SPPs in hyperbolic materials, Salandrino and Engheta theoretically proposed far-field optical microscopy with a sub-diffraction resolution, also termed as a magnifying superlens [226]. They exploited the metamaterial

Figure 31

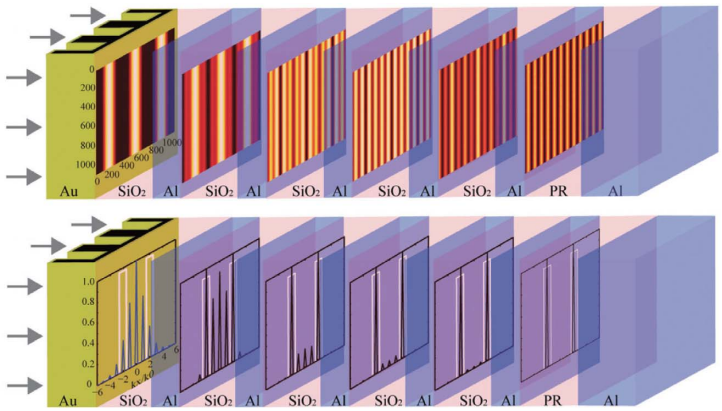

Planar multilayer for spectral filtering and demagnifying lithography. Top: light intensity distribution inside multilayers. Bottom: spatial-frequency spectra normalized to their maximum value. Liang *et al.*, Adv. Opt. Mater. **3**, 1248–1256 (2015) [117]. Copyright Wiley-VCH Verlag.

Figure 32

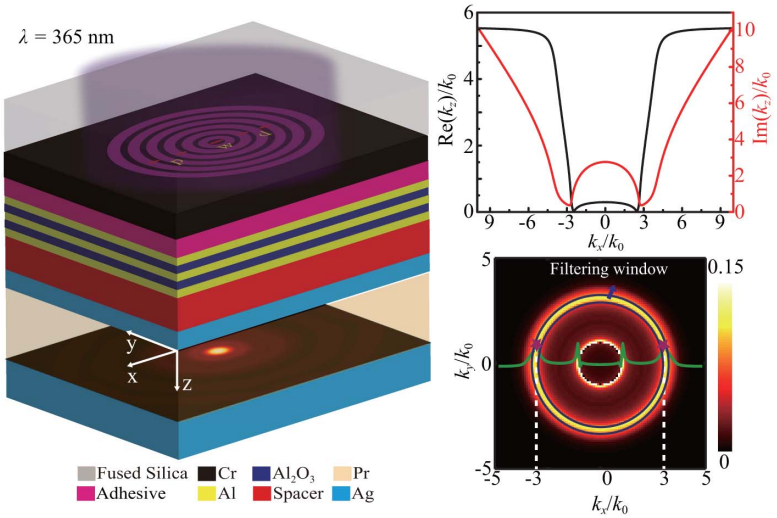

Schematic of the hyperbolic lens for the evanescent Bessel beam generation under circular polarization illumination. Top right shows the calculated real (black curve) and imaginary (red curve) parts of longitudinal wavevector k_z for variant tangential wavevector k_x at a wavelength of 365 nm. Bottom shows the 2D OTF versus the tangential wavevector. Adapted with permission from Liu *et al.*, Mater. Horiz. **4**, 290–296 (2017) [92]. Copyright 2017 Royal Society of Chemistry.

crystal that is obliquely cut at its output plane, or has a curved output surface to map the input field distribution onto the crystal's output surface with a compressed angular spectrum, resulting in a "magnified" image. Based on a similar operation scheme, the concept of "hyperlens" was proposed in the same year [227]. Owing to the conservation of angular momentum, a magnified image carried by low wavevectors will ultimately be formed at the outer boundary of the hyperlens before propagating into the far field. The magnification at the output surface is given simply by the ratio of the radii at the two boundaries. Then conventional microscopy can be utilized to capture the output fields to achieve far-field super-resolution imaging. As shown in Fig. 33, a cylindrical optical hyperlens in ultraviolet frequencies was constructed by exploiting the Ag-Al_2O_3 multilayer [111], through which a sub-diffraction-limited object (with a 130 nm center-to-center distance) was observed by a conventional lens in the far field. Similarly, a spherical hyperlens with 2D super-resolution capability was experimentally demonstrated in the visible spectral region [228].

According to the reciprocity theorem, by simply reversing the operation direction of the hyperlens [229,230], a mask with diffraction-limited dimensions can be demagnified into a sub-diffraction-limited one in plasmonic nanolithography [112]. Figure 34(a) shows the hyperlens composed of multiple Ag/SiO_2 films, which has a sub-diffraction resolution of about 55 nm linewidth and a demagnification factor of 1.8 at 365 nm wavelength. Using a laser source operating at 405 nm, a similar experiment with a resolution of 170 nm linewidth was also demonstrated [113].

It should be mentioned that the curved geometry of a (de)magnifying hyperlens causes difficulty in the practical implementation and applications. A simple method for a planar imaging profile is to cut and polish the hyperlens on one or both sides [229]. But this operation seems challenging for fabrication and usually results in the deformation of images. As an alternative, a hybrid lens combining a hyperlens with a planar superlens was proposed [Fig. 34(b)] [109,231,232], but the demagnification ratio is often not uniform on the entire object/imaging plane. To solve this

Figure 33

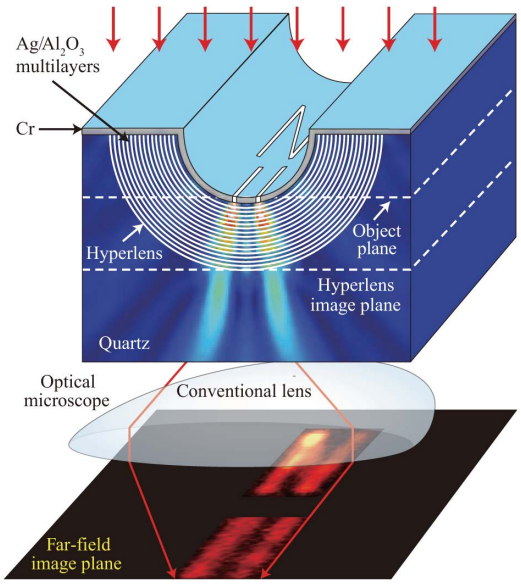

Magnifying hyperlens used for imaging of sub-diffraction-limited objects. From Liu *et al.*, Science **315**, 1686–1686 (2007) [111]. Adapted with permission from AAAS.

problem, a conformal transformation approach involving a Hermite interpolating polynomial was recently proposed to design planar input and output surfaces with uniform demagnification [233]. By using cascaded multilayers for further demagnification, imaging results with about $\lambda/23$ (16 nm) half-pitch resolution were demonstrated.

Since the diffraction limit is universal for all kinds of wave phenomena, the resolution of conventional acoustic imaging is also limited by the wavelength of the sound wave. Acoustic metamaterials [234,235], superlenses [236], and hyperlenses [237] aimed to improve the spatial resolution have been introduced by many research groups. Analogous to the SPPs excited at the metal–dielectric interface, there are also acoustic surface states at the interface between two semi-infinite media with mass densities of opposite signs. The dispersion curve of the surface state asymptotically reaches infinity at the mass density match point, implying a super-resolution imaging ability.

Note that not all metal–dielectric multilayers can be approximated to be hyperbolic or elliptic dispersion. The effective dispersion diagram will be much stranger if more than two different layers are used as a unit cell of the multilayer stack. For example, Xu *et al.* used five-layer films as a unit cell, and demonstrated an omnidirectional left-handed response for TM polarization [238]. By engineering the structure to have a refractive index close to -1 over a broad angular range, they achieved flat lensing of arbitrarily shaped 2D objects beyond the near field. Interestingly, the hat-like dispersion curve for the multilayer is neither hyperbolic nor elliptic. In a follow-up work, it was shown that such a dispersion is a consequence of the interference of complex Bloch modes [239]. As a result, besides the mode showing negative refraction, there are other modes that behave in a right-handed manner.

4.3. Thin-Film Absorbers

In traditional thin-film interference theory, materials are often lossless, and the refractive indices are real numbers. In this subsection, we show that the large imaginary part of the metallic thin film may lead to many unusual interference effects. Since the

Figure 34

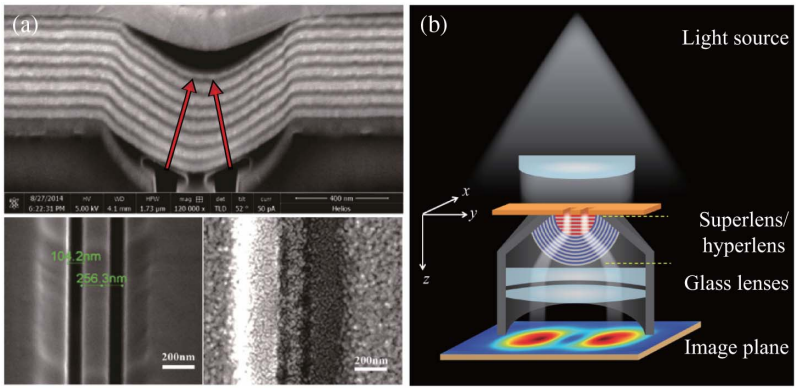

(a) Top: schematic and SEM of the demagnifying hyperlens. Bottom: SEM images of the mask and photoresist patterns with a demagnifying ratio of 2:1. Adapted with permission from Liu *et al.*, RSC Adv. **6**, 95973–95978 (2016) [112]. Copyright 2016 Royal Society of Chemistry. (b) Schematic of the hybrid-super-hyperlens. Adapted with permission from [231]. Copyright 2013 Optical Society of America.

imaginary part is associated with the absorption of light, we will focus on their applications in electromagnetic absorbers.

Without loss of generality, the reflection and transmission coefficients of light normally incident upon a dielectric slab in air can be calculated using the transfer matrix or the Fresnel–Airy formulae [188]. As early as 1934, it was discovered that a thin film of metal with proper thickness can absorb up to 50% of the incident light [240]. Meanwhile, the transmission and reflection intensities are equal to 25%. Inspired by the anti-lasing concept [187], it was recently demonstrated that the interference of two oppositely propagating coherent beams in a heavily doped silicon film could lead to broadband perfect absorption with absorbance larger than 99.99% [188], which is called a thin-film coherent perfect absorber (CPA). On the basis of transfer matrix theory, the perfect absorption condition for the thin-film CPA is obtained as

$$\exp(ink_0 d) = \pm\frac{n-1}{n+1}. \tag{13}$$

For $d \ll \lambda$ and $|nk_0 d| \ll 1$, Eq. (13) is reduced to

$$n' \approx n'' \approx \frac{1}{\sqrt{k_0 d}} = \sqrt{\frac{c}{\omega d}}, \tag{14}$$

where n' and n'' are the real and imaginary parts of the refractive index, k_0 is the vacuum wavevector, ω is the angular frequency, and c is the velocity of light. Since the required complex refractive index is frequency dependent, material with specific dispersion characteristics should be used to obtain a broadband CPA. Fortunately, it has been shown that metal and metal-like material such as doped semiconductors are natural candidates for such applications. Figure 35 illustrates the absorption curves of doped silicon film for two characteristic thicknesses, named the Woltersdorff thickness (150 nm) and the plasmon thickness (450 nm). While the first thickness corresponds to broadband absorption in the low frequency, the second is associated with plasmon resonance. The concept of thin-film CPA was experimentally demonstrated in the microwave range with both a resistive sheet and a graphene layer [241,242]. As realized more recently, a thin layer of resistive sheet was used as a near-perfect absorber in the radio frequency [243], where the thickness-wavelength ratio is as small as 8×10^{-5}, implying that the broadband CPA may bypass the Planck–Rozanov limit [244,245].

Figure 35

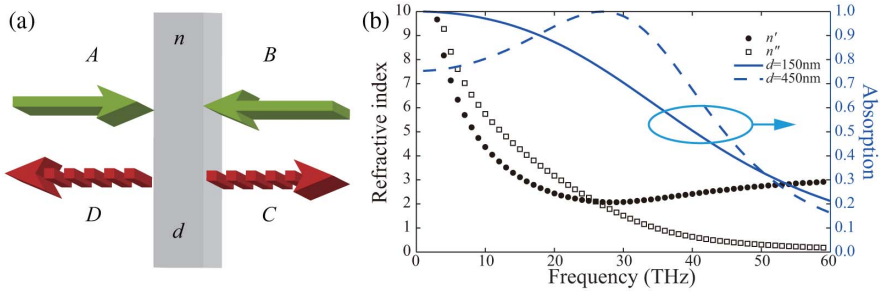

(a) Schematic of the thin-film CPA. (b) Refractive index and absorption spectrum for boron-doped silicon film with a doping concentration of 4×10^{19} cm^{-3}. Adapted with permission from [188]. Copyright 2012 Optical Society of America.

For a thin film with simultaneous electric and magnetic responses, the general CPA condition is [246]

$$\exp(ink_0 d) = \pm\frac{1-Z}{1+Z}, \tag{15}$$

where Z is the effective impedance, and $\pm$ signs are corresponding to the symmetrical and anti-symmetric inputs, respectively. Such a mechanism can be realized by utilizing coherent plasmon hybridization in a metamaterial film composed of MIM structure. CPA can also be employed in a solar thermophotovoltaic system to realize frequency-selective broadband absorption [247], or be extended into other areas such as all-optical logical operations [248], coherent polarization conversion [189,190], coherent abnormal deflection and spin Hall effect [191], subwavelength focusing [249], and lasing and anti-lasing in a single cavity [250].

In thin-film CPA, the absorption enhancement is provided by an additional incident beam with opposite phase; thus the destructive interference condition may be achieved with a film thickness several magnitudes smaller than the wavelength. Such interference could also be constructed by the reflection of a reflective substrate. Nevertheless, since there is a half wave loss in the reflection, the thickness of traditional absorbers is close to one quarter of the wavelength. In order to reduce the thickness of the absorber, higher refractive index material with large loss constant was investigated. Interestingly, an unexpected absorption peak was found for a high-index material with thickness much smaller than $\lambda/4n$. Figure 36 shows the reflectivity and absorption of an absorber composed of a very thin layer of germanium (Ge) deposited on gold (Au) substrate [251]. The minimal thickness of Ge is only 7 nm, close to $\lambda/50$ at a wavelength of 500 nm. Theoretical analysis shows that the reflection phase shift at the a–Ge interface and Ge–Au interface plays an important role for phase matching. Based on this principle, various functional devices such as tunable color filters and thermal emitters were developed [252–255].

Recent results reveal that absorbers based on high-index dielectric spacers have intrinsic angle-independent absorption [256]. According to Eq. (11), the destructive interference condition for a typical Dallenbach absorber with a refractive index of n and thickness of d is written as

$$nk_0 d\sqrt{1-\sin^2\theta/n^2} = \pi/2. \tag{16}$$

Figure 36

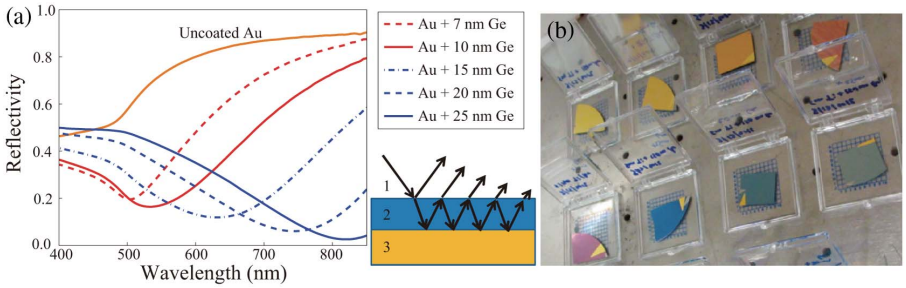

(a) Near-normal incidence reflection spectra of thick Au coated with Ge. (b) Colors formed by coating Au with nanometer films ranging from 0 to 25 nm. Adapted with permission from Macmillan Publishers Ltd.: Kats *et al.*, Nat. Mater. **12**, 20–24 (2013) [251]. Copyright 2012.

When $n \gg 1$, this condition is reduced to $nk_0d = \pi/2$, which is independent of the incident angle. Note that this effective high-index material can be realized using metamaterial [53,257,258]. Figure 37 shows a drawing of the absorbance of a hypothetic Dallenbach absorber ($d = 1$ mm) as a function of the frequency and incident angle.

High index contrast in optical multilayer is a necessary condition for engineering the photonic bandgap and realizing independent control of light in different frequency bands. For instance, Raman *et al.* introduced an integrated photonic solar reflector and thermal emitter consisting of seven layers of HfO_2 ($n = 2$ at $\lambda = 500$ nm) and SiO_2 that reflected 97% of incident sunlight while emitting strongly and selectively in the infrared atmospheric transparency window (Fig. 38) [259]. When exposed to direct sunlight exceeding 850 W per square meter on a rooftop, the

Figure 37

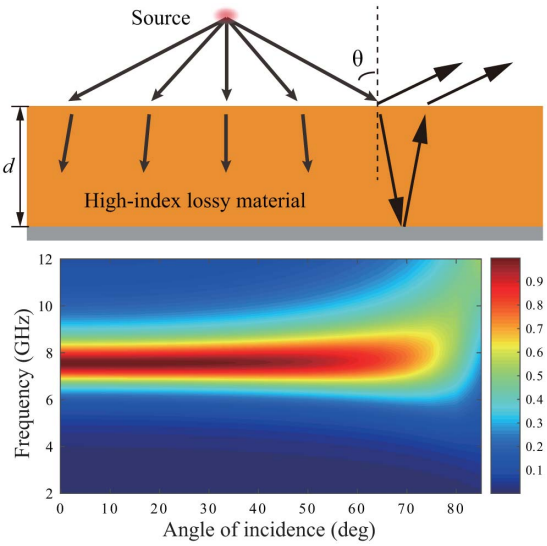

Principle of the wide-angle absorbers based on multiple interference. The bottom shows the simulated results for a Dallenbach absorber. The complex permittivity is chosen as $100 + 12i$.

Figure 38

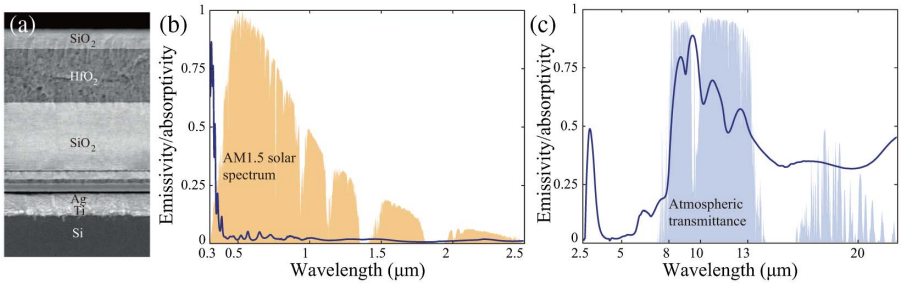

(a) SEM image of the cross section. (b), (c) Measured emissivity/absorptivity at 5° angle of incidence of the photonic radiative cooler over optical and near- and mid-infrared wavelengths using an unpolarized light source. Adapted with permission from Macmillan Publishers Ltd.: Raman *et al.*, Nature **515**, 540–544 (2014) [259]. Copyright 2014.

photonic radiative cooler cooled to 4.9°C below ambient air temperature. Modifications of the design have also been realized using optical transparent conductors and other novel materials [260,261]. Compared with other subwavelength structures, the multilayers are easier to fabricate and use in practical conditions.

5. PERIODIC SURFACE STRUCTURES

Different from photonic crystals whose characteristic dimensions are comparable to the wavelength, periodic structures with subwavelength periodicity are often described by 2D or 3D effective materials termed metamaterials [6]. Such effective materials have dramatically changed the interference phenomena in spectral filtering, absorption, and polarization conversion.

5.1. Spectral Filtering

In traditional optical technologies, color filters are typically made of multilayered thin films [193]. Using subwavelength interference effects, the size of traditional filters may be reduced significantly. In general, subwavelength color filters include both transmissive and reflective types. Figure 39 shows one transmissive filter based on stacked metallic gratings [262]. Owing to the subwavelength interference in the middle dielectric layer, wavelength-selective transmission was realized by tuning the width of the metallic grating. As illustrated in Fig. 39(c), the filtered wavelength is directly related to the stack period owing to the linear dispersion of the anti-symmetric SPP mode, making the design of such filters much easier than like devices. Besides the small dimensions, the polarization dependence of such plasmonic resonators not only benefits the applications in LCD by eliminating the need for a separate polarizer layer, but also can be used for extracting polarimetric information in spectral

Figure 39

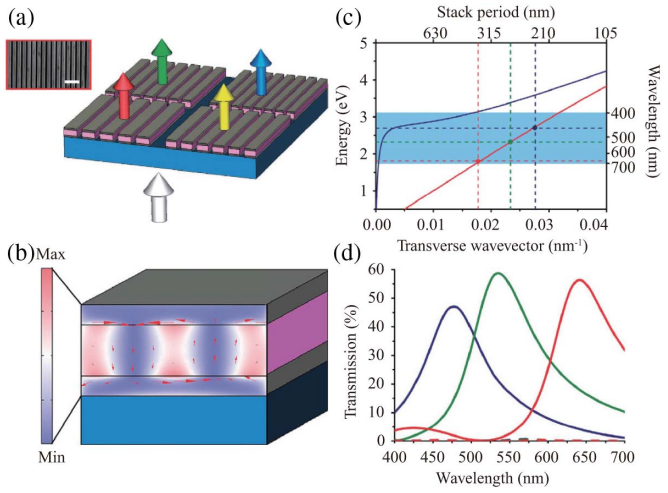

Plasmonic nanoresonators formed by stacked gratings. (a) Schematic diagram of the proposed plasmonic nanoresonators. (b) Cross section of the time-averaged magnetic field intensity and electric displacement distribution (red arrow) at a wavelength of 650 nm. (c) Plasmon dispersions in the stack array. Red, green, and blue dots correspond to the case of filtering primary RGB colors. Red and blue curves correspond to anti-symmetric and symmetric modes. (d) Simulated transmission spectra. The solid and dashed curves correspond to TM and TE illuminations, respectively. Adapted with permission from Macmillan Publishers Ltd.: Xu *et al.*, Nat. Commun. **1**, 59 (2010) [262]. Copyright 2010.

imaging. In another work, the guided mode resonance was adopted in order to realize sharper transmission spectra [134]. However, since guided mode resonance requires a large number of horizontal periods to sustain the propagating modes, it is difficult to shrink the size of pixels.

In some cases, such as displays, reflective color filters are more useful than their transmissive counterparts. This application relates to the wavelength-dependent optical absorbers, which will be discussed in detail in the next section. Here we note that one goal of the spectral engineering is to filter color in a space close to the diffraction limit, since industrial printing techniques could only print at resolutions below 10,000 dpi as a result of their micrometer-sized ink spots. To obtain such a goal, the horizontal coupling of resonators must be decreased; thus interference between vertical multiple reflected waves dominates the physical process [263].

Almost all recent designs of colors filters are based on the direct transmission or reflection of a light wave. These configurations are presented as periodically arranged nanopatches or nanorods atop the substrate. When the distance between adjacent elements is close enough, the coupling between neighboring metallic elements results in a significantly enhanced electric field. Therefore, a dense arrangement of elements appears to be a necessary requirement to design color filters by introducing strong near-field coupling. To avoid the use of costly and inefficient fabricating methods such as electron beam lithography (EBL) and focused ion beam (FIB) milling, interference lithography was recently adopted to achieve an ultra-smooth silver shallow grating with spectral filtering capability. Different from previous designs, the plasmonic shallow grating produces colors by photon spin restoration, which reflects a circularly polarized light to its co-polarized state at specific wavelengths [264]. A FWHM of ∼16 nm with high efficiency (∼75%) has been theoretically obtained and experimentally demonstrated. Furthermore, by rotating the grating and resorting to the geometric phase, simultaneous structural colors and holographic imaging could be realized.

5.2. Broadband Absorption

In Subsection 4.3, it has been shown that a highly lossy film can induce intense electromagnetic absorption. However, since the refractive index of naturally occurring materials is limited by their atomic and molecular structures, the absorption is typically narrowband and not so high. Along with the development of metamaterials and metasurfaces, subwavelength structured absorbing materials are demonstrated to have superb absorption capability beyond the traditional ones [8,11,265]. This subsection focuses on how to use the subwavelength interference effect to increase the absorption bandwidth and efficiency, while simultaneously decreasing the thickness.

Research on perfect absorption of light by subwavelength structures can date back to 1902 with grating diffraction [135]. When light incidents on a metallic grating with subwavelength pitch and thickness, the reflection intensity may be reduced to zero at some particular conditions, and this effect is referred to as Wood's anomaly, which contributes to the discovery of surface plasmons [137]. Inspired by the critical coupling principle shown in Subsection 3.2, surface plasmons in the MIM waveguide were recently utilized to design a perfect optical absorber [136]. With the coupling of two resonant modes, two absorption peaks were realized with a simple structure. Compared with the traditional grating, this new type of flat absorber is much thinner, more robust, and easier to design and fabricate. As another early attempt to reduce the absorber's thickness using subwavelength structures, Engheta theoretically proposed a thin absorbing screen consisting of a resistive sheet and a metamaterial surface with effective high impedance [50]. Since the reflection phase of the high-impedance

surface is 180°, the distance between the resistive sheet and the impedance surface may be reduced to zero; thus the overall thickness of the absorber is equal to that of the impedance surface. It was later shown that thin mushroom-like structures could be used as radar-absorbing structures whose performance nearly does not change with the incidence angle for TM-polarized waves [266]. Based on simultaneous magnetic and electric resonances, a "perfect metamaterial absorber" was subsequently proposed with thickness of only $\lambda/40$ but absorption peaks high up to 96% [267]. With the advantage of intrinsic impedance match to air, this approach opens a new avenue to realizing electromagnetic absorbers for various applications.

The bandwidth of thin metamaterial is typically limited by the thickness, which can be deduced from either the antenna theory or complex analysis [245]. Although not favored by applications such as stealth and solar cell absorbers, this narrow bandwidth enables such absorbers to be used as natural candidates of reflective color filters. As depicted in Fig. 40, each color pixel consists of four nanodisks that support particle resonances [263]. These disks are raised above equally sized holes on a back-reflector, which functions as a mirror to increase the scattering intensity of the disks. The geometric parameters are used to control the interference condition and color generation (right panel). A key feature of such structures is their ease of fabrication and throughput scale-up by means of nanoimprint lithography (NIL) or plasmonic lithography [91,268].

Multiplexed optical recording also requires wavelength-dependent absorption. By exploiting the unique properties of longitudinal surface plasmon resonance of quasi-periodic gold nanorods, Zijlstra *et al.* demonstrated true five-dimensional optical recording for the first time [269]. The longitudinal SPR exhibits excellent wavelength and polarization sensitivity, whereas the distinct energy threshold required for the photothermal recording mechanism provides the spatial selectivity.

In order to increase the absorption bandwidth required for energy harvest or other applications, two approaches have been extensively employed. On the one hand, unit cells with different resonant frequencies can be incorporated into a supercell, as demonstrated by using plasmon hybridization [270] and magnetic resonance coupling [100,102]. On the other hand, multilayered magnetic resonances may be connected to increase the bandwidth [271,272]. Compared with a traditional pyramidal absorber,

Figure 40

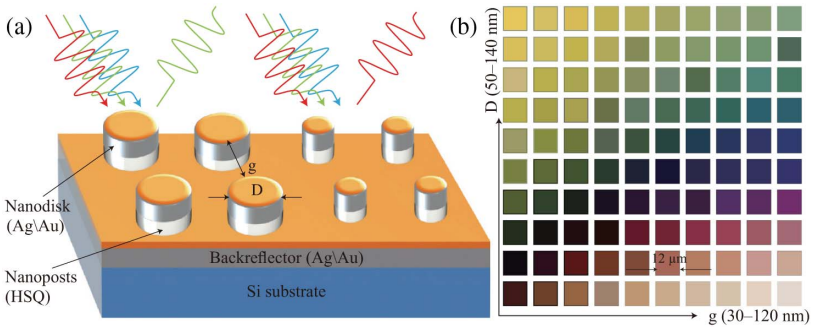

(a) Schematic of the interaction of white light with two closely spaced pixels, each consisting of four nanodisks. As a result of the different diameters (D) and separations (g) of the nanodisks within each pixel, different wavelengths of light are preferentially reflected back. (b) Optical micrographs of arrays of nanostructures with varying diameters D and gaps *g*. Adapted with permission from Macmillan Publishers Ltd.: Kumar *et al.*, Nat. Nanotechnol. **7**, 557–561 (2012) [263]. Copyright 2012.

the broadband absorber composed of metal–dielectric multilayered truncated pyramids exhibits much smaller thickness and better frequency selectivity [273], which ensures its superior performance in thermophotovoltaic applications. By combining the concepts of supercell and multilayers, further increase of the bandwidth was also demonstrated. Figure 41 shows the schematic and results for the hybrid absorber [274]. Owing to the two distinct mechanisms for bandwidth enhancement, a strong absorption larger than 0.9 was demonstrated in a wide frequency range of more than 11 GHz.

In the original metamaterial absorber proposed in Ref. [267], the physical principle was interpreted as the simultaneous control of electric and magnetic responses such that the impedance is matched to free space. However, it is currently widely accepted that such impedance match does not ensure the transmission and reflection to be simultaneously reduced to zero. It is also ambiguous to define the μ_{eff} and ε_{eff} in such complex structures, since the metamaterial perfect absorber cannot be strictly considered as a homogeneous bulk medium [275]. As a consequence, an alternative theory for absorption in such structured materials should be formulated. In contrary to the metamaterial concept, it was shown that the effective impedance was more physically meaningful and beneficial in describing the electromagnetic properties of layered subwavelength absorbers [53]. In general, such layered absorbers can be viewed as a variation of the Gires–Tournois etalon, where the impedance surface acts as a phase screen to realize destructive interference based on the generalized Fresnel's equations [38].

According to the requirements of Maxwell's boundary conditions, the relationship between equivalent impedance and the reflection coefficient of the absorber is derived by exploiting the transfer matrix method [53]:

$$Y_{\text{eff}} = 1/Z_{\text{eff}} = Y_0 \frac{1-r}{1+r} - Y_1 \frac{\exp(-ink_0 d) - r_m \exp(ink_0 d)}{\exp(-ink_0 d) + r_m \exp(ink_0 d)}, \tag{17}$$

where Y_0 and $Y_1 = nY_0$ are the intrinsic admittance of vacuum and dielectric spacer, n is the refractive index of the dielectric spacer, r is the overall reflection coefficient, and r_m is the reflection coefficient of the thick metal layer. By setting the reflection coefficient to zero and mimicking the impedance of the perfect impedance matched layer through frequency dispersion engineering of the metasurface, a broadband

Figure 41

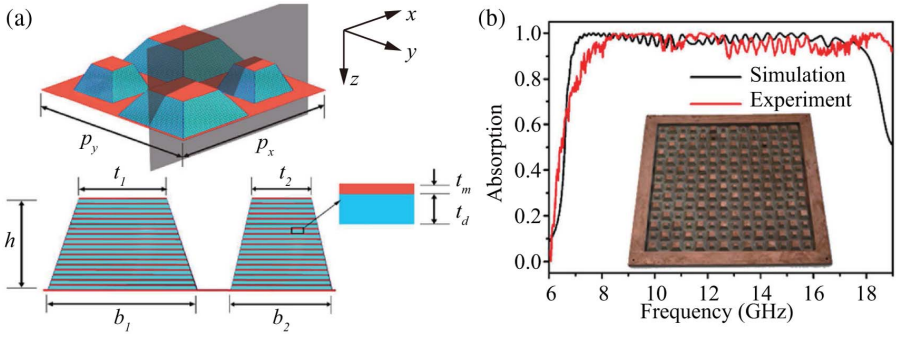

(a) 3D structure diagram (top) and a typical cross section along the xz plane (bottom) for the unit of the metamaterial absorber labeled with sizes. The overall thickness h is 4.36 mm. (b) Simulated and experimental absorption spectra. The inset displays a photograph of the fabricated sample. Adapted with permission from Macmillan Publishers Ltd.: Long *et al.*, Sci. Rep. **6**, 21431 (2016) [274].

infrared absorber was proposed [55]. With a thin layer of structured nichrome, a polarization-independent absorber with absorption larger than 97% was numerically demonstrated over a working band larger than one octave bandwidth (Fig. 42). Since nichrome is a good refractory material, such a configuration ensures that the device can operate at a very high temperature as high as 1000°C for both microwave and infrared applications [38].

The bandwidth enhancement of the above dispersion-engineered absorber is related to the transformation of the Drude model of free electron gas in the metal film to the Lorentz oscillator model of a bound electron in the structured metasurface. The comparison of ideal and retrieved sheet impedance [Fig. 42(b)] implies that the dispersion is actually a series of lumped circuits composed of a resistor, inductor, and capacitor. The capacitance at the lower frequency induces a positive phase shift, while the inductance at the higher frequency introduces a negative phase shift. This frequency-dependent phase shift makes the destructive interference occur in a continuous band and leads to broadband absorption. Intuitively, even larger bandwidth is possible by stacking multilayers and optimizing their dispersion curves. Similar structures have also been proposed to realize broadband absorption in the entire electromagnetic spectrum [54,276].

From a more fundamental perspective, it is a known fact that the maximal absorption bandwidth is limited by the optical thickness as indicated by the thickness-bandwidth ratio [245]. For absorbers working at terahertz and higher frequencies, the physical thickness is very small even for quite large optical thickness. Consequently, the thickness may not cause a big problem for broadband absorption at these frequencies. In contrary, the fabrication technique becomes a challenge since most broadband

Figure 42

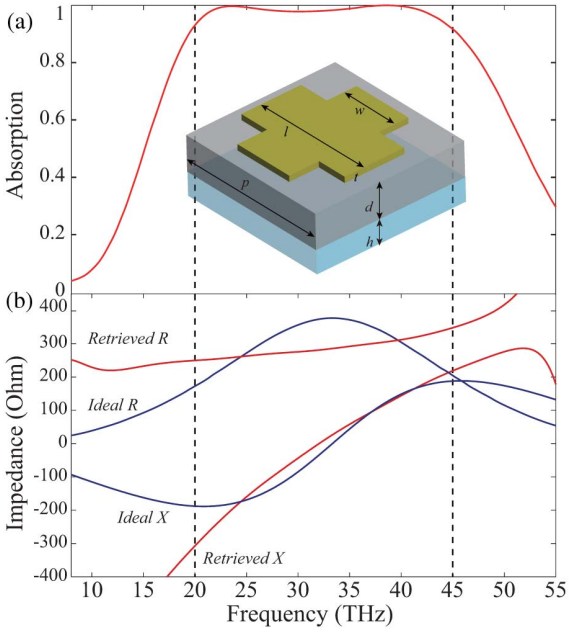

(a) Broadband absorption performance of infrared metasurface absorber. (b) Comparison of the retrieved impedance with the ideal impedance required for perfect absorption. Adapted with permission from [55]. Copyright 2012 Optical Society of America.

absorbers require multilayer thin films or complicated structures. Based on heavily doped silicon structures, Pu *et al.* proposed one easy-to-fabricate and scalable broadband terahertz absorber, as shown in Fig. 43 [132]. Different from common subwavelength absorbers, higher diffraction orders exist because the period is larger than the effective wavelength in the substrate (still smaller than that in vacuum to avoid diffraction in reflection). Through exciting both the zero- and first-order diffraction in the doped silicon wafer and meeting the destructive interference condition for anti-reflection, a relative absorption bandwidth larger than 100% was achieved. Owing to the scalability of Maxwell's equations and the permittivity of doped silicon, the hybrid absorber can be easily extended to higher frequencies, as demonstrated by subsequent experiments [277–279].

5.3. Polarization Manipulations

5.3a. Meta-Anisotropy

As one important aspect of electromagnetic waves, the polarization state has widespread applications ranging from glare elimination to polarization imaging. In the simplest case, polarization could be manipulated by waveplates composed of homogenous but anisotropic material [83,85,86,280]. Furthermore, space-variant anisotropic metasurfaces could generate strong geometric phase; thus the design of high-performance anisotropic polarizers is not only useful for polarization manipulation, but also beneficial for phase-gradient devices [84,281].

One early anisotropic waveplate made of subwavelength structures is the multilayer meander-lines [177], which possess inductive and capacitive impedances along two orthogonal directions (Fig. 44). When the electric field is polarized perpendicularly to the lines, the structure acts as a capacitor and introduces a positive phase retardation. For the other polarization, the surface acts as an inductor and a negative phase shift is induced. The transmittance for both the polarizations is guaranteed by the destructive interference in reflection, as analyzed by Chu and Lee using a transfer matrix method [282]. Owing to the large abrupt phase shift provided by the meander-lines, the overall thickness of the QWP is only ~2.5 mm ($\sim\lambda/12$). Although meander-lines are periodic in each single layer, a unique unit cell cannot be defined since the periodicities of adjacent layers are not the same. This indicates that the common design procedure of multilayered subwavelength structures, like the unit cell boundary condition in commercial software CST MWS, may be not applicable.

Figure 43

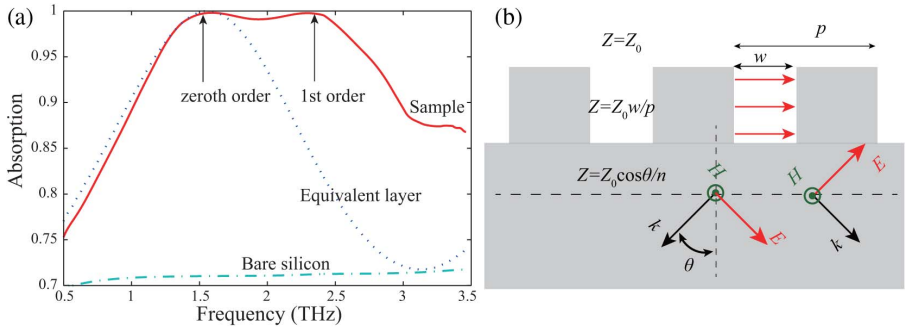

Broadband absorption induced by high-order impedance match. (a) Absorption curves for the designed absorber as well as a bare doped silicon slab and an absorber based on an equivalent anti-reflection layer. (b) Schematic of the impedance matching for the first-order diffraction. Adapted with permission from [132]. Copyright 2012 Optical Society of America.

In contrast to transmissive polarization transformers [177,283], the polarizing metamirrors, which convert the polarization state in reflection mode, have much smaller thickness due to the folded geometry as well as higher energy efficiency since no complicated anti-reflection technique is needed [83,178]. Similar to previous thin metamaterials, ultrathin anisotropic waveplates may be achieved using anisotropic magnetic resonance, which was demonstrated in both the microwave and optical regimes [284,285]. When electric fields are polarized along the inductive axis, the structure acts as a magnetic conductor and the reflective phase shift at resonance is near 0°. For the orthogonal polarization, the phase shift can be either 90° or 180°; thus a quarter or half waveplate may be realized.

Owing to the intrinsic resonance, magnetic metamirrors often operate in a narrow frequency band. In order to overcome this problem, dispersion-engineered ultrathin metamirrors were proposed. For a three-layer configuration composed of a metasurface, a dielectric spacer, and a ground plane, the reflected phase shift may be calculated directly from the well-established transfer matrix method [83]. Once the ideal sheet impedance for arbitrary phase retardation $\Delta\Phi = \Phi_x - \Phi_y$ is calculated, it can be approximated by precisely adjusting the LC resonance of the anisotropic metallic elements.

As demonstrated with an I-shaped resonator array [Fig. 45(a)], near-perfect polarization conversion of circular polarization was realized in the frequency range between 5.5 and 16.5 GHz [83]. Based on a similar configuration, a terahertz polarization converter was experimentally demonstrated [86]. The device is able to rotate the linear polarization by 90°, with a conversion efficiency exceeding 50% from 0.52 to 1.82 THz, and the highest efficiency is about 80% at 1.04 THz. In the near-infrared and visible band, broadband metasurface polarizers have also been demonstrated with high-efficiency, angle-insensitive performance. Meanwhile, the fabrication of a large-area (2 cm × 2 cm) polarization converter was demonstrated by virtue of orthogonal interference lithography [87], which breaks the bottleneck of large-area metasurface fabrication in the optical regime. In order to avoid strong ohmic loss,

Figure 44

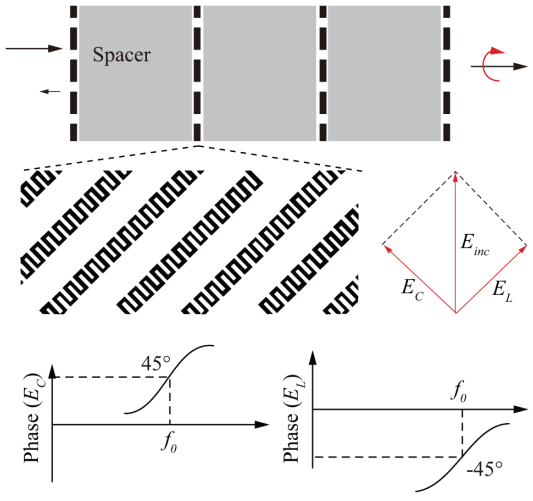

Multilayered meander-line polarizer. Top: schematic of the multilayer. Middle: front view of the meander-line along with the incidence electric fields. Bottom: phase shifts in the two orthogonal directions. © 1973 IEEE. Adapted, with permission, from Young *et al.*, IEEE Trans. Antennas Propag. **21**, 376–378 (1973) [177].

metallic resonators may be replaced by high-index silicon cut-wires [286], following some early work on the form-birefringence [287].

The above dispersion-engineering technique is implemented only along one dimension, which results in an operation bandwidth typically no more than a two-octave bandwidth. Figure 45(b) demonstrates a broadband polarization manipulator with super-octave bandwidth [85]. Multiple resonances accompanied by the superimpositions of Lorentz dispersions were employed to match the effective impedance to the ideal impedance. Experimental results show that this metamirror worked well from 3.2 to 16.4 GHz with polarization conversion efficiency higher than 85%. This converter was also superior to the aforementioned devices in the frequency-band selectivity because the operation band approximates an ideal rectangle. The rectangular coefficient, defined as the bandwidth ratio between high (>80%) and low (<20%) conversion efficiency, is larger than 0.94. This performance is also much better than other designs based on 2D dispersion engineering of L-shaped and cross-shaped antennas [288,289].

As predicted in the discussion of metamirror polarizers [83] and demonstrated later [290], one advantage of such devices over traditional components is that they can be designed to be tunable by replacing some components with semiconductors. The optical and electrical performance of semiconductors such as silicon is dynamically tunable via electric bias or photoinduced carrier generation [291].

5.3b. Meta-Chirality

Besides anisotropy, the chirality arising from magneto-electric coupling plays an important role in the manipulation of circularly polarized light with applications ranging from bio-chemical sensing to negative refraction [292–294]. Structured materials with artificial chirality may be classified into two parts: one is a continuous 3D chiral structure, and the other is a multilayered 3D chiral structure. Inspired by the helix antenna and chiral response of some insects, metallic helices have been proposed as broadband chiral structures [295]. By selectively coupling one particular circular polarization into the helix antenna, a large value of circular dichroism may be obtained. According to classical antenna theory, the operation frequency band of circular dichroism is directly related to the number of helix pitches, and an octave band in the infrared range could be achieved using two pitches of the helix structure.

Figure 45

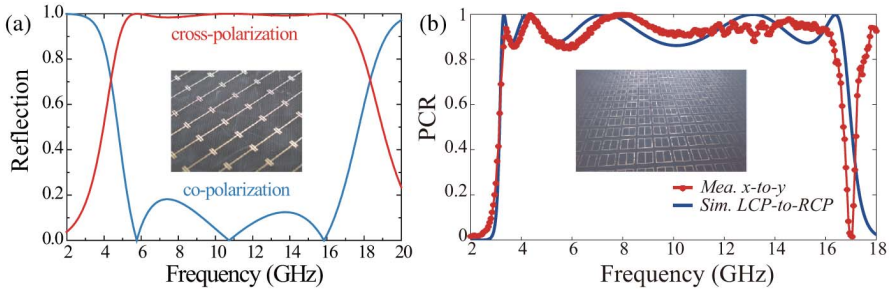

(a) Cross- and co-polarized reflection for a metamirror based on I-shaped resonators. Adapted with permission from Pu *et al.*, Appl. Phys. Lett. **102**, 131906 (2013) [83]. Copyright 2013 AIP Publishing LLC. (b) Metamirror based on split-ring resonators. Adapted with permission from Macmillan Publishers Ltd.: Guo *et al.*, Sci. Rep. **5**, 8434 (2015) [85].

Despite the broadband and efficient response, the metallic helix-shaped chiral metamaterials have 3D structures that require complex fabrication techniques such as two-photon lithography [296]. To reduce the fabrication difficulty, planar chiral structures composed of twisted metallic rods were proposed (Fig. 46), which have broadband chirality in the visible range and are robust to the misalignment in different layers [297]. Once again, multiple interference between these layers is essential in the broadband chiral response, as illustrated using the transfer matrix formalism with a rotation matrix added between each layer.

Ideally, the refractive index of chiral material is dependent only on the handedness of the incident light, but not on the polarization direction of linear polarization. However, as shown in Fig. 46, each layer of this composite material is actually anisotropic. To utilize both the facts in design, multilayered twisted arc structures shown in Fig. 47

Figure 46

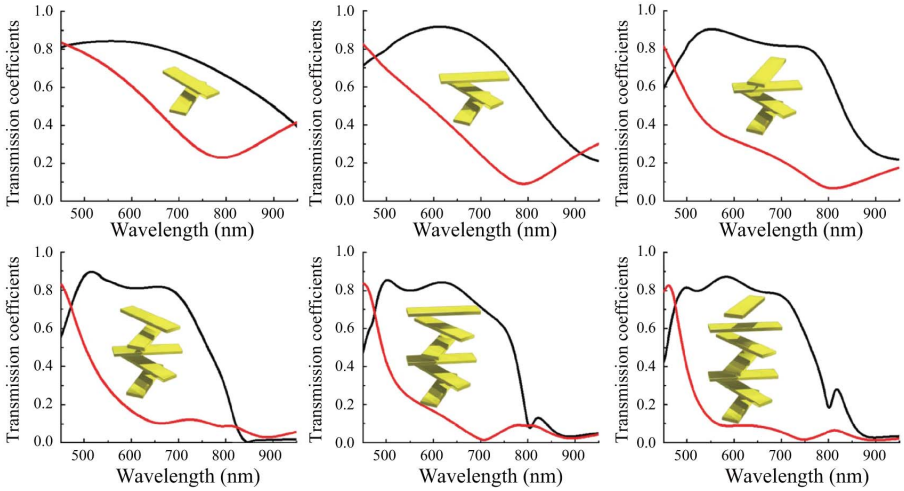

Evolution of the frequency response by increasing the number of stacks. The insets illustrate one unit cell of the corresponding twisted metamaterial. Adapted with permission from Macmillan Publishers Ltd.: Zhao *et al.*, Nat. Commun. **3**, 870 (2012) [297].

Figure 47

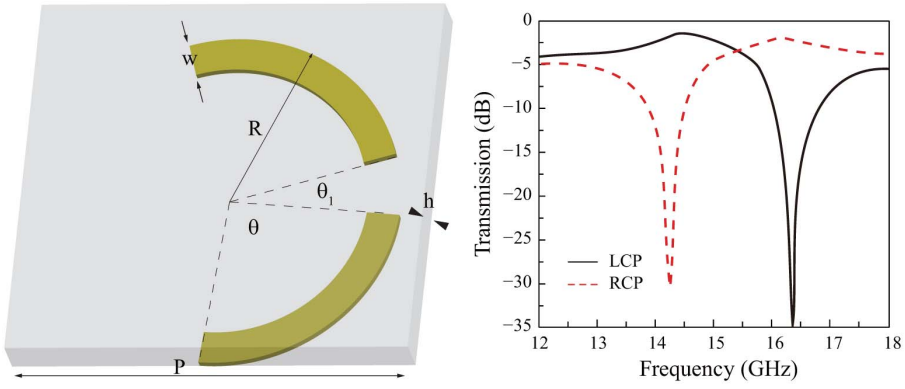

Ultrathin chiral unit cell and corresponding transmission coefficients for RCP and LCP. Adapted with permission from [298]. Copyright 2012 Optical Society of America.

were proposed [298,299]. Similar to the connected helixes with opposite handedness [300], the co-existence of anisotropy and chirality means that there are polarization conversions for circular polarization incidence, although they are often very small. Different from multilayered twisted metallic rods, the arc structures show sharp peaks in the transmission spectra, which are beneficial in the enhancement of chirality. In addition, the arc structures can be further optimized to obtain more resonant frequencies [299]. Owing to the simplicity of fabrication and superior performance, these arc-shaped chiral metamaterials were subsequently widely utilized to construct chiral optical devices for applications such as nonlinear imaging and spectroscopy [301,302].

Besides metallic components, chirality and circular dichroism can also be achieved using dielectric chiral structures such as dielectric spirals and photonic crystals [303,304]. For deep-subwavelength chiral materials that could be homogenized, dielectric chiral materials are more suitable for optical rotation since the difference in the effective refractive index of different circular polarizations is smaller than that of metallic structures [304]. For chiral photonic crystal that cannot be homogenized, the polarization-dependent bandgap results in a larger difference between LCP and RCP, although the bandwidth is often limited [303].

6. APERIODIC SURFACE STRUCTURES

Subwavelength interference in aperiodic structures has been intensively studied in recent decades along with the interest in gradient metamaterials and metasurfaces, which have diverse applications ranging from metalenses to wavefront shaping and holography.

6.1. Metalenses

Lenses and mirrors are the most common components in optical systems, which are governed by some age-old principles associated with reflection and refraction. In general, the laws of reflection and refraction follow the *Principle of Least Time* proposed by Pierre de Fermat in 1662. After the work made by James Clerk Maxwell, it was found that the laws of reflection and refraction could be completely derived using the boundary conditions regarding the electric and magnetic fields. Based on the gradient phase shift on artificially structured surfaces, the generalized Snell's law or the so-called MLRR was proposed [38–40], which provides a promising approach to realize flat metalenses and metamirrors [8,305].

6.1a. Achromatic Metalens

Metalenses are flat lenses composed of gradient subwavelength structures. In the last decade, both metallic and dielectric metalenses have been demonstrated by various research groups [7,127,306]. Since it is easy to realize a metalens for a single wavelength, we focus our attention on the achromatic metalens, which utilizes intricate dispersion-engineering methods to reduce the chromatic dispersion.

Chromatism is a quantity describing the performance change of the optical device when the operating light wavelength changes. It exists not only in traditional flat optical components such as zoneplates and photonsieves [142], but also in many metasurface-based optical devices such as metalenses, deflectors, and holograms [307]. The achromatic focusing requires the focal length to remain as a constant, which implies that the phase shift should vary with the wavelength. According to Fermat's principle, the ideal phase profile for an achromatic lens could be written as [140,307]

$$\Delta\Phi(r,\lambda) = -\frac{2\pi}{\lambda}\left(\sqrt{r^2+f^2}-f\right), \tag{18}$$

where r and f are the radius and focal length, respectively. Since the metalens would behave the same with an arbitrary additive constant, the phase shift may be revised as

$$\Delta\Phi(r,\lambda) = -\frac{2\pi}{\lambda}\left(\sqrt{r^2+f^2}-f\right) + C(\lambda). \tag{19}$$

Since the ideal phase is inversely proportional to the wavelength, it is difficult to achieve using common subwavelength structures. However, with an additional term $C(\lambda)$ added in this equation and introducing strong oscillation in the dispersion curve of each subwavelength structure, more degrees of freedom could be exploited to realize near-achromatic focusing performance.

One straightforward method to optimize $C(\lambda)$ and eliminate the chromatism of the focusing lens is to utilize high-order resonant modes. For instance, a multiwavelength achromatic metasurface was demonstrated based on multiple metallic nano-groove gratings [308]. To achieve achromatic diffraction, the ratio between the resonant wavelength and the period of each elementary grating was fixed. Incident light at those multiple resonance wavelengths can be efficiently diffracted into the same direction with near-complete suppression of the specular reflection. Based on a similar approach, a wide-angle off-axis achromatic flat lens was realized for concentrating light of different wavelengths into the same position.

With an aperiodic arrangement of coupled dielectric resonators, Capasso's group proposed an achromatic metalens working at three different wavelengths of 1300, 1550, and 1800 nm [307,309]. The essence of this lens, however, is achromatic at multiwavelengths rather than in a continuously broad band. Subsequently, a novel method to design a broadband achromatic plasmonic component was proposed based on a metallic nanoslit lens (Fig. 48). By compensating the dispersion of silver material

Figure 48

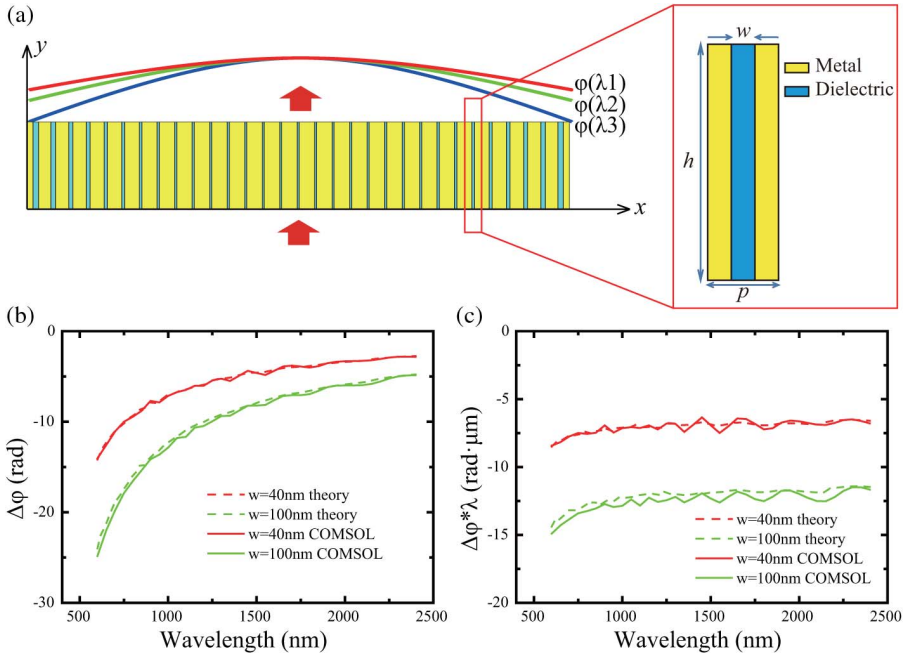

Metallic nanoslits array as an achromatic lens. (a) Side view. (b) Relative phase shifts obtained by theoretical calculations and numerical simulations. (c) Product of φ and λ for each slit width. Adapted with permission from Macmillan Publishers Ltd.: Li *et al.*, Sci. Rep. **6**, 19885 (2016) [140].

and SPP mode in MIM waveguides, achromatic beam deflection and focusing were demonstrated in the wavelength range of 1000–2000 nm [140]. A similar tactic was later demonstrated in an all-dielectric flat focusing lens, which was composed of a subwavelength silicon–air slits waveguide array with varied widths [148]. Such lenses can realize achromatic focusing in a wide spectral range from 8 to 12 μm by engineering the width of the silicon slits.

Compared with the infrared spectrum, an achromatic flat lens operating at the visible range is more appealing. Figure 49 shows an achromatic metalens operating over a continuous bandwidth in the visible from $\lambda = 490$ to 550 nm, accomplished via dispersion engineering of TiO_2 nanopillars tiled on a dielectric spacer layer above a metallic mirror [310]. Following a particle swarm optimization (PSO) process to optimize $C(\lambda)$, a metalens with reverse chromatic dispersion was also designed, where the focal length increases as the wavelength, in contrary to conventional diffractive lenses.

Geometric phase provides another promising way to realize achromatic performance. For instance, an integrated-resonant unit element of combined geometric phase and resonant phase shift was employed to design broadband achromatic flat optical components [311]. An achromatic converging metalens and beam deflector were demonstrated within a broad infrared band from wavelength of 1200 to 1680 nm [311] and a broad visible band from 400 to 660 nm [312]. As a result of the limited phase-shift coverage, the achromatic lens shown in Fig. 50 has a small numerical aperture of

Figure 49

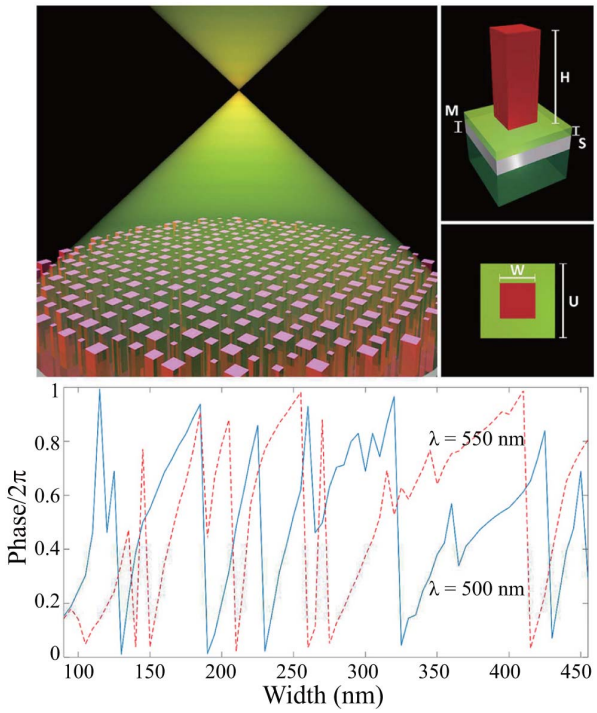

Achromatic metalens in reflection mode. The building block consists of a titanium dioxide (TiO_2) nanopillar with height $H = 600$ nm on a substrate. The bottom shows the reflection phase shift as a function of the nanopillar width at two different wavelengths of 500 and 550 nm. Adapted with permission from Khorasaninejad *et al.*, Nano Lett. **17**, 1819–1824 (2017) [310]. Copyright 2017 American Chemical Society.

0.268. For all the measured wavelengths, the focused light has a strong intensity at $z = 100$ μm.

The above two achromatic lenses are both reflective, and are of less priority for optical systems with middle-sized apertures. To surpass this problem, transmissive devices have been designed based on dielectric resonators [46,313]. As illustrated in Fig. 51, the achromatic metalens is constructed by varying both the sizes and orientation angles of two complementary structures (holes and pillars) [46]. With a diameter of 50 μm and NA of 0.106, the metalens is able to form achromatic images as shown in Figs. 51(c)–51(e). In order to increase the aperture size, while simultaneously maintaining the achromatic performance, larger phase shift and stronger dispersion correcting ability should be provided.

6.1b. Wide-Angle Metalens

Besides serious chromatic dispersion, most planar lenses suffer from off-axis aberration [314] because the ideal phase profile is dependent on the incidence angle [315]. In contrast, the gradient-index Luneburg lens is free from such aberration owing to its rotational symmetry [316]. The gradient-index requirement can be addressed by use of metamaterial-homogenization techniques [317–320]. For example, by etching subwavelength holes into silicon on insulator, a flattened all-dielectric Luneburg lens at telecommunication wavelengths was realized [321], which exhibits beam forming from a planar focal surface over a wide field of view (FOV) of 67°. Meanwhile, a 3D transformation-optics lens was proposed in the microwave frequency band [318], which was fabricated by multilayered dielectric plates with inhomogeneous holes. By shifting a planar array of feeding sources on the flattened focal plane, the radiation beam scanned in a range of 50°. Similarly, a 3D version of the Luneburg lens at optical frequencies has been fabricated by using the ultrafine femtosecond laser direct writing technique [319].

Figure 50

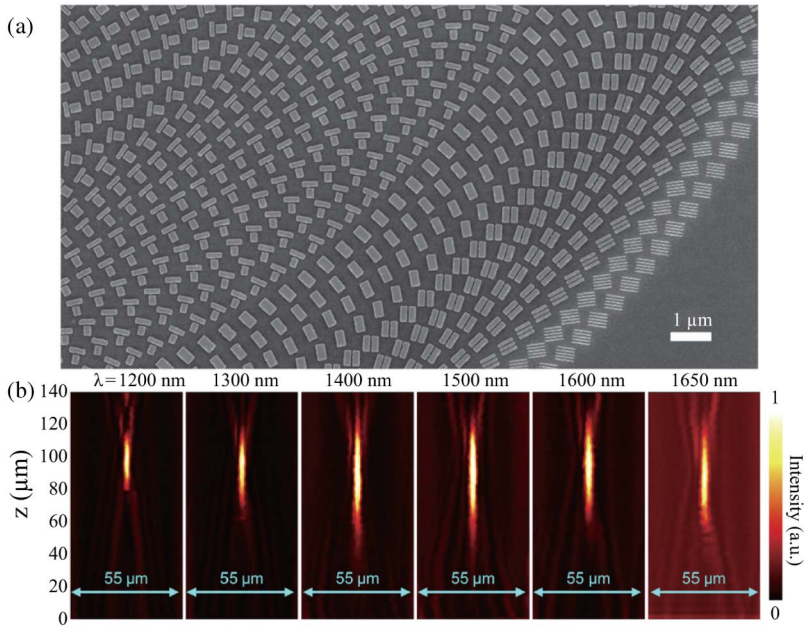

(a) Zoom-in SEM image of fabricated metalens. (b) Experimental intensity profiles along axial planes at various incident wavelengths. Adapted with permission from Macmillan Publishers Ltd.: Wang *et al.*, Nat. Commun. **8**, 187 (2017) [311].

In imaging applications, although the Luneburg lens bears a rather large FOV, the rotational symmetry of these near-optimal lenses makes them not compatible with flat optics as well as the current planar fabrication technologies. Fortunately, recent results show that multilayered or curved metasurfaces could be promising alternatives to traditional Luneburg lenses [314]. As an example, a flat wide-angle lens with a monolithic metasurface doublet could correct the monochromatic aberrations [322]. The doublet lens consists of a hexagonal array of 600-nm-tall amorphous Si nanoposts with spatially varying diameters on the top and bottom surfaces of a 1-mm-thick transparent fused silica substrate, which has a small f-number of 0.9 and a FOV larger than $60^\circ \times 60^\circ$, and operates at 850 nm wavelength with 70% focusing efficiency. Based on the principle of the Chevalier Landscape lens, a similar doublet was demonstrated at a wavelength of 532 nm using the geometric phase in TiO_2 nanofins [323]. By combining the aperture metalens and the focusing metalens, large FOV up to 50° was demonstrated, as shown in Fig. 52. Compared with the multi-microlens objective fabricated by two-photon laser direct writing [324], the metasurface doublet is more compact and easier to scale up.

Since the off-axis aberration of the planar lens is associated with the symmetry breaking of light–matter interaction, it is interesting to see whether the symmetry could be controlled with subwavelength structures. Following this route, a strategy that is able to control such symmetry in a 2D flat lens with rapid phase gradient has been proposed, which enables perfect conversion from rotational symmetry to translational symmetry and results in near-perfect wide-angle lensing performance. The phase of the proposed super-symmetric lens follows a quadratic form. Therefore, the lens is termed a "quadratic lens":

$$\Phi(r) = k_0 \frac{r}{2f}, \tag{20}$$

Figure 51

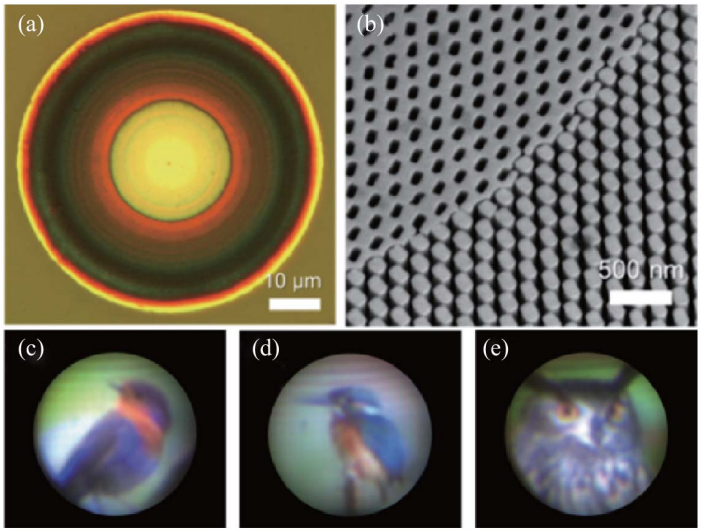

(a) Optical image of broadband achromatic metalens. (b) Zoom-in SEM images at the boundary of nanopillars and Babinet GaN-based structures. (c)–(e) Colorfully captured images from achromatic metalens. Adapted with permission from Macmillan Publishers Ltd.: Wang *et al.*, Nat. Nanotechnol. **13**, 227–232 (2018) [46].

where $r \in [0, 2\pi]$ is the radial distance to the lens center. Interestingly, Eq. (20) is just the phase for a normal thin lens in the paraxial regime. Assuming that the incident collimated light beam lies in the xz plane with an arbitrary angle of θ to the normal axis of the lens, the phase carried by the outgoing light should be

$$\Phi(r) = k_0 \frac{r^2}{2f} + k_0 x \sin\theta = \frac{k_0}{2f}((x + f\sin\theta)^2 + y^2) - \frac{f k_0 \sin^2\theta}{2}, \quad \textbf{(21)}$$

where $k_0 x \sin\theta$ is the gradient phase induced by oblique incidence. Since the last term on the right-hand side does not depend on r, there is only a transversal shift of $f\sin\theta$ in the x direction with respect to normal incidence. Consequently, the rotational shift of oblique incidence is converted to the translational movement of the focusing beam [Fig. 53(a)], which can be used in Fourier transform and wide-angle imaging.

The quadratic lens could be realized using either discrete nanoantennas or semi-continuous catenary structures [Fig. 53(b)] [325]. To increase the energy efficiency of single-layered metasurface, Liu *et al.* proposed a 1D Fourier metalens made of an array of dielectric waveguide resonators [326], which shows focusing efficiency as high as ≈50% for incidence angles of 0°–60° and a broad bandwidth ranging from 1100 to 1700 nm [Fig. 53(c)].

Figure 52

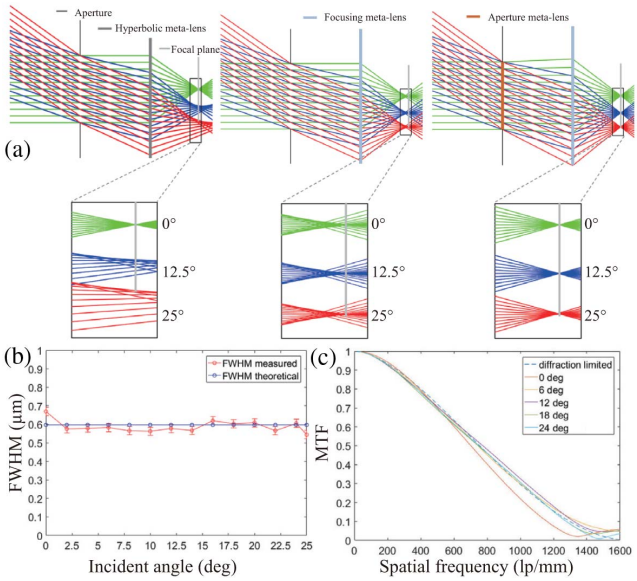

Principle of aberration correction in metasurface doublet. (a) Left: ray diagram of a metalens with hyperbolic phase profile showing large aberrations at oblique incidence. An aperture is added before the focus lens. Middle: ray diagram of the focusing metalens, where a polynomial is added onto the hyperbolic phase profile to correct aberrations. Right: ray diagram obtained by adding the aperture metalens resulting in diffraction-limited focusing along the focal plane. Insets show the magnified plots near their focal planes. (b) Theoretical and measured FWHM along the x direction. (c) Measured modulation transfer function (MTF) curves at different incidence angles. The horizontal axis is in units of line pair per millimeter. A diffraction-limit MTF curve (blue dashed line) is provided as a reference. Adapted with permission from Groever *et al.*, Nano Lett. **17**, 4902–4907 (2017) [323]. Copyright 2017 American Chemical Society.

Analogous to the Luneburg lens, the quadratic flat lens can be easily integrated in lens antennas owing to the translational symmetry. The radiation direction and side lobe are made tunable by adjusting the horizontal position and the distance between the source and the flat lens. As demonstrated recently [327], a high-efficiency (>80% even when the incidence angle is titled by 60°) and ultrathin (0.127λ) metalens was realized by Guo *et al.* using bilayer geometric metasurfaces. Wide-angle beam steering ability beyond ±60° was experimentally demonstrated in 16–19 GHz. Compared with previous beam steering techniques such as the Luneburg lens and rotational prisms, this approach provides great advantages such as low profile, easy implementation, and dramatically reduced side lobe level.

6.2. Structured Light Generation

Flat metalenses and metamirrors are only one specific application of gradient subwavelength structures. With localized phase shift, the wavefront of arbitrary beams could be directly modulated, which enables many novel applications such as holography and OAM generation.

6.2a. Holography and Beyond

CGH is one of the most important applications of aperiodic subwavelength structures. Depending on the modulation methods, CGH can be divided into two categories, one amplitude-type and the other phase-type (also known as Kinoform [328]). Like the Fresnel zoneplate, the diffraction efficiency of amplitude-type CGH is typically very low, and the reconstructed images are accompanied by ghost images. To separate the ghost images from the designed patterns, off-axis and detoured phase holograms are often adopted [329]. A recent paper based on the nanoslit array can illustrate this concept well [330], although the original polarization-independent holography was extended to be polarization-dependent by using the nanoslits as phase elements.

Figure 53

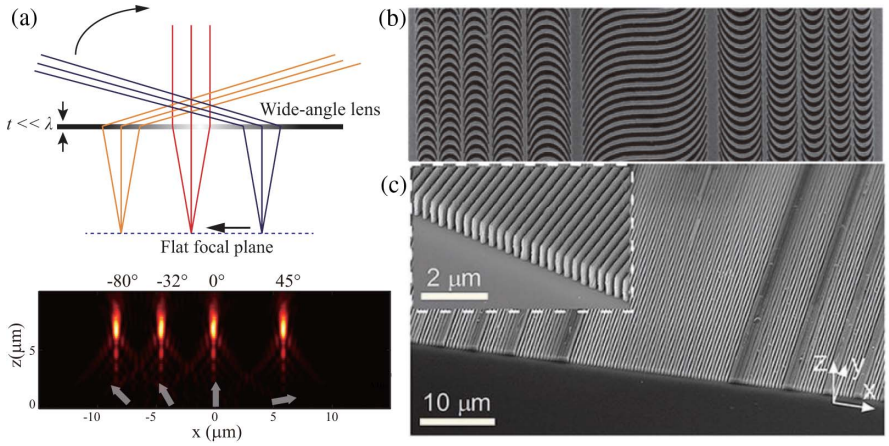

Wide-angle Fourier lens based on symmetry transformation. (a) Schematic of the operational principle. The bottom shows the intensity distribution with different incident angles. Adapted with permission from [325]. Copyright 2017 Optical Society of America. (b) SEM image of the catenary Fourier lens. Adapted with permission from [78] under the terms of the Creative Commons Attribution NonCommercial-NoDerivs 4.0 License. (c) Dielectric Fourier lens based on gradient silicon grating. Liu *et al.*, Adv. Mater. **30**, 1706368 (2018) [326]. Copyright 2018 Wiley-VCH Verlag. Adapted with permission.

As shown in Fig. 54, for a given off-axis direction θ under normal incidence, the optical path difference of light between two slits separated by D could be expressed as D sin θ. As a result, one can control the phase difference by adjusting the distance D. Using this approach, polarization-dependent holography was designed for many different functions such as optical vortex and Airy beam generation. Notably, this experiment can be seen as a 2D extension of Young's double slits interference.

Since the detoured phase has intrinsic low efficiency and is accompanied by twinborn images, many other alternatives have been proposed to realize high-efficiency phase modulation, such as plasmonic and dielectric retardation, and impedance-induced and geometric phase. By replacing metallic slits with high-aspect dielectric pillars, the efficiency could be increased to be about 75% [331]. In principle, all these phase modulation schemes are suitable for both lensing and holography applications, except that the phase distribution for holography is much more random and lacking in symmetry. One other different requirement is on the dispersion characteristic of the phase shift. For lensing and imaging applications, a phase modulation reversely proportional to the wavelength is typically required for broadband applications. However, the phase needs to be independently controlled at separate frequencies to realize multicolor holography. Figure 55 shows the setup of a color hologram under y-polarized white light illumination (consisting of 405, 532, and 658 nm laser beams) that reconstructs images "R" in red, "G" in green, and "B" in blue, respectively [332]. The aluminum nanorod array is patterned on a 30-nm-thick SiO_2 spacer layer sputtered on top of a 130-nm-thick aluminum mirror; thus the phase modulation mechanism is actually the same as the magnetic or gap-plasmon resonators [53,333]. With spatial-variant design of the structures, resonances with narrow bandwidth are realized to allow each color to be controlled separately by the three kinds of nanorods.

To reduce the pixel size as well as the crosstalk between different channels, a high-performance multicolor 3D meta-hologram was realized based on a single type of plasmonic pixel under off-axis illumination (Fig. 56) [43]. Both a full-color flower

Figure 54

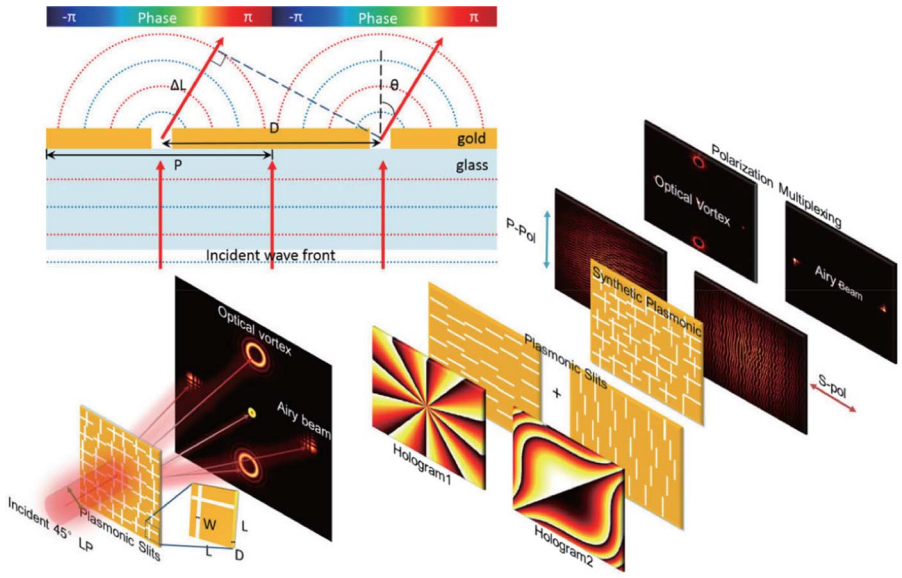

Principle of detour phase (above) and polarization multiplexing of a meta-hologram (bottom) based on nanoslits. Min *et al.*, Laser Photon. Rev. **10**, 978–985 (2016) [330]. Copyright 2016 Wiley-VCH Verlag. Adapted with permission.

image and a 3D spiral helix pattern composed of multiple light spots with varying colors were realized. Owing to the angle-dispersion, the crosstalk between different colors existing in traditional space-division designs was avoided [332,334]. The signal-to-noise ratio (SNR) is five times better than that of the previous meta-hologram design. Switching among different images is achieved by tuning the incident angle of the illumination light.

Besides linear holography, increasing attention has been focused on the nonlinear optical properties of subwavelength materials, particularly in the context of second- and third-harmonic generation. Owing to the greatly increased local fields, the nonlinear

Figure 55

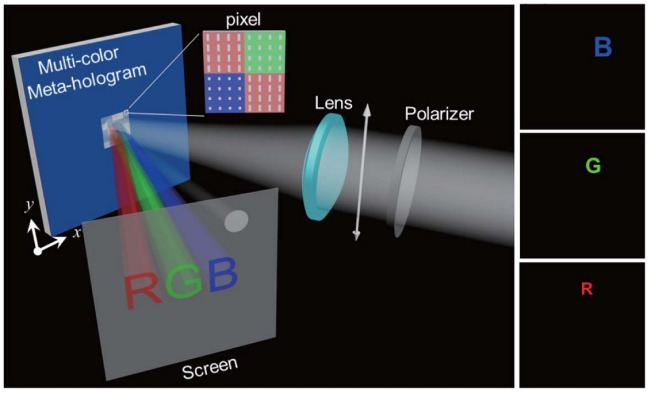

Illustration of the designed multicolor meta-hologram under linearly polarized illumination. The sizes and locations of the three images R, G, and B relative to the zeroth-order spot located at the upper right corner of the image screen are designed to make the reconstructed images fall into the correct spatial order with the appearance of equal size. Adapted with permission from Huang *et al.*, Nano Lett. **15**, 3122–3127 (2015) [332]. Copyright 2015 American Chemical Society.

Figure 56

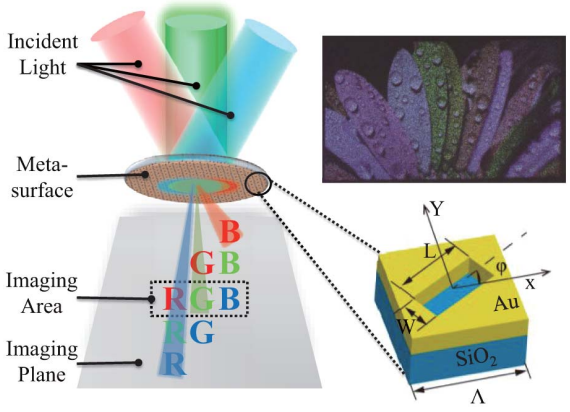

Schematic diagram of the off-axis illumination method for full-color meta-hologram. The image on the top right shows the experimental results of a colorful flower image based on plasmonic nanoslit antennas. Adapted with permission from [43] under the terms of the Creative Commons Attribution NonCommercial License.

effect may be boosted dramatically at the subwavelength scale [62]. However, due to the somewhat limited phase and amplitude control over the nonlinearities of the individual element, the fundamental issue of phase matching across metasurfaces has not yet been thoroughly addressed. Recently, Almeida *et al.* demonstrated full control over the nonlinear phase on the subwavelength scale in phase-gradient metasurfaces [335]. As in the linear regime, phase control over the nonlinear nanoantennas leads to a modified manifestation of the laws governing nonlinear phenomena, such as nonlinear scattering, nonlinear refraction, and frequency conversion. Four wave mixing (FWM) from such metasurfaces revealed a new feature: the scattering from a phase-gradient unit cell enables an anomalous phase-matching condition for FWM from such metasurfaces.

Li *et al.* have experimentally demonstrated nonlinear metasurfaces with homogeneous linear optical properties but spatially varying effective nonlinear polarizability with continuously controllable phase [336]. The continuous phase control over the local nonlinearity has been demonstrated for second- and third-harmonic generation by using nonlinear metasurfaces consisting of nanoantennas of C3 and C4 rotational symmetries, respectively. The continuous phase engineering of the effective nonlinear polarizability enables complete control over the propagation of harmonic generation signals. Therefore, this method seamlessly combines the generation and manipulation of harmonic waves, paving the way for highly compact nonlinear nanophotonic devices. More recently, Ye *et al.* reported a spin and wavelength multiplexed nonlinear metasurface holography [337], which allows the construction of multiple target holographic images carried independently by the fundamental and harmonic generation waves of different spins (Fig. 57). Such nonlinear holograms provide independent and crosstalk-free post-selective channels for holographic multiplexing and multidimensional optical data storage, anti-counterfeiting, and optical encryption.

Figure 57

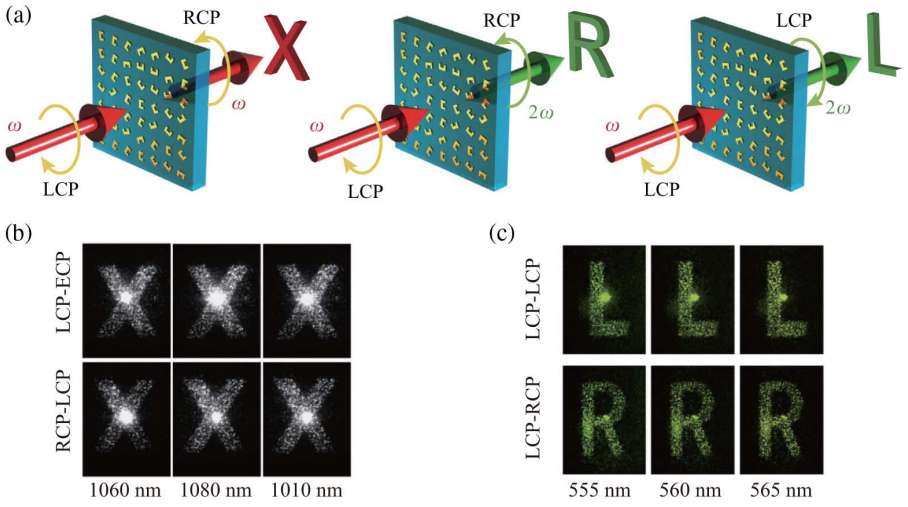

Nonlinear holographic metasurfaces. (a) Linear holography for reconstruction of the letter "*X*" at infrared wavelengths and nonlinear holographic images for the reconstruction of the letters encoded in the different circular polarization states. (b) Linear holographic image at various wavelengths is recorded when incident and measured polarizations are perpendicular. (c) Two-channel holographic images at second-harmonic wavelengths. Adapted with permission from [337] under terms of the Creative Commons Attribution NonCommercial-NoDerivs 4.0 License.

As a quantum mechanical description of photons, the optical angular momentum is crucial for various classical and quantum applications [338]. In 1936, Beth first demonstrated that circularly polarized light possesses spin angular momentum (SAM) of $\pm\hbar$ per photon [339]. In 1992, Allen *et al.* [340] recognized that a helically phased beam with $\Phi = l\varphi$ possesses quantized OAM of $l\hbar$, where l is known as topological charge. Featuring a helix phase front and zero intensity distribution at the beam center, beams carrying OAM are also called optical vortices and have drawn increasing attention from many realms, including super-resolution imaging [341], optical micromanipulation [342], optical communications [343], and detection of rotating objects [344]. Recent progress in the modal basis that carries OAM facilitates space-division multiplexing due to the inherent orthogonality of the different OAM modes [345]. However, traditional technologies to generate and manipulate vortex beams suffer from bulky size and thus cannot be integrated in nanophotonic systems. By utilizing the geometric phase in space-variant anisotropic structures, it is quite straightforward to obtain a lens for vortex beam generation under circular polarization illumination [41]. Plasmonic phase modulation in metallic holes can also be utilized for such applications for both linear polarization and circular polarization. In order to relax the fabrication requirement in the visible band, high refractive index materials were filled into the metallic slits to obtain stronger local phase engineering ability; thus a radius change of approximately 56 nm results in a 2π phase change [93]. According to the geometric phase theory, a vortex plate composed of rotated metallic rods could generate helical geometric phase under circularly polarized illumination. In order to produce a focusing optical vortex, a spherical wavefront along the radial direction and a spiral wavefront along the azimuth direction are both needed [41]. With similar approaches, the twisted focusing optical vortex [346] and deflecting vortex [347] have been demonstrated. Recently, Li *et al.* proposed a physical methodology for multiple OAMs multiplexing and demultiplexing by an off-axis designing principle to integrate all the space-division multiplexing (SDM), wavelength-division multiplexing (WDM), and polarization-division multiplexing (PDM) into one single ultrathin metasurface [348]. With off-axis incidence of beams representing independent information channels, the component can generate independent coaxial vortex beams with different topological charges as a multiplexer. Furthermore, the conservations of momentum make this off-axis diffractive component contain dispersion, which demonstrates its great potential in a SDM-WDM system. To achieve integrated OAM detection, Ren *et al.* proposed an angular momentum multiplexing method using a nano-ring aperture with a chip-scale footprint as small as 4.2 μm × 4.2 μm, where nano-ring slits exhibit a distinctive outcoupling efficiency on tightly confined plasmonic modes [349]. The mode-sorting sensitivity and scalability of this approach enable on-chip parallel multiplexing over a bandwidth of 150 nm in the visible wavelength range. Note that angular-momentum-dependent plasmonic coupling can also be understood in the framework of the spin Hall effect and the angular momentum Hall effect [350–352].

As another interesting beam with structured phase, the Bessel beam represents an exact solution of the Helmholtz equation [353]. An ideal Bessel beam requires the horizontal dimensions as well as the power carried by the beam to be infinite, which cannot be achieved in practical situations. Nevertheless, it was shown that even truncated with a Gaussian function, the Bessel beam can still maintain its unique properties such as being diffraction-free and self-healing, which enable a variety of important applications in super-resolution imaging [354], optical trapping, and nanofabrication [342]. Furthermore, by merging the spherical and conical wavefronts, a "Bessel lens" with much higher imaging resolution than the traditional lens could be produced [355].

High-order Bessel beams (HOBBs), i.e., Bessel beams carrying optical vortices, are a new research frontier of structured light. The hollow-core shape of the HOBBs and its ability to retain over an extended propagation distance in a propagation-invariant manner make it useful in optical manipulation. In principle, the HOBBs could be generated via a similar method to that used for previous phase-type elements. By exploiting quasi-continuous catenary nanostructures that generate continuous phase modulation between 0 and 2π as building blocks (Fig. 58), 2D arbitrary phase modulation was obtained by locating and rotating the elements along a predefined trajectory, which offers a great flexibility for the generation of HOBBs in a broad spectral band [41,174].

In geometric phase theory, the magnitude of phase would reverse when the handedness of incident circular polarization is switched, which means that light beams with opposite spin states will acquire opposite horizontal momenta [78,175,356]. Recently, it was demonstrated that this symmetry of geometric phase may be broken by merging the geometric phase and propagation phase in metasurfaces [45,157,357–359]. Benefiting from the independent phase modulation for opposite spins, totally different holographic images or vortex beams carrying arbitrary OAM have been achieved in the far field for each separate circular polarization, in both the visible and infrared bands.

Based on asymmetric spin-orbit coupling, giant and broadband circular asymmetric transmission (AT) was experimentally realized, accompanied by wavefront manipulation for transmitted and reflected circularly polarized light [44]. The circular AT is defined as the difference in total transmittance of CP light between forward and backward beams. The bottom panel of Fig. 59(a) illustrates the different transmission resulting from constructive and destructive interference under circular polarization incidence from the substrate. To demonstrate the wavefront manipulation capability, an asymmetric deflector, vortex beam generator, and hologram are designed, which show anomalous refraction and reflection that are different from traditional geometric metasurfaces. This approach provides a promising new route to replacing bulky cascading optical

Figure 58

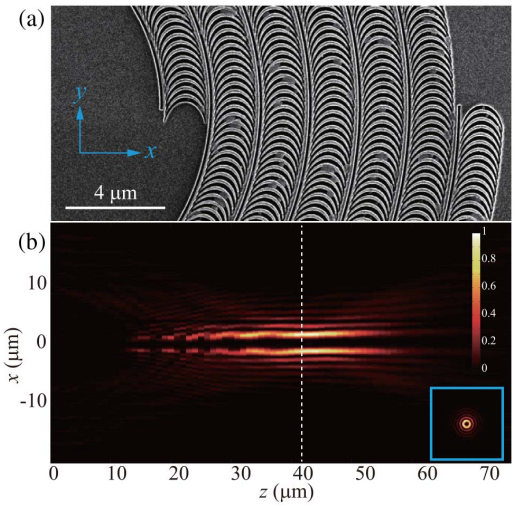

HOBBs generation via catenary metasurface. (a) SEM image of the sample. (b) Intensity distribution in the *xz* plane and the *xy* plane (inset). From Pu *et al.*, Sci. Adv. **1**, e1500396 (2015) [41]. Adapted with permission from AAAS.

components such as beam splitters and prisms with only one ultrathin metasurface for chiroptical spectroscopy, chiral imaging, optical communication, etc.

6.2b. Polarimetry and Spectropolarimetry

In addition to the spatial phase profile, the distribution of polarization is an important factor for structured light. It was shown that properly designed gradient metasurfaces based on geometric phase could efficiently control the polarization states. Figure 60 demonstrates an optically active metasurface of $\lambda/50$ thickness that rotates linearly polarized light by 45° over a broadband wavelength range in the near-infrared region [360]. The rotation of the polarization angle is related to the offset distance between the neighboring supercells, which results in a relative phase shift between the outgoing beams. Therefore, this method allows for greater tolerance against fabrication errors, similar to another metasurface constructed by V-shaped antennas [361].

Figure 59

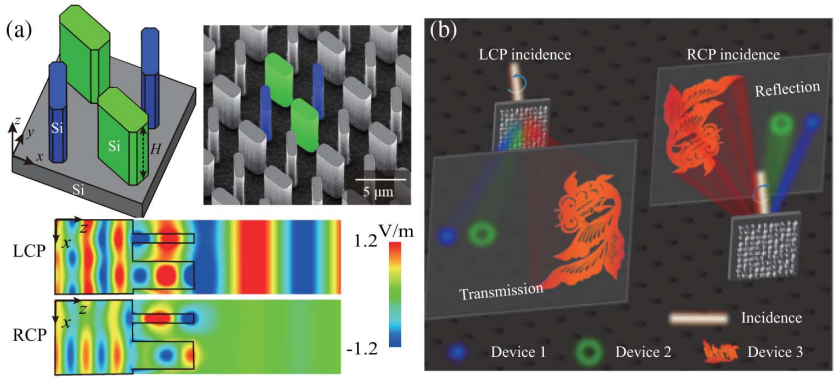

(a) Asymmetric transmission in hybrid unit cells. The electric field distributions correspond to the illumination of LCP and RCP light from the substrate side at the resonant wavelength of 9.9 μm. (b) Schematic illustration of the designed devices that generate diffraction patterns in the transmission (reflection) field under the illumination of LCP (RCP). Zhang *et al.*, Adv. Funct. Mater. **27**, 1704295 (2017) [44]. Copyright 2017 Wiley-VCH Verlag. Adapted with permission.

Figure 60

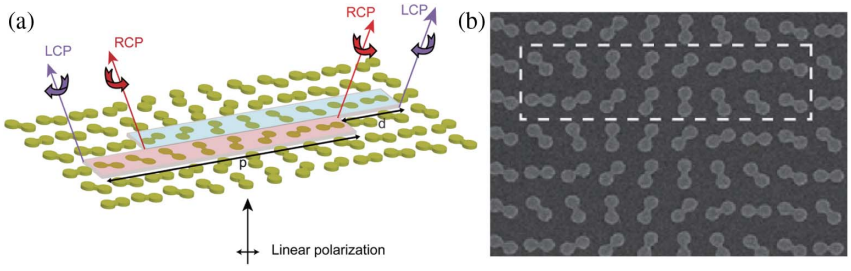

(a) Metasurface structure that performs optical rotation. It includes two subarrays (in blue and red) causing circular polarization splitting in two opposite diffraction directions. In each diffraction direction, LCP and RCP add up to form linear polarization. The two subarrays are separated by an offset distance d, causing a phase shift between the LCP and RCP. (b) SEM image of the fabricated sample. Adapted with permission from Shaltout *et al.*, Nano Lett. **14**, 4426–4431 (2014) [360]. Copyright 2014 American Chemical Society.

Since the polarization rotation angle only depends on the offset distance, multiple different polarization states can be easily obtained in a broadband range, although the efficiency may be limited by the unit cell design. Based on the offset phase modulation and the spatial multiplexing, a reflective metasurface constructed by aluminum plasmonic antennas was recently developed, which can generate six polarization states simultaneously including four linear polarizations and two circular polarizations in the entire visible spectrum, as shown in Fig. 61 [362].

Another important application of the gradient geometric metasurface is polarization measurement, since different polarized light is scattered in different directions [165]. Balthasar Mueller *et al.* proposed a nondestructive polarization measurement method based on a single 2D array of rod antennas, which relies on the detection of polarization-selective directional scattering and can substantially outperform existing polarimeters in terms of size, cost, and complexity [363]. More recently, chip-size plasmonic spectropolarimeters consisting of three gap-plasmon phase-gradient metasurfaces were experimentally demonstrated for simultaneous polarization state and wavelength determination [364]. The spectropolarimeters diffract normally incident light to six predesigned directions, whose polar angles are proportional to the light wavelength, while contrasts in the corresponding diffraction intensities provide a direct measure of the incident polarization state through retrieval of the associated Stokes parameters. The proof-of-concept 96-μm-diameter spectropolarimeter exhibits expected polarization selectivity and high angular dispersion (0.0133°/nm) in the wavelength range of 750–950 nm.

6.2c. Electromagnetic Virtual Shaping

Reflective subwavelength surface structures are useful for radar/lidar cross-section (RCS/LCS) reduction applications by employing the concept of virtual shaping [84,365]. In a general sense, the spherical/cylindrical cloak, carpet cloak, and other functional devices based on transformation optics [366,367] could be seen as one kind of virtual shaping. For example, the spherical, cylindrical, and carpet cloaks are defined to transform a given space to a point, line, and plane; thus the objects hidden in the space are invisible to outer observers. Different from this 3D gradient metamaterials approach, the recent trend of virtual shaping is to exploit the surface properties to realize wavefront shaping via changing the electromagnetic boundary conditions [38,368]. According to the Huygens' principle [128], the manifestation of gradient constitutive materials is equivalent to the gradient boundary approach in many cases.

Since traditional methods based on absorbing materials and/or shaping are often limited by physical constraints such as aero- and hydro-dynamics of vehicles, it is

Figure 61

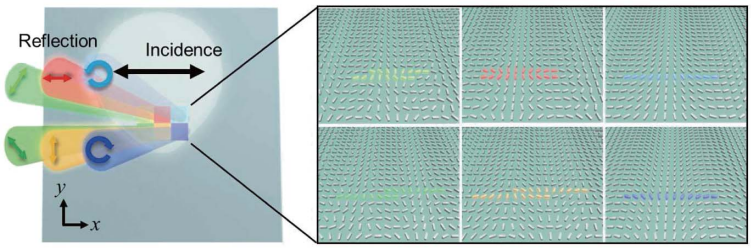

Schematic of multiple polarization generation with aluminum plasmonic metasurfaces. The right panels show six regions to generate the different polarization states. Reprinted with permission from Wu *et al.*, Nano Lett. **17**, 445–452 (2017) [362]. Copyright 2017 American Chemical Society.

a long-held dream to realize virtual shaping of the electromagnetic shapes seen by detectors [369,370]. With phase-shift metasurfaces as covers, it is now possible to decouple the physical shape and the electromagnetic characteristics in broadband frequencies. For instance, a planar slab with linear phase distribution along the radial direction will behave like a pyramid to radar; thus the RCS is significantly reduced [84]. This proposal was validated by full-wave simulations in optical wavelengths ranging from 600 to 2800 nm and experimental characterization in microwave frequencies from 8 to 16 GHz with echo reflectance less than 10% in the whole range, providing a conceptually new method for RCS/LCS reduction [88].

The principle of virtual shaping has also been extended to the optical band. As demonstrated experimentally using subwavelength-scale gold nanoantennas, an ultrathin

Figure 62

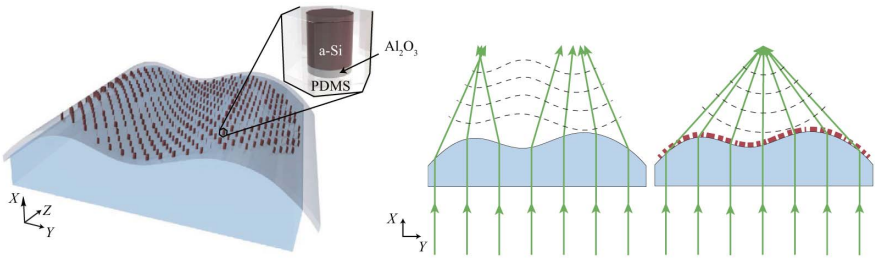

Conformal optics with dielectric metasurfaces. Left: schematic of a dielectric metasurface conformed to the surface of a transparent object with arbitrary geometry. Middle: side view of the arbitrarily shaped object showing how the object refracts light according to its geometry. Right: the same object with a thin dielectric metasurface layer conformed to its surface to change its optical response. Adapted with permission from Macmillan Publishers Ltd.: Kamali *et al.*, Nat. Commun. **7**, 11618 (2016) [372].

Figure 63

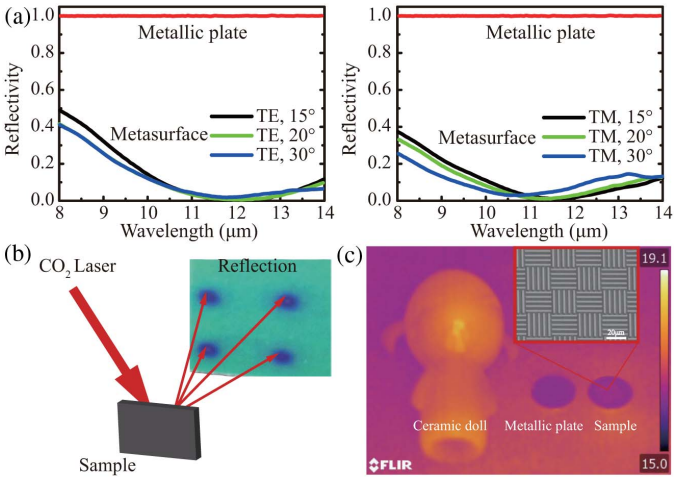

(a) Measured reflectivity of the metasurface under oblique incidence for TE and TM polarization. (b) Measured scattering pattern for the metasurface sample using a CO_2 laser. (c) Thermal infrared image of a ceramic doll, a metallic plate, and the fabricated sample. The inset is the SEM image of a part of the fabricated metasurface. From Xie *et al.*, Adv. Funct. Mater. **28**, 1706673 (2018) [179]. Adapted with permission from Wiley-VCH Verlag.

invisibility skin cloak (only 80 nm thick) was wrapped over an object [371] to conceal a 3D arbitrarily shaped object by complete restoration of the phase of the reflected light at a wavelength of 730 nm. Although the phase modulation scheme has been reported before [333], the fabrication recipe on curved structures provides a robust route towards practical applications. To further get around the strong ohmic loss of metallic structures, one may resort to the local phase modulation capability of the subwavelength dielectric resonators. As depicted in Fig. 62 [372], flexible dielectric metasurfaces are constructed by fabricating them on elastic substrates and then covered on a glass cylinder, which makes the cylinder behave like an aspherical lens focusing light to a point.

Virtual shaping is also a powerful means to realize infrared camouflage without increasing the infrared laser characteristics. It is known that Gustav's thermal radiation law has set a fundamental contradiction between the infrared reflection and thermal radiation. Based on virtual shaping, Xie *et al.* proposed an ultrathin plasmonic metasurface to simultaneously produce ultralow specular reflection and infrared emission across a broad spectrum and wide incident angle range [179], by combining the low emission nature of metal and the geometric phase in spatially inhomogeneous structures. A phase-gradient metasurface composed of subwavelength metal gratings was designed and experimentally characterized in the infrared atmosphere window of 8–14 μm, demonstrating an ultralow specular reflectivity and infrared emissivity below 0.1. Based on the local phase modulation, it was proved that an infrared illusion could be generated by the metasurface, enabling not only invisibility for thermal and laser detection, but also multi-functionalities for potential applications. The measured reflectivities of the metasurface under TE- and TM-polarized illumination in 8–14 μm are shown in Fig. 63(a), along with a same-sized gold plate without subwavelength gratings.

To check the scattering pattern of the metasurface, a CO_2 laser beam is illuminated on the sample with a small oblique angle of ∼10°, and the reflection signal is collected with an infrared color plate. Four spots are clearly observed on the color plate, indicating four reflected beams [Fig. 63(b)]. The low infrared emission property is characterized by comparing the thermal infrared image of the fabricated sample with a ceramic doll and a metallic plate using a commercial thermal infrared imager. Clearly, the apparent temperature of the ceramic doll is much higher than that of the metallic plate and the metasurface sample, indicating that the metasurface has a low infrared emission similar to that of metal [Fig. 63(c)].

7. CONCLUSIONS AND PERSPECTIVES

As one of the most fundamental behaviors of light, interference has received continuous attention since it was observed by Thomas Young in 1801. Traditional interference occurs at a length scale larger than the wavelength, thus limiting the characteristic length (period, thickness, etc.) of functional devices. Subwavelength interference was originally proposed in the mid-20th century to count the quantum or statistical properties of light [59]. Although it is possible to obtain subwavelength patterns by joint-intensity measurement, it is not practical to realize using traditional experimental conditions. Since the discovery of EYI on a metallic surface in this century [17–19, 29,373,374], it has been known that the classical light can induce deep-subwavelength interference patterns on structured surfaces. Based on these novel physical processes, various subwavelength devices have been realized for a wide range of optical applications, including sub-diffraction-limited imaging, nanolithography, flat lenses, beam shaping, antennas, and absorbers. Figure 64 shows a schematic of the development of some typical functional devices and systems enabled by EYI and M-wave. It should be

noted that besides improving the performance of traditional optical elements, the complex subwavelength structures also enable many functionalities that are not available for traditional materials, including multispectral, multifunctional, and multiphysical applications [179,375,376].

Based on active materials, tunable subwavelength devices have also been extensively studied. For instance, nanoslits-based plasmonic lenses may become actively tunable by filling the nanoslits with Kerr nonlinear media [377] and phase-change material [378–380]. With mechanical and micro-electromechanical systems (MEMS), the geometric parameters could be adjusted to realize tunable lens and color generation [381–383]. By combining active diodes with metallic circuits, arbitrary beam scanning and dynamic metamaterials have also been realized [51,384–386]. Nevertheless, it is still challenging to realize all-electric tunable devices with subwavelength pixel size in the optical regime.

Regarding the fundamental limitations of optical performance, there are two research goals in the future: first, it is of paramount importance to reduce the characteristic length, including the lithography resolution and device thickness, etc., by using the deep-subwavelength interference effect. Second, broadband operation, either in temporal frequency or in spatial frequency, is indispensable for many optical applications. For instance, the perfect imaging system requires an OTF with infinite spatial-frequency bandwidth, while an ideal blackbody absorber needs to absorb waves in the entire electromagnetic spectrum.

Considering the great promises and existing challenges, more efforts must be devoted in the future. Among the diverse research hotspots, we think the following two points deserve special considerations. First, the mathematical–physical models and design methodologies for subwavelength interference should be established and optimized for typical combinations of optical materials and structures. Like the transformation optics and effective materials parameter retrieval method, proper models will boost both the understanding and control of subwavelength light–matter interaction.

Figure 64

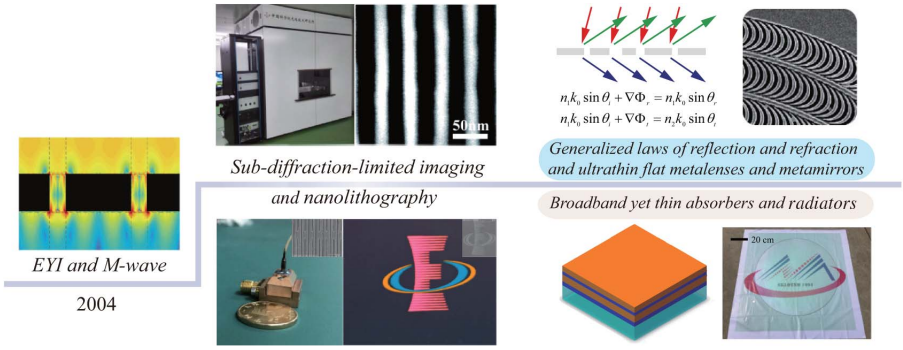

Illustration of the typical applications enabled by EYI and M-wave. The inset figures are reprinted with permission. Left panel: reprinted with permission from Luo and Ishihara, Appl. Phys. Lett. **84**, 4780–4782 (2004) [17]. Copyright 2004 AIP Publishing LLC. Middle panel: reprinted with permission from Luo, Natl. Sci. Rev. **5**, 137–138 (2018) [69]. Copyright 2018, the authors. Top right panel: reproduced from [41] under the terms of the Creative Commons Attribution NonCommercial License. Bottom right panel: reprinted with permission from Huang *et al.*, Appl. Phys. Express **10**, 112601 (2017) [260]. Copyright 2017 The Japan Society of Applied Physics.

In particular, dispersion engineering has been proposed as a powerful methodology to control subwavelength interference, which greatly improves the performance of metalenses, metamirrors, polarization convertors, structural colors, and electromagnetic absorbers [387,388]. On the other hand, artificial intelligence and big data technologies may be employed in next-generation subwavelength optics. Since subwavelength optical devices and systems have a great deal of design freedom, design methods based on trial-and-error may not get the optimal results for both periodic and aperiodic structures. Although many optimization algorithms such as simulated annealing (SA), GA, and PSO have been extensively investigated, they are only suitable for forward optimization; i.e., the geometric shapes are fixed. Recently, the emergence of artificial intelligence has provided a promising method to realize inverse and optimized design of subwavelength structures. For instance, a generative network has been constructed to produce a candidate geometric pattern in order to match input spectra at an average accuracy of about 0.9 [389].

In summary, we have outlined the recent global research interests in subwavelength interference effects within subwavelength structured metal–dielectric composites. The fundamental theories, design methodologies, fabrication recipes, and potential engineering applications are reviewed. With the greatly reduced scale for light–matter interaction, we believe that this topic will still be a hot topic in the foreseeable future, and act as one core of Engineering Optics 2.0 [8]. Meanwhile, we shall witness a transition of research from theoretical breakthroughs to technological revolutions and industrial applications.

FUNDING

973 Program of China (2013CBA01700); RIE2020 Advanced Manufacturing and Engineering (AME) Individual Research Grant (IPG) (A1883c0010).

REFERENCES

1. E. Ozbay, "Plasmonics: merging photonics and electronics at nanoscale dimensions," Science **311**, 189–193 (2006).
2. H. Hashemi, B. Zhang, J. D. Joannopoulos, and S. G. Johnson, "Delay-bandwidth and delay-loss limitations for cloaking of large objects," Phys. Rev. Lett. **104**, 253903 (2010).
3. F. Qin and M. Hong, "Breaking the diffraction limit in far field by planar metalens," Sci. China Phys. Mech. Astron. **60**, 044231 (2017).
4. E. Yablonovitch, "Photonic crystals: semiconductors of light," Sci. Am. **285**, 46–55 (2001).
5. W. L. Barnes, A. Dereux, and T. W. Ebbesen, "Surface plasmon subwavelength optics," Nature **424**, 824–830 (2003).
6. V. G. Veselago and E. E. Narimanov, "The left hand of brightness: past, present and future of negative index materials," Nat. Mater. **5**, 759–762 (2006).
7. M. Khorasaninejad and F. Capasso, "Metalenses: versatile multifunctional photonic components," Science **358**, eaam8100 (2017).
8. X. Luo, "Subwavelength optical engineering with metasurface waves," Adv. Opt. Mater. **6**, 1701201 (2018).
9. S. B. Glybovski, S. A. Tretyakov, P. A. Belov, Y. S. Kivshar, and C. R. Simovski, "Metasurfaces: from microwaves to visible," Phys. Rep. **634**, 1–72 (2016).
10. A. V. Kildishev, A. Boltasseva, and V. M. Shalaev, "Planar photonics with metasurfaces," Science **339**, 1232009 (2013).

11. Y. Cui, Y. He, Y. Jin, F. Ding, L. Yang, Y. Ye, S. Zhong, Y. Lin, and S. He, "Plasmonic and metamaterial structures as electromagnetic absorbers," Laser Photon. Rev. **8**, 495–520 (2014).
12. F. Ding, A. Pors, and S. I. Bozhevolnyi, "Gradient metasurfaces: a review of fundamentals and applications," Rep. Prog. Phys. **81**, 026401 (2018).
13. H.-T. Chen, A. J. Taylor, and N. Yu, "A review of metasurfaces: physics and applications," Rep. Prog. Phys. **79**, 076401 (2016).
14. A. E. Minovich, A. E. Miroshnichenko, A. Y. Bykov, T. V. Murzina, D. N. Neshev, and Y. S. Kivshar, "Functional and nonlinear optical metasurfaces," Laser Photon. Rev. **9**, 195–213 (2015).
15. A. V. Zayats, I. I. Smolyaninov, and A. A. Maradudin, "Nano-optics of surface plasmon polaritons," Phys. Rep. **408**, 131–314 (2005).
16. X. Luo and T. Ishihara, "Subwavelength photolithography based on surface-plasmon polariton resonance," Opt. Express **12**, 3055–3065 (2004).
17. X. Luo and T. Ishihara, "Surface plasmon resonant interference nanolithography technique," Appl. Phys. Lett. **84**, 4780–4782 (2004).
18. M. Pu, Y. Guo, X. Li, X. Ma, and X. Luo, "Revisitation of extraordinary Young's interference: from catenary optical fields to spin-orbit interaction in metasurfaces," ACS Photon. **5**, 3198–3204 (2018).
19. H. F. Schouten, N. Kuzmin, G. Dubois, T. D. Visser, G. Gbur, P. F. A. Alkemade, H. Blok, G. W. Hooft, D. Lenstra, and E. R. Eliel, "Plasmon-assisted two-slit transmission: Young's experiment revisited," Phys. Rev. Lett. **94**, 053901 (2005).
20. J. B. Pendry, "Negative refraction makes a perfect lens," Phys. Rev. Lett. **85**, 3966–3969 (2000).
21. T. W. Ebbesen, H. J. Lezec, H. F. Ghaemi, T. Thio, and P. A. Wolff, "Extraordinary optical transmission through sub-wavelength hole arrays," Nature **391**, 667–669 (1998).
22. L. Martin-Moreno, F. J. Garcia-Vidal, H. J. Lezec, K. M. Pellerin, T. Thio, J. B. Pendry, and T. W. Ebbesen, "Theory of extraordinary optical transmission through subwavelength hole arrays," Phys. Rev. Lett. **86**, 1114–1117 (2001).
23. H. Liu and P. Lalanne, "Microscopic theory of the extraordinary optical transmission," Nature **452**, 728–731 (2008).
24. H. A. Atwater, "The promise of plasmonics," Sci. Am. **296**, 56–62 (2007).
25. D. K. Gramotnev and S. I. Bozhevolnyi, "Plasmonics beyond the diffraction limit," Nat. Photonics **4**, 83–91 (2010).
26. F. J. Garcia-Vidal, L. Martin-Moreno, T. W. Ebbesen, and L. Kuipers, "Light passing through subwavelength apertures," Rev. Mod. Phys. **82**, 729–787 (2010).
27. Y. Li, F. Liu, L. Xiao, K. Cui, X. Feng, W. Zhang, and Y. Huang, "Two-surface-plasmon-polariton-absorption based nanolithography," Appl. Phys. Lett. **102**, 063113 (2013).
28. M. Pu, X. Ma, X. Li, Y. Guo, and X. Luo, "Merging plasmonics and metamaterials by two-dimensional subwavelength structures," J. Mater. Chem. C **5**, 4361–4378 (2017).
29. H. Shi, X. Luo, and C. Du, "Young's interference of double metallic nanoslit with different widths," Opt. Express **15**, 11321–11327 (2007).
30. T. Xu, Y. Zhao, D. Gan, C. Wang, C. Du, and X. Luo, "Directional excitation of surface plasmons with subwavelength slits," Appl. Phys. Lett. **92**, 101501 (2008).
31. T. Xu, L. Fang, J. Ma, B. Zeng, Y. Liu, J. Cui, C. Wang, Q. Feng, and X. Luo, "Localizing surface plasmons with a metal-cladding superlens for projecting deep-subwavelength patterns," Appl. Phys. B **97**, 175–179 (2009).

32. P. Gao, N. Yao, C. Wang, Z. Zhao, Y. Luo, Y. Wang, G. Gao, K. Liu, C. Zhao, and X. Luo, "Enhancing aspect profile of half-pitch 32 nm and 22 nm lithography with plasmonic cavity lens," Appl. Phys. Lett. **106**, 093110 (2015).
33. L. Bourke and R. J. Blaikie, "Genetic algorithm optimization of grating coupled near-field interference lithography systems at extreme numerical apertures," J. Opt. **19**, 095003 (2017).
34. T. Xu, C. Du, C. Wang, and X. Luo, "Subwavelength imaging by metallic slab lens with nanoslits," Appl. Phys. Lett. **91**, 201501 (2007).
35. L. Verslegers, P. B. Catrysse, Z. Yu, J. S. White, E. S. Barnard, M. L. Brongersma, and S. Fan, "Planar lenses based on nanoscale slit arrays in a metallic film," Nano Lett. **9**, 235–238 (2009).
36. L. Lin, X. M. Goh, L. P. McGuinness, and A. Roberts, "Plasmonic lenses formed by two-dimensional nanometric cross-shaped aperture arrays for Fresnel-region focusing," Nano Lett. **10**, 1936–1940 (2010).
37. S. Ishii, V. M. Shalaev, and A. V. Kildishev, "Holey-metal lenses: sieving single modes with proper phases," Nano Lett. **13**, 159–163 (2013).
38. X. Luo, "Principles of electromagnetic waves in metasurfaces," Sci. China Phys. Mech. Astron. **58**, 594201 (2015).
39. T. Xu, C. Wang, C. Du, and X. Luo, "Plasmonic beam deflector," Opt. Express **16**, 4753–4759 (2008).
40. N. Yu, P. Genevet, M. A. Kats, F. Aieta, J.-P. Tetienne, F. Capasso, and Z. Gaburro, "Light propagation with phase discontinuities: generalized laws of reflection and refraction," Science **334**, 333–337 (2011).
41. M. Pu, X. Li, X. Ma, Y. Wang, Z. Zhao, C. Wang, C. Hu, P. Gao, C. Huang, H. Ren, X. Li, F. Qin, J. Yang, M. Gu, M. Hong, and X. Luo, "Catenary optics for achromatic generation of perfect optical angular momentum," Sci. Adv. **1**, e1500396 (2015).
42. H. Sun, "The mystical interlinks: mechanics, religion or optics?" Sci. China Phys. Mech. Astron. **59**, 614202 (2016).
43. X. Li, L. Chen, Y. Li, X. Zhang, M. Pu, Z. Zhao, X. Ma, Y. Wang, M. Hong, and X. Luo, "Multicolor 3D meta-holography by broadband plasmonic modulation," Sci. Adv. **2**, e1601102 (2016).
44. F. Zhang, M. Pu, X. Li, P. Gao, X. Ma, J. Luo, H. Yu, and X. Luo, "All-dielectric metasurfaces for simultaneous giant circular asymmetric transmission and wavefront shaping based on asymmetric photonic spin-orbit interactions," Adv. Funct. Mater. **27**, 1704295 (2017).
45. R. C. Devlin, A. Ambrosio, N. A. Rubin, J. P. B. Mueller, and F. Capasso, "Arbitrary spin-to-orbital angular momentum conversion of light," Science **358**, 896–901 (2017).
46. S. Wang, P. C. Wu, V.-C. Su, Y.-C. Lai, M.-K. Chen, H. Y. Kuo, B. H. Chen, Y. H. Chen, T.-T. Huang, J.-H. Wang, R.-M. Lin, C.-H. Kuan, T. Li, Z. Wang, S. Zhu, and D. P. Tsai, "A broadband achromatic metalens in the visible," Nat. Nanotechnol. **13**, 227–232 (2018).
47. E. Maguid, I. Yulevich, D. Veksler, V. Kleiner, M. L. Brongersma, and E. Hasman, "Photonic spin-controlled multifunctional shared-aperture antenna array," Science **352**, 1202–1206 (2016).
48. B. Chambers and A. Tennant, "The phase-switched screen," IEEE Antennas Propag. Mag. **46**(6), 23–37 (2004).
49. D. Sievenpiper, L. Zhang, R. Broas, N. Alexopolous, and E. Yablonovitch, "High-impedance electromagnetic surfaces with a forbidden frequency band," IEEE Trans. Microwave Theory Tech. **47**, 2059–2074 (1999).

50. N. Engheta, "Thin absorbing screens using metamaterial surfaces," in *IEEE Antennas and Propagation Society International Symposium* (IEEE, 2002), Vol. **2**, pp. 392–395.
51. D. F. Sievenpiper, J. H. Schaffner, H. J. Song, R. Y. Loo, and G. Tangonan, "Two-dimensional beam steering using an electrically tunable impedance surface," IEEE Trans. Antennas Propag. **51**, 2713–2722 (2003).
52. H.-T. Chen, "Interference theory of metamaterial perfect absorbers," Opt. Express **20**, 7165–7172 (2012).
53. M. Pu, C. Hu, M. Wang, C. Huang, Z. Zhao, C. Wang, Q. Feng, and X. Luo, "Design principles for infrared wide-angle perfect absorber based on plasmonic structure," Opt. Express **19**, 17413–17420 (2011).
54. A. Kazemzadeh, "Nonmagnetic ultrawideband absorber with optimal thickness," IEEE Trans. Antennas Propag. **59**, 135–140 (2011).
55. Q. Feng, M. Pu, C. Hu, and X. Luo, "Engineering the dispersion of metamaterial surface for broadband infrared absorption," Opt. Lett. **37**, 2133–2135 (2012).
56. L. Mandel and E. Wolf, "Coherence properties of optical fields," Rev. Mod. Phys. **37**, 231–287 (1965).
57. J. Xiong, D.-Z. Cao, F. Huang, H.-G. Li, X.-J. Sun, and K. Wang, "Experimental observation of classical subwavelength interference with a pseudothermal light source," Phys. Rev. Lett. **94**, 173601 (2005).
58. A. N. Boto, P. Kok, D. S. Abrams, S. L. Braunstein, C. P. Williams, and J. P. Dowling, "Quantum interferometric optical lithography: exploiting entanglement to beat the diffraction limit," Phys. Rev. Lett. **85**, 2733–2736 (2000).
59. R. W. Boyd and J. P. Dowling, "Quantum lithography: status of the field," Quantum Inf. Process. **11**, 891–901 (2012).
60. F. J. García de Abajo, "Colloquium: light scattering by particle and hole arrays," Rev. Mod. Phys. **79**, 1267–1290 (2007).
61. A. E. Miroshnichenko, S. Flach, and Y. S. Kivshar, "Fano resonances in nanoscale structures," Rev. Mod. Phys. **82**, 2257–2298 (2010).
62. M. Lapine, I. V. Shadrivov, and Y. S. Kivshar, "Colloquium: nonlinear metamaterials," Rev. Mod. Phys. **86**, 1093–1123 (2014).
63. N. Yu and F. Capasso, "Flat optics with designer metasurfaces," Nat. Mater. **13**, 139–150 (2014).
64. R. P. Crease, "The most beautiful experiment," Phys. World **15**, 19 (2002).
65. J. S. Fakonas, H. Lee, Y. A. Kelaita, and H. A. Atwater, "Two-plasmon quantum interference," Nat. Photonics **8**, 317–320 (2014).
66. M. R. Singh, K. Davieau, and J. J. L. Carson, "Effect of quantum interference on absorption of light in metamaterial hybrids," J. Phys. D **49**, 445103 (2016).
67. D. C. Flanders, "Submicrometer periodicity gratings as artificial anisotropic dielectrics," Appl. Phys. Lett. **42**, 492–494 (1983).
68. P. Lalanne and J.-P. Hugonin, "High-order effective-medium theory of subwavelength gratings in classical mounting: application to volume holograms," J. Opt. Soc. Am. A **15**, 1843–1851 (1998).
69. X. Luo, "Plasmonic metalens for nanofabrication," Natl. Sci. Rev. **5**, 137–138 (2018).
70. Z. Liu, Q. Wei, and X. Zhang, "Surface plasmon interference nanolithography," Nano Lett. **5**, 957–961 (2005).
71. Z. Liu, Y. Wang, J. Yao, H. Lee, W. Srituravanich, and X. Zhang, "Broad band two-dimensional manipulation of surface plasmons," Nano Lett. **9**, 462–466 (2008).
72. I. Epstein, Y. Tsur, and A. Arie, "Surface-plasmon wavefront and spectral shaping by near-field holography," Laser Photon. Rev. **10**, 360–381 (2016).

73. R. Welti, "Light transmission through two slits: the Young experiment revisited," J. Opt. A **8**, 606–609 (2006).
74. R. Gordon, "Near-field interference in a subwavelength double slit in a perfect conductor," J. Opt. A **8**, L1–L3 (2006).
75. G. Lerosey, D. F. P. Pile, P. Matheu, G. Bartal, and X. Zhang, "Controlling the phase and amplitude of plasmon sources at a subwavelength scale," Nano Lett. **9**, 327–331 (2009).
76. J. Lin, J. P. B. Mueller, Q. Wang, G. Yuan, N. Antoniou, X.-C. Yuan, and F. Capasso, "Polarization-controlled tunable directional coupling of surface plasmon polaritons," Science **340**, 331–334 (2013).
77. S. Xiao, F. Zhong, H. Liu, S. Zhu, and J. Li, "Flexible coherent control of plasmonic spin-Hall effect," Nat. Commun. **6**, 8360 (2015).
78. X. Luo, M. Pu, X. Li, and X. Ma, "Broadband spin Hall effect of light in single nanoapertures," Light Sci. Appl. **6**, e16276 (2017).
79. H. J. Lezec, A. Degiron, E. Devaux, R. A. Linke, L. Martin-Moreno, F. J. Garcia-Vidal, and T. W. Ebbesen, "Beaming light from a subwavelength aperture," Science **297**, 820–822 (2002).
80. M. Pu, X. Ma, Y. Guo, X. Li, and X. Luo, "Theory of microscopic meta-surface waves based on catenary optical fields and dispersion," Opt. Express **26**, 19555–19562 (2018).
81. M. Esfandyarpour, E. C. Garnett, Y. Cui, M. D. McGehee, and M. L. Brongersma, "Metamaterial mirrors in optoelectronic devices," Nat. Nanotechnol. **9**, 542–547 (2014).
82. L. J. Chu, "Physical limitations of omni-directional antennas," J. Appl. Phys. **19**, 1163–1175 (1948).
83. M. Pu, P. Chen, Y. Wang, Z. Zhao, C. Huang, C. Wang, X. Ma, and X. Luo, "Anisotropic meta-mirror for achromatic electromagnetic polarization manipulation," Appl. Phys. Lett. **102**, 131906 (2013).
84. M. Pu, Z. Zhao, Y. Wang, X. Li, X. Ma, C. Hu, C. Wang, C. Huang, and X. Luo, "Spatially and spectrally engineered spin-orbit interaction for achromatic virtual shaping," Sci. Rep. **5**, 9822 (2015).
85. Y. Guo, Y. Wang, M. Pu, Z. Zhao, X. Wu, X. Ma, C. Wang, L. Yan, and X. Luo, "Dispersion management of anisotropic metamirror for super-octave bandwidth polarization conversion," Sci. Rep. **5**, 8434 (2015).
86. N. K. Grady, J. E. Heyes, D. R. Chowdhury, Y. Zeng, M. T. Reiten, A. K. Azad, A. J. Taylor, D. A. R. Dalvit, and H.-T. Chen, "Terahertz metamaterials for linear polarization conversion and anomalous refraction," Science **340**, 1304–1307 (2013).
87. Z. Zhang, J. Luo, M. Song, and H. Yu, "Large-area, broadband and high-efficiency near-infrared linear polarization manipulating metasurface fabricated by orthogonal interference lithography," Appl. Phys. Lett. **107**, 241904 (2015).
88. Y. Guo, L. Yan, W. Pan, and L. Shao, "Scattering engineering in continuously shaped metasurface: an approach for electromagnetic illusion," Sci. Rep. **6**, 30154 (2016).
89. L. Bourke and R. J. Blaikie, "Herpin effective media resonant underlayers and resonant overlayer designs for ultra-high NA interference lithography," J. Opt. Soc. Am. A **34**, 2243–2249 (2017).
90. L. Liu, Y. Luo, Z. Zhao, W. Zhang, G. Gao, B. Zeng, C. Wang, and X. Luo, "Large area and deep sub-wavelength interference lithography employing odd surface plasmon modes," Sci. Rep. **6**, 30450 (2016).
91. L. Liu, X. Zhang, Z. Zhao, M. Pu, P. Gao, Y. Luo, J. Jin, C. Wang, and X. Luo, "Batch fabrication of metasurface holograms enabled by plasmonic cavity lithography," Adv. Opt. Mater. **5**, 1700429 (2017).

92. L. Liu, P. Gao, K. Liu, W. Kong, Z. Zhao, M. Pu, C. Wang, and X. Luo, "Nanofocusing of circularly polarized Bessel-type plasmon polaritons with hyperbolic metamaterials," Mater. Horiz. **4**, 290–296 (2017).
93. J. Sun, X. Wang, T. Xu, Z. A. Kudyshev, A. N. Cartwright, and N. M. Litchinitser, "Spinning light on the nanoscale," Nano Lett. **14**, 2726–2729 (2014).
94. M. Rahmani, A. E. Miroshnichenko, D. Y. Lei, B. Luk'yanchuk, M. I. Tribelsky, A. I. Kuznetsov, Y. S. Kivshar, Y. Francescato, V. Giannini, M. Hong, and S. A. Maier, "Beyond the hybridization effects in plasmonic nanoclusters: diffraction-induced enhanced absorption and scattering," Small **10**, 576–583 (2014).
95. J. Khurgin, W.-Y. Tsai, D. P. Tsai, and G. Sun, "Landau damping and limit to field confinement and enhancement in plasmonic dimers," ACS Photon. **4**, 2871–2880 (2017).
96. S. S. Aćimović, M. P. Kreuzer, M. U. González, and R. Quidant, "Plasmon near-field coupling in metal dimers as a step toward single-molecule sensing," ACS Nano **3**, 1231–1237 (2009).
97. H. Aouani, M. Rahmani, M. Navarro-Cia, and S. A. Maier, "Third-harmonic-upconversion enhancement from a single semiconductor nanoparticle coupled to a plasmonic antenna," Nat. Nanotechnol. **9**, 290–294 (2014).
98. V. A. Fedotov, M. Rose, S. L. Prosvirnin, N. Papasimakis, and N. I. Zheludev, "Sharp trapped-mode resonances in planar metamaterials with a broken structural symmetry," Phys. Rev. Lett. **99**, 147401 (2007).
99. Y. Yang, I. I. Kravchenko, D. P. Briggs, and J. Valentine, "All-dielectric metasurface analogue of electromagnetically induced transparency," Nat. Commun. **5**, 5753 (2014).
100. M. Pu, C. Hu, C. Huang, C. Wang, Z. Zhao, Y. Wang, and X. Luo, "Investigation of Fano resonance in planar metamaterial with perturbed periodicity," Opt. Express **21**, 992–1001 (2013).
101. M. Rahmani, B. Luk'yanchuk, and M. Hong, "Fano resonance in novel plasmonic nanostructures," Laser Photon. Rev. **7**, 329–349 (2013).
102. C. Wu and G. Shvets, "Design of metamaterial surfaces with broadband absorbance," Opt. Lett. **37**, 308–310 (2012).
103. M. Caldarola, P. Albella, E. Cortés, M. Rahmani, T. Roschuk, G. Grinblat, R. F. Oulton, A. V. Bragas, and S. A. Maier, "Non-plasmonic nanoantennas for surface enhanced spectroscopies with ultra-low heat conversion," Nat. Commun. **6**, 7915 (2015).
104. D. G. Baranov, S. V. Makarov, A. E. Krasnok, P. A. Belov, and A. Alù, "Tuning of near- and far-field properties of all-dielectric dimer nanoantennas via ultrafast electron-hole plasma photoexcitation," Laser Photon. Rev. **10**, 1009–1015 (2016).
105. W. Singer, M. Totzek, and H. Gross, *Physical Image Formation* (Wiley, 2005).
106. N. I. Zheludev, "What diffraction limit?" Nat. Mater. **7**, 420–422 (2008).
107. L. Chen, Y. Zhou, M. Wu, and M. Hong, "Remote-mode microsphere nanoimaging: new boundaries for optical microscopes," Opto-Electron. Adv. **1**, 170001 (2018).
108. B. Wood, J. B. Pendry, and D. P. Tsai, "Directed subwavelength imaging using a layered metal-dielectric system," Phys. Rev. B **74**, 115116 (2006).
109. W. Wang, H. Xing, L. Fang, Y. Liu, J. Ma, L. Lin, C. Wang, and X. Luo, "Far-field imaging device: planar hyperlens with magnification using multi-layer metamaterial," Opt. Express **16**, 21142–21148 (2008).
110. S. Han, Y. Xiong, D. Genov, Z. Liu, G. Bartal, and X. Zhang, "Ray optics at a deep-subwavelength scale: a transformation optics approach," Nano Lett. **8**, 4243–4247 (2008).

111. Z. Liu, H. Lee, Y. Xiong, C. Sun, and X. Zhang, "Far-field optical hyperlens magnifying sub-diffraction-limited objects," Science **315**, 1686 (2007).
112. L. Liu, K. Liu, Z. Zhao, C. Wang, P. Gao, and X. Luo, "Sub-diffraction demagnification imaging lithography by hyperlens with plasmonic reflector layer," RSC Adv. **6**, 95973–95978 (2016).
113. J. Sun, T. Xu, and N. M. Litchinitser, "Experimental demonstration of demagnifying hyperlens," Nano Lett. **16**, 7905–7909 (2016).
114. S.-A. Biehs, M. Tschikin, and P. Ben-Abdallah, "Hyperbolic metamaterials as an analog of a blackbody in the near field," Phys. Rev. Lett. **109**, 104301 (2012).
115. Y. Guo, C. L. Cortes, S. Molesky, and Z. Jacob, "Broadband super-Planckian thermal emission from hyperbolic metamaterials," Appl. Phys. Lett. **101**, 131106 (2012).
116. H. N. S. Krishnamoorthy, Z. Jacob, E. Narimanov, I. Kretzschmar, and V. M. Menon, "Topological transitions in metamaterials," Science **336**, 205–209 (2012).
117. G. Liang, C. Wang, Z. Zhao, Y. Wang, N. Yao, P. Gao, Y. Luo, G. Gao, Q. Zhao, and X. Luo, "Squeezing bulk plasmon polaritons through hyperbolic metamaterial for large area deep subwavelength interference lithography," Adv. Opt. Mater. **3**, 1248–1256 (2015).
118. Z. Zhao, Y. Luo, W. Zhang, C. Wang, P. Gao, Y. Wang, M. Pu, N. Yao, C. Zhao, and X. Luo, "Going far beyond the near-field diffraction limit via plasmonic cavity lens with high spatial frequency spectrum off-axis illumination," Sci. Rep. **5**, 15320 (2015).
119. E. T. F. Rogers and N. I. Zheludev, "Optical super-oscillations: sub-wavelength light focusing and super-resolution imaging," J. Opt. **15**, 094008 (2013).
120. G. Lerosey, J. de Rosny, A. Tourin, and M. Fink, "Focusing beyond the diffraction limit with far-field time reversal," Science **315**, 1120–1122 (2007).
121. C. Wang, D. Tang, Y. Wang, Z. Zhao, J. Wang, M. Pu, Y. Zhang, W. Yan, P. Gao, and X. Luo, "Super-resolution optical telescopes with local light diffraction shrinkage," Sci. Rep. **5**, 18485 (2015).
122. A. Ciattoni, B. Crosignani, and P. Di Porto, "Vectorial free-space optical propagation: a simple approach for generating all-order nonparaxial corrections," Opt. Commun. **177**, 9–13 (2000).
123. E. T. F. Rogers, J. Lindberg, T. Roy, S. Savo, J. E. Chad, M. R. Dennis, and N. I. Zheludev, "A super-oscillatory lens optical microscope for subwavelength imaging," Nat. Mater. **11**, 432–435 (2012).
124. K. Huang, H. Ye, J. Teng, S. P. Yeo, B. S. Luk'yanchuk, and C. Qiu, "Optimization-free superoscillatory lens using phase and amplitude masks," Laser Photon. Rev. **8**, 152–157 (2014).
125. D. Tang, C. Wang, Z. Zhao, Y. Wang, M. Pu, X. Li, P. Gao, and X. Luo, "Ultrabroadband superoscillatory lens composed by plasmonic metasurfaces for subdiffraction light focusing," Laser Photon. Rev. **9**, 713–719 (2015).
126. Z. Li, T. Zhang, Y. Wang, W. Kong, J. Zhang, Y. Huang, C. Wang, X. Li, M. Pu, and X. Luo, "Achromatic broadband super-resolution imaging by superoscillatory metasurface," Laser Photon. Rev. **12**, 1800064 (2018).
127. Y. Xu, Y. Fu, and H. Chen, "Planar gradient metamaterials," Nat. Rev. Mater. **1**, 16067 (2016).
128. C. Pfeiffer and A. Grbic, "Metamaterial Huygens' surfaces: tailoring wave fronts with reflectionless sheets," Phys. Rev. Lett. **110**, 197401 (2013).
129. C. Pfeiffer, N. K. Emani, A. M. Shaltout, A. Boltasseva, V. M. Shalaev, and A. Grbic, "Efficient light bending with isotropic metamaterial Huygens' surfaces," Nano Lett. **14**, 2491–2497 (2014).

130. A. H. Abdelrahman, A. Z. Elsherbeni, and F. Yang, "Transmission phase limit of multilayer frequency-selective surfaces for transmitarray designs," IEEE Trans. Antennas Propag. **62**, 690–697 (2014).
131. M. Pu, P. Chen, Y. Wang, Z. Zhao, C. Wang, C. Huang, C. Hu, and X. Luo, "Strong enhancement of light absorption and highly directive thermal emission in graphene," Opt. Express **21**, 11618–11627 (2013).
132. M. Pu, M. Wang, C. Hu, C. Huang, Z. Zhao, Y. Wang, and X. Luo, "Engineering heavily doped silicon for broadband absorber in the terahertz regime," Opt. Express **20**, 25513–25519 (2012).
133. S. Fan and J. D. Joannopoulos, "Analysis of guided resonances in photonic crystal slabs," Phys. Rev. B **65**, 235112 (2002).
134. A. F. Kaplan, T. Xu, and L. J. Guo, "High efficiency resonance-based spectrum filters with tunable transmission bandwidth fabricated using nanoimprint lithography," Appl. Phys. Lett. **99**, 143111 (2011).
135. R. W. Wood, "On a remarkable case of uneven distribution of light in a diffraction grating spectrum," Proc. Phys. Soc. London **18**, 269–275 (1902).
136. C. Hu, Z. Zhao, X. Chen, and X. Luo, "Realizing near-perfect absorption at visible frequencies," Opt. Express **17**, 11039–11044 (2009).
137. M. C. Hutley and D. Maystre, "The total absorption of light by a diffraction grating," Opt. Commun. **19**, 431–436 (1976).
138. M. Cai, O. Painter, and K. J. Vahala, "Observation of critical coupling in a fiber taper to a silica-microsphere whispering-gallery mode system," Phys. Rev. Lett. **85**, 74–77 (2000).
139. S. Chen, Z. Li, Y. Zhang, H. Cheng, and J. Tian, "Phase manipulation of electromagnetic waves with metasurfaces and its applications in nanophotonics," Adv. Opt. Mater. **6**, 1800104 (2018).
140. Y. Li, X. Li, M. Pu, Z. Zhao, X. Ma, Y. Wang, and X. Luo, "Achromatic flat optical components via compensation between structure and material dispersions," Sci. Rep. **6**, 19885 (2016).
141. J. Li, S. Chen, H. Yang, J. Li, P. Yu, H. Cheng, C. Gu, H.-T. Chen, and J. Tian, "Simultaneous control of light polarization and phase distributions using plasmonic metasurfaces," Adv. Funct. Mater. **25**, 704–710 (2015).
142. L. Kipp, M. Skibowski, R. L. Johnson, R. Berndt, R. Adelung, S. Harm, and R. Seemann, "Sharper images by focusing soft X-rays with photon sieves," Nature **414**, 184–188 (2001).
143. K. Huang, H. Liu, F. J. Garcia-Vidal, M. Hong, B. Luk'yanchuk, J. Teng, and C.-W. Qiu, "Ultrahigh-capacity non-periodic photon sieves operating in visible light," Nat. Commun. **6**, 7059 (2015).
144. P. R. West, S. Ishii, G. V. Naik, N. K. Emani, V. M. Shalaev, and A. Boltasseva, "Searching for better plasmonic materials," Laser Photon. Rev. **4**, 795–808 (2010).
145. S. Jahani and Z. Jacob, "All-dielectric metamaterials," Nat. Nanotechnol. **11**, 23–36 (2016).
146. A. I. Kuznetsov, A. E. Miroshnichenko, M. L. Brongersma, Y. S. Kivshar, and B. Luk'yanchuk, "Optically resonant dielectric nanostructures," Science **354**, aag2472 (2016).
147. S. Astilean, P. Lalanne, P. Chavel, E. Cambril, and H. Launois, "High-efficiency subwavelength diffractive element patterned in a high-refractive-index material for 633 nm," Opt. Lett. **23**, 552–554 (1998).
148. S. Wang, J. Lai, T. Wu, C. Chen, and J. Sun, "Wide-band achromatic flat focusing lens based on all-dielectric subwavelength metasurface," Opt. Express **25**, 7121–7130 (2017).

149. F. Monticone, N. M. Estakhri, and A. Alù, "Full control of nanoscale optical transmission with a composite metascreen," Phys. Rev. Lett. **110**, 203903 (2013).
150. M. Decker, I. Staude, M. Falkner, J. Dominguez, D. N. Neshev, I. Brener, T. Pertsch, and Y. S. Kivshar, "High-efficiency dielectric Huygens' surfaces," Adv. Opt. Mater. **3**, 813–820 (2015).
151. K. E. Chong, L. Wang, I. Staude, A. R. James, J. Dominguez, S. Liu, G. S. Subramania, M. Decker, D. N. Neshev, I. Brener, and Y. S. Kivshar, "Efficient polarization-insensitive complex wavefront control using Huygens' metasurfaces based on dielectric resonant meta-atoms," ACS Photon. **3**, 514–519 (2016).
152. J. Y. Lau and S. V. Hum, "Reconfigurable transmitarray design approaches for beamforming applications," IEEE Trans. Antennas Propag. **60**, 5679–5689 (2012).
153. W. Pan, C. Huang, P. Chen, M. Pu, X. Ma, and X. Luo, "A beam steering horn antenna using active frequency selective surface," IEEE Trans. Antennas Propag. **61**, 6218–6223 (2013).
154. J. Huang and J. A. Encinar, *Reflectarray Antennas* (Wiley, 2008).
155. J. A. Encinar and J. A. Zornoza, "Broadband design of three-layer printed reflectarrays," IEEE Trans. Antennas Propag. **51**, 1662–1664 (2003).
156. N. Engheta, "Circuits with light at nanoscales: optical nanocircuits inspired by metamaterials," Science **317**, 1698–1702 (2007).
157. Y. Guo, M. Pu, Z. Zhao, Y. Wang, J. Jin, P. Gao, X. Li, X. Ma, and X. Luo, "Merging geometric phase and plasmon retardation phase in continuously shaped metasurfaces for arbitrary orbital angular momentum generation," ACS Photon. **3**, 2022–2029 (2016).
158. A. G. Fox, "An adjustable wave-guide phase changer," Proc. IRE **35**, 1489–1498 (1947).
159. W. Sichak and D. J. Levine, "Microwave high-speed continuous phase shifter," Proc. IRE **43**, 1661–1663 (1955).
160. S. Pancharatnam, "Generalized theory of interference, and its applications. Part I. Coherent pencils," Proc. Indian Acad. Sci. A **44**, 247–262 (1956).
161. M. V. Berry, "Quantal phase factors accompanying adiabatic changes," Proc. R. Soc. A **392**, 45–57 (1984).
162. M. V. Berry, "The adiabatic phase and Pancharatnam's phase for polarized light," J. Mod. Opt. **34**, 1401–1407 (1987).
163. Z. Bomzon, V. Kleiner, and E. Hasman, "Pancharatnam–Berry phase in space-variant polarization-state manipulations with subwavelength gratings," Opt. Lett. **26**, 1424–1426 (2001).
164. R. Bhandari, "Polarization of light and topological phases," Phys. Rep. **281**, 1–64 (1997).
165. F. Gori, "Measuring Stokes parameters by means of a polarization grating," Opt. Lett. **24**, 584–586 (1999).
166. Z. Bomzon, G. Biener, V. Kleiner, and E. Hasman, "Space-variant Pancharatnam-Berry phase optical elements with computer-generated subwavelength gratings," Opt. Lett. **27**, 1141–1143 (2002).
167. E. Hasman, V. Kleiner, G. Biener, and A. Niv, "Polarization dependent focusing lens by use of quantized Pancharatnam–Berry phase diffractive optics," Appl. Phys. Lett. **82**, 328–330 (2003).
168. D. Lin, P. Fan, E. Hasman, and M. L. Brongersma, "Dielectric gradient metasurface optical elements," Science **345**, 298–302 (2014).
169. M. Khorasaninejad, W. T. Chen, R. C. Devlin, J. Oh, A. Y. Zhu, and F. Capasso, "Metalenses at visible wavelengths: diffraction-limited focusing and subwavelength resolution imaging," Science **352**, 1190–1194 (2016).

170. L. Huang, X. Chen, H. Mühlenbernd, G. Li, B. Bai, Q. Tan, G. Jin, T. Zentgraf, and S. Zhang, "Dispersionless phase discontinuities for controlling light propagation," Nano Lett. **12**, 5750–5755 (2012).
171. X. Chen, L. Huang, H. Mühlenbernd, G. Li, B. Bai, Q. Tan, G. Jin, C. W. Qiu, S. Zhang, and T. Zentgraf, "Dual-polarity plasmonic metalens for visible light," Nat. Commun. **3**, 1198 (2012).
172. B. H. Chen, P. C. Wu, V.-C. Su, Y.-C. Lai, C. H. Chu, I. C. Lee, J.-W. Chen, Y. H. Chen, Y.-C. Lan, C.-H. Kuan, and D. P. Tsai, "GaN metalens for pixel-level full-color routing at visible light," Nano Lett. **17**, 6345–6352 (2017).
173. Y. Wang, M. Pu, Z. Zhang, X. Li, X. Ma, Z. Zhao, and X. Luo, "Quasi-continuous metasurface for ultra-broadband and polarization-controlled electromagnetic beam deflection," Sci. Rep. **5**, 17733 (2015).
174. X. Li, M. Pu, Z. Zhao, X. Ma, J. Jin, Y. Wang, P. Gao, and X. Luo, "Catenary nanostructures as highly efficient and compact Bessel beam generators," Sci. Rep. **6**, 20524 (2016).
175. N. Shitrit, I. Bretner, Y. Gorodetski, V. Kleiner, and E. Hasman, "Optical spin Hall effects in plasmonic chains," Nano Lett. **11**, 2038–2042 (2011).
176. X. Ma, C. Huang, M. Pu, C. Hu, Q. Feng, and X. Luo, "Single-layer circular polarizer using metamaterial and its application in antenna," Microw. Opt. Technol. Lett. **54**, 1770–1774 (2012).
177. L. Young, L. A. Robinson, and C. Hacking, "Meander-line polarizer," IEEE Trans. Antennas Propag. **21**, 376–378 (1973).
178. J. Hao, Y. Yuan, L. Ran, T. Jiang, J. A. Kong, C. T. Chan, and L. Zhou, "Manipulating electromagnetic wave polarizations by anisotropic metamaterials," Phys. Rev. Lett. **99**, 063908 (2007).
179. X. Xie, X. Li, M. Pu, X. Ma, K. Liu, Y. Guo, and X. Luo, "Plasmonic metasurfaces for simultaneous thermal infrared invisibility and holographic illusion," Adv. Funct. Mater. **28**, 1706673 (2018).
180. X. Zhang, Z. Tian, W. Yue, J. Gu, S. Zhang, J. Han, and W. Zhang, "Broadband terahertz wave deflection based on C-shape complex metamaterials with phase discontinuities," Adv. Mater. **25**, 4567–4572 (2013).
181. X. Ni, N. K. Emani, A. V. Kildishev, A. Boltasseva, and V. M. Shalaev, "Broadband light bending with plasmonic nanoantennas," Science **335**, 427 (2012).
182. F. Aieta, P. Genevet, N. Yu, M. A. Kats, Z. Gaburro, and F. Capasso, "Out-of-plane reflection and refraction of light by anisotropic optical antenna metasurfaces with phase discontinuities," Nano Lett. **12**, 1702–1706 (2012).
183. X. Ni, S. Ishii, A. V. Kildishev, and V. M. Shalaev, "Ultra-thin, planar, Babinet-inverted plasmonic metalenses," Light Sci. Appl. **2**, e72 (2013).
184. X. Ni, A. V. Kildishev, and V. M. Shalaev, "Metasurface holograms for visible light," Nat. Commun. **4**, 2807 (2013).
185. X. Yin, Z. Ye, J. Rho, Y. Wang, and X. Zhang, "Photonic spin Hall effect at metasurfaces," Science **339**, 1405–1407 (2013).
186. F. Qin, L. Ding, L. Zhang, F. Monticone, C. C. Chum, J. Deng, S. Mei, Y. Li, J. Teng, M. Hong, S. Zhang, A. Alù, and C.-W. Qiu, "Hybrid bilayer plasmonic metasurface efficiently manipulates visible light," Sci. Adv. **2**, e1501168 (2016).
187. W. Wan, Y. Chong, L. Ge, H. Noh, A. D. Stone, and H. Cao, "Time-reversed lasing and interferometric control of absorption," Science **331**, 889–892 (2011).
188. M. Pu, Q. Feng, M. Wang, C. Hu, C. Huang, X. Ma, Z. Zhao, C. Wang, and X. Luo, "Ultrathin broadband nearly perfect absorber with symmetrical coherent illumination," Opt. Express **20**, 2246–2254 (2012).
189. M. Crescimanno, N. J. Dawson, and J. H. Andrews, "Coherent perfect rotation," Phys. Rev. A **86**, 031807 (2012).

190. Y. Wang, M. Pu, C. Hu, Z. Zhao, C. Wang, and X. Luo, "Dynamic manipulation of polarization states using anisotropic meta-surface," Opt. Commun. **319**, 14–16 (2014).
191. X. Li, M. Pu, Y. Wang, X. Ma, Y. Li, H. Gao, Z. Zhao, P. Gao, C. Wang, and X. Luo, "Dynamic control of the extraordinary optical scattering in semicontinuous 2D metamaterials," Adv. Opt. Mater. **4**, 659–663 (2016).
192. P. Yeh, *Optical Waves in Layered Media*, 2nd ed. (Wiley, 2005).
193. H. A. Macleod, *Thin-Film Optical Filters*, 4th ed. (CRC Press, 2010).
194. M. L. Brongersma, "Introductory lecture: nanoplasmonics," Faraday Discuss. **178**, 9–36 (2015).
195. E. Kretschmann and H. Raether, "Notizen: radiative decay of non radiative surface plasmons excited by light," Z. Naturforsch. A **23**, 2135–2136 (1968).
196. R. B. Pettit, J. Silcox, and R. Vincent, "Measurement of surface-plasmon dispersion in oxidized aluminum films," Phys. Rev. B **11**, 3116–3123 (1975).
197. F. Liu, L. Xiao, Y. Ye, M. Wang, K. Cui, X. Feng, W. Zhang, and Y. Huang, "Integrated Cherenkov radiation emitter eliminating the electron velocity threshold," Nat. Photonics **11**, 289–292 (2017).
198. K. A. Willets and R. P. V. Duyne, "Localized surface plasmon resonance spectroscopy and sensing," Annu. Rev. Phys. Chem. **58**, 267–297 (2007).
199. X. Zhang and Z. Liu, "Superlenses to overcome the diffraction limit," Nat. Mater. **7**, 435–441 (2008).
200. V. G. Veselago, "The electrodynamics of substances with simultaneously negative values of ε and μ," Sov. Phys. Usp. **10**, 509–514 (1968).
201. D. O. S. Melville and R. J. Blaikie, "Super-resolution imaging through a planar silver layer," Opt. Express **13**, 2127–2134 (2005).
202. N. Fang, H. Lee, C. Sun, and X. Zhang, "Sub-diffraction-limited optical imaging with a silver superlens," Science **308**, 534–537 (2005).
203. H. Liu, B. Wang, L. Ke, J. Deng, C. C. Choy, M. S. Zhang, L. Shen, S. A. Maier, and J. H. Teng, "High contrast superlens lithography engineered by loss reduction," Adv. Funct. Mater. **22**, 3777–3783 (2012).
204. Z. Guo, Q. Huang, C. Wang, P. Gao, W. Zhang, Z. Zhao, L. Yan, and X. Luo, "Negative and positive impact of roughness and loss on subwavelength imaging for superlens structures," Plasmonics **9**, 103–110 (2014).
205. T. Xu and H. J. Lezec, "Visible-frequency asymmetric transmission devices incorporating a hyperbolic metamaterial," Nat. Commun. **5**, 4141 (2014).
206. Z. Liu, J. M. Steele, W. Srituravanich, Y. Pikus, C. Sun, and X. Zhang, "Focusing surface plasmons with a plasmonic lens," Nano Lett. **5**, 1726–1729 (2005).
207. L. Yin, V. K. Vlasko-Vlasov, J. Pearson, J. M. Hiller, J. Hua, U. Welp, D. E. Brown, and C. W. Kimball, "Subwavelength focusing and guiding of surface plasmons," Nano Lett. **5**, 1399–1402 (2005).
208. Z. Fang, Q. Peng, W. Song, F. Hao, J. Wang, P. Nordlander, and X. Zhu, "Plasmonic focusing in symmetry broken nanocorrals," Nano Lett. **11**, 893–897 (2011).
209. E.-Y. Song, S.-Y. Lee, J. Hong, K. Lee, Y. Lee, G.-Y. Lee, H. Kim, and B. Lee, "A double-lined metasurface for plasmonic complex-field generation," Laser Photon. Rev. **10**, 299–306 (2016).
210. Y.-G. Chen, Y.-H. Chen, and Z.-Y. Li, "Direct method to control surface plasmon polaritons on metal surfaces," Opt. Lett. **39**, 339–342 (2014).
211. Y.-H. Chen, L. Huang, L. Gan, and Z.-Y. Li, "Wavefront shaping of infrared light through a subwavelength hole," Light Sci. Appl. **1**, e26 (2012).
212. P. Genevet, J. Lin, M. A. Kats, and F. Capasso, "Holographic detection of the orbital angular momentum of light with plasmonic photodiodes," Nat. Commun. **3**, 1278 (2012).

213. S. Sun, Q. He, S. Xiao, Q. Xu, X. Li, and L. Zhou, "Gradient-index metasurfaces as a bridge linking propagating waves and surface waves," Nat. Mater. **11**, 426–431 (2012).
214. X. Wan, Y. B. Li, B. G. Cai, and T. J. Cui, "Simultaneous controls of surface waves and propagating waves by metasurfaces," Appl. Phys. Lett. **105**, 121603 (2014).
215. J. Lin, Q. Wang, G. Yuan, L. Du, S. S. Kou, and X.-C. Yuan, "Mode-matching metasurfaces: coherent reconstruction and multiplexing of surface waves," Sci. Rep. **5**, 10529 (2015).
216. P. Genevet, D. Wintz, A. Ambrosio, A. She, R. Blanchard, and F. Capasso, "Controlled steering of Cherenkov surface plasmon wakes with a one-dimensional metamaterial," Nat. Nanotechnol. **10**, 804–809 (2015).
217. P. A. Huidobro, M. L. Nesterov, L. Martín-Moreno, and F. J. García-Vidal, "Transformation optics for plasmonics," Nano Lett. **10**, 1985–1990 (2010).
218. Y. Liu, T. Zentgraf, G. Bartal, and X. Zhang, "Transformational plasmon optics," Nano Lett. **10**, 1991–1997 (2010).
219. T. Zentgraf, Y. Liu, M. H. Mikkelsen, J. Valentine, and X. Zhang, "Plasmonic Luneburg and Eaton lenses," Nat. Nanotechnol. **6**, 151–155 (2011).
220. A. A. Orlov, S. V. Zhukovsky, I. V. Iorsh, and P. A. Belov, "Controlling light with plasmonic multilayers," Photon. Nanostruct. **12**, 213–230 (2014).
221. Z. Jacob, J.-Y. Kim, G. V. Naik, A. Boltasseva, E. E. Narimanov, and V. M. Shalaev, "Engineering photonic density of states using metamaterials," Appl. Phys. B **100**, 215–218 (2010).
222. C. Wang, P. Gao, X. Tao, Z. Zhao, M. Pu, P. Chen, and X. Luo, "Far field observation and theoretical analyses of light directional imaging in metamaterial with stacked metal-dielectric films," Appl. Phys. Lett. **103**, 031911 (2013).
223. A. A. High, R. C. Devlin, A. Dibos, M. Polking, D. S. Wild, J. Perczel, N. P. de Leon, M. D. Lukin, and H. Park, "Visible-frequency hyperbolic metasurface," Nature **522**, 192–196 (2015).
224. W. Kong, W. Du, K. Liu, C. Wang, L. Liu, Z. Zhao, and X. Luo, "Launching deep subwavelength bulk plasmon polaritons through hyperbolic metamaterials for surface imaging with a tuneable ultra-short illumination depth," Nanoscale **8**, 17030–17038 (2016).
225. W. Kong, W. Du, K. Liu, H. Liu, Z. Zhao, M. Pu, C. Wang, and X. Luo, "Surface imaging microscopy with tunable penetration depth as short as 20 nm by employing hyperbolic metamaterials," J. Mater. Chem. C **6**, 1797–1805 (2018).
226. A. Salandrino and N. Engheta, "Far-field subdiffraction optical microscopy using metamaterial crystals: theory and simulations," Phys. Rev. B **74**, 075103 (2006).
227. Z. Jacob, L. V. Alekseyev, and E. Narimanov, "Optical hyperlens: far-field imaging beyond the diffraction limit," Opt. Express **14**, 8247–8256 (2006).
228. J. Rho, Z. Ye, Y. Xiong, X. Yin, Z. Liu, H. Choi, G. Bartal, and X. Zhang, "Spherical hyperlens for two-dimensional sub-diffractional imaging at visible frequencies," Nat. Commun. **1**, 143 (2010).
229. Y. Xiong, Z. Liu, and X. Zhang, "A simple design of flat hyperlens for lithography and imaging with half-pitch resolution down to 20 nm," Appl. Phys. Lett. **94**, 203108 (2009).
230. G. Ren, C. Wang, G. Yi, X. Tao, and X. Luo, "Subwavelength demagnification imaging and lithography using hyperlens with a plasmonic reflector layer," Plasmonics **8**, 1065–1072 (2013).

231. B. H. Cheng, Y.-C. Lan, and D. P. Tsai, "Breaking optical diffraction limitation using optical hybrid-super-hyperlens with radially polarized light," Opt. Express **21**, 14898–14906 (2013).
232. B. H. Cheng, Y. Z. Ho, Y. C. Lan, and D. P. Tsai, "Optical hybrid-superlens hyperlens for superresolution imaging," IEEE J. Sel. Top. Quantum Electron. **19**, 4601305 (2013).
233. X. Tao, C. Wang, Z. Zhao, Y. Wang, N. Yao, and X. Luo, "A method for uniform demagnification imaging beyond the diffraction limit: cascaded planar hyperlens," Appl. Phys. B **114**, 545–550 (2014).
234. X. Yang, J. Yin, G. Yu, L. Peng, and N. Wang, "Acoustic superlens using Helmholtz-resonator-based metamaterials," Appl. Phys. Lett. **107**, 193505 (2015).
235. X. Ao and C. T. Chan, "Far-field image magnification for acoustic waves using anisotropic acoustic metamaterials," Phys. Rev. E **77**, 025601 (2008).
236. N. Kaina, F. Lemoult, M. Fink, and G. Lerosey, "Negative refractive index and acoustic superlens from multiple scattering in single negative metamaterials," Nature **525**, 77–81 (2015).
237. J. Li, L. Fok, X. Yin, G. Bartal, and X. Zhang, "Experimental demonstration of an acoustic magnifying hyperlens," Nat. Mater. **8**, 931–934 (2009).
238. T. Xu, A. Agrawal, M. Abashin, K. J. Chau, and H. J. Lezec, "All-angle negative refraction and active flat lensing of ultraviolet light," Nature **497**, 470–474 (2013).
239. R. Maas, E. Verhagen, J. Parsons, and A. Polman, "Negative refractive index and higher-order harmonics in layered metallodielectric optical metamaterials," ACS Photon. **1**, 670–676 (2014).
240. W. Woltersdorff, "Über die optischen Konstanten dünner Metallschichten im langwelligen ultrarot," Z. Für Phys. Hadrons Nucl. **91**, 230–252 (1934).
241. S. Li, J. Luo, S. Anwar, S. Li, W. Lu, Z. H. Hang, Y. Lai, B. Hou, M. Shen, and C. Wang, "Broadband perfect absorption of ultrathin conductive films with coherent illumination: superabsorption of microwave radiation," Phys. Rev. B **91**, 220301 (2015).
242. S. Li, Q. Duan, S. Li, Q. Yin, W. Lu, L. Li, B. Gu, B. Hou, and W. Wen, "Perfect electromagnetic absorption at one-atom-thick scale," Appl. Phys. Lett. **107**, 181112 (2015).
243. C. Yan, M. Pu, J. Luo, Y. Huang, X. Li, X. Ma, and X. Luo, "Coherent perfect absorption of electromagnetic wave in subwavelength structures," Opt. Laser Technol. **101**, 499–506 (2018).
244. M. Hong, "Metasurface wave in planar nano-photonics," Sci. Bull. **61**(2), 112–113 (2016).
245. K. N. Rozanov, "Ultimate thickness to bandwidth ratio of radar absorbers," IEEE Trans. Antennas Propag. **48**, 1230–1234 (2000).
246. M. Pu, Q. Feng, C. Hu, and X. Luo, "Perfect absorption of light by coherently induced plasmon hybridization in ultrathin metamaterial film," Plasmonics **7**, 733–738 (2012).
247. A. Kohiyama, M. Shimizu, and H. Yugami, "Unidirectional radiative heat transfer with a spectrally selective planar absorber/emitter for high-efficiency solar thermophotovoltaic systems," Appl. Phys. Express **9**, 112302 (2016).
248. M. Papaioannou, E. Plum, J. Valente, E. T. F. Rogers, and N. I. Zheludev, "Two-dimensional control of light with light on metasurfaces," Light Sci. Appl. **5**, e16070 (2016).
249. H. Noh, S. M. Popoff, and H. Cao, "Broadband subwavelength focusing of light using a passive sink," Opt. Express **21**, 17435–17446 (2013).

250. Z. J. Wong, Y.-L. Xu, J. Kim, K. O'Brien, Y. Wang, L. Feng, and X. Zhang, "Lasing and anti-lasing in a single cavity," Nat. Photonics **10**, 796–801 (2016).
251. M. A. Kats, R. Blanchard, P. Genevet, and F. Capasso, "Nanometre optical coatings based on strong interference effects in highly absorbing media," Nat. Mater. **12**, 20–24 (2013).
252. M. A. Kats, D. Sharma, J. Lin, P. Genevet, R. Blanchard, Z. Yang, M. M. Qazilbash, D. N. Basov, S. Ramanathan, and F. Capasso, "Ultra-thin perfect absorber employing a tunable phase change material," Appl. Phys. Lett. **101**, 221101 (2012).
253. P. Hosseini, C. D. Wright, and H. Bhaskaran, "An optoelectronic framework enabled by low-dimensional phase change films," Nature **511**, 206–211 (2014).
254. M. A. Kats and F. Capasso, "Optical absorbers based on strong interference in ultra-thin films," Laser Photon. Rev. **10**, 735–749 (2016).
255. A. Y. Vorobyev and C. Guo, "Colorizing metals with femtosecond laser pulses," Appl. Phys. Lett. **92**, 041914 (2008).
256. B. A. Munk, P. Munk, and J. Pryor, "On designing Jaumann and circuit analog absorbers (CA absorbers) for oblique angle of incidence," IEEE Trans. Antennas Propag. **55**, 186–193 (2007).
257. T. D. Dao, K. Chen, S. Ishii, A. Ohi, T. Nabatame, M. Kitajima, and T. Nagao, "Infrared perfect absorbers fabricated by colloidal mask etching of Al-Al_2O_3–Al trilayers," ACS Photon. **2**, 964–970 (2015).
258. M. Choi, S. H. Lee, Y. Kim, S. B. Kang, J. Shin, M. H. Kwak, K.-Y. Kang, Y.-H. Lee, N. Park, and B. Min, "A terahertz metamaterial with unnaturally high refractive index," Nature **470**, 369–373 (2011).
259. A. P. Raman, M. A. Anoma, L. Zhu, E. Rephaeli, and S. Fan, "Passive radiative cooling below ambient air temperature under direct sunlight," Nature **515**, 540–544 (2014).
260. Y. Huang, M. Pu, P. Gao, Z. Zhao, X. Li, X. Ma, and X. Luo, "Ultra-broadband large-scale infrared perfect absorber with optical transparency," Appl. Phys. Express **10**, 112601 (2017).
261. L. Zhu, A. P. Raman, and S. Fan, "Radiative cooling of solar absorbers using a visibly transparent photonic crystal thermal blackbody," Proc. Natl. Acad. Sci. USA **112**, 12282–12287 (2015).
262. T. Xu, Y.-K. Wu, X. Luo, and L. J. Guo, "Plasmonic nanoresonators for high-resolution colour filtering and spectral imaging," Nat. Commun. **1**, 59 (2010).
263. K. Kumar, H. Duan, R. S. Hegde, S. C. W. Koh, J. N. Wei, and J. K. W. Yang, "Printing colour at the optical diffraction limit," Nat. Nanotechnol. **7**, 557–561 (2012).
264. M. Song, X. Li, M. Pu, Y. Guo, K. Liu, H. Yu, X. Ma, and X. Luo, "Color display and encryption with a plasmonic polarizing metamirror," Nanophotonics **7**, 323–331 (2018).
265. C. M. Watts, X. Liu, and W. J. Padilla, "Metamaterial electromagnetic wave absorbers," Adv. Mater. **24**, OP98–OP120 (2012).
266. S. A. Tretyakov and S. I. Maslovski, "Thin absorbing structure for all incidence angles based on the use of a high-impedance surface," Microw. Opt. Technol. Lett. **38**, 175–178 (2003).
267. N. I. Landy, S. Sajuyigbe, J. J. Mock, D. R. Smith, and W. J. Padilla, "Perfect metamaterial absorber," Phys. Rev. Lett. **100**, 207402 (2008).
268. V.-C. Su, C. H. Chu, G. Sun, and D. P. Tsai, "Advances in optical metasurfaces: fabrication and applications [Invited]," Opt. Express **26**, 13148–13182 (2018).

269. P. Zijlstra, J. W. M. Chon, and M. Gu, "Five-dimensional optical recording mediated by surface plasmons in gold nanorods," Nature **459**, 410–413 (2009).
270. K. Aydin, V. E. Ferry, R. M. Briggs, and H. A. Atwater, "Broadband polarization-independent resonant light absorption using ultrathin plasmonic super absorbers," Nat. Commun. **2**, 517 (2011).
271. Y. Q. Ye, Y. Jin, and S. He, "Omnidirectional, polarization-insensitive and broadband thin absorber in the terahertz regime," J. Opt. Soc. Am. B **27**, 498–504 (2010).
272. J. Sun, L. Liu, G. Dong, and J. Zhou, "An extremely broad band metamaterial absorber based on destructive interference," Opt. Express **19**, 21155–21162 (2011).
273. M. Song, H. Yu, C. Hu, M. Pu, Z. Zhang, J. Luo, and X. Luo, "Conversion of broadband energy to narrowband emission through double-sided metamaterials," Opt. Express **21**, 32207–32216 (2013).
274. C. Long, S. Yin, W. Wang, W. Li, J. Zhu, and J. Guan, "Broadening the absorption bandwidth of metamaterial absorbers by transverse magnetic harmonics of 210 mode," Sci. Rep. **6**, 21431 (2016).
275. A. Vora, J. Gwamuri, N. Pala, A. Kulkarni, J. M. Pearce, and D. Ö. Güney, "Exchanging ohmic losses in metamaterial absorbers with useful optical absorption for photovoltaics," Sci. Rep. **4**, 4901 (2014).
276. J. A. Bossard, L. Lin, S. Yun, L. Liu, D. H. Werner, and T. S. Mayer, "Near-ideal optical metamaterial absorbers with super-octave bandwidth," ACS Nano **8**, 1517–1524 (2014).
277. C. Shi, X. Zang, Y. Wang, L. Chen, B. Cai, and Y. Zhu, "A polarization-independent broadband terahertz absorber," Appl. Phys. Lett. **105**, 031104 (2014).
278. S. Yin, J. Zhu, W. Xu, W. Jiang, J. Yuan, G. Yin, L. Xie, Y. Ying, and Y. Ma, "High-performance terahertz wave absorbers made of silicon-based metamaterials," Appl. Phys. Lett. **107**, 073903 (2015).
279. X. Zang, C. Shi, L. Chen, B. Cai, Y. Zhu, and S. Zhuang, "Ultra-broadband terahertz absorption by exciting the orthogonal diffraction in dumbbell-shaped gratings," Sci. Rep. **5**, 8091 (2015).
280. L. Zhang, P. Zhou, H. Chen, H. Lu, J. Xie, and L. Deng, "Adjustable wideband reflective converter based on cut-wire metasurface," J. Opt. **17**, 105105 (2015).
281. G. Zheng, H. Mühlenbernd, M. Kenney, G. Li, and S. Zhang, "Metasurface holograms reaching 80% efficiency," Nat. Nanotechnol. **10**, 308–312 (2015).
282. R.-S. Chu and K.-M. Lee, "Analytical method of a multilayered meander-line polarizer plate with normal and oblique plane-wave incidence," IEEE Trans. Antennas Propag. **35**, 652–661 (1987).
283. Y.-J. Jen, A. Lakhtakia, C.-W. Yu, C.-F. Lin, M.-J. Lin, S.-H. Wang, and J.-R. Lai, "Biologically inspired achromatic waveplates for visible light," Nat. Commun. **2**, 363 (2011).
284. J. Hao, Q. Ren, Z. An, X. Huang, Z. Chen, M. Qiu, and L. Zhou, "Optical metamaterial for polarization control," Phys. Rev. A **80**, 023807 (2009).
285. A. Pors, M. G. Nielsen, G. D. Valle, M. Willatzen, O. Albrektsen, and S. I. Bozhevolnyi, "Plasmonic metamaterial wave retarders in reflection by orthogonally oriented detuned electrical dipoles," Opt. Lett. **36**, 1626–1628 (2011).
286. Y. Yang, W. Wang, P. Moitra, I. I. Kravchenko, D. P. Briggs, and J. Valentine, "Dielectric meta-reflectarray for broadband linear polarization conversion and optical vortex generation," Nano Lett. **14**, 1394–1399 (2014).
287. G. Nordin and P. Deguzman, "Broadband form birefringent quarter-wave plate for the mid-infrared wavelength region," Opt. Express **5**, 163–168 (1999).

288. H. F. Ma, G. Z. Wang, G. S. Kong, and T. J. Cui, "Broadband circular and linear polarization conversions realized by thin birefringent reflective metasurfaces," Opt. Mater. Express **4**, 1717–1724 (2014).
289. S.-C. Jiang, X. Xiong, Y.-S. Hu, Y.-H. Hu, G.-B. Ma, R.-W. Peng, C. Sun, and M. Wang, "Controlling the polarization state of light with a dispersion-free metastructure," Phys. Rev. X **4**, 021026 (2014).
290. J. Cui, C. Huang, W. Pan, M. Pu, Y. Guo, and X. Luo, "Dynamical manipulation of electromagnetic polarization using anisotropic meta-mirror," Sci. Rep. **6**, 30771 (2016).
291. S. Zhang, J. Zhou, Y.-S. Park, J. Rho, R. Singh, S. Nam, A. K. Azad, H.-T. Chen, X. Yin, A. J. Taylor, and X. Zhang, "Photoinduced handedness switching in terahertz chiral metamolecules," Nat. Commun. **3**, 942 (2012).
292. J. B. Pendry, "A chiral route to negative refraction," Science **306**, 1353–1355 (2004).
293. Y. Tang and A. E. Cohen, "Enhanced enantioselectivity in excitation of chiral molecules by superchiral light," Science **332**, 333–336 (2011).
294. M. Hentschel, M. Schäferling, X. Duan, H. Giessen, and N. Liu, "Chiral plasmonics," Sci. Adv. **3**, e1602735 (2017).
295. J. K. Gansel, M. Thiel, M. S. Rill, M. Decker, K. Bade, V. Saile, G. von Freymann, S. Linden, and M. Wegener, "Gold helix photonic metamaterial as broadband circular polarizer," Science **325**, 1513–1515 (2009).
296. S. Kawata, H. Sun, T. Tanaka, and K. Takada, "Finer features for functional microdevices," Nature **412**, 697–698 (2001).
297. Y. Zhao, M. A. Belkin, and A. Alù, "Twisted optical metamaterials for planarized ultrathin broadband circular polarizers," Nat. Commun. **3**, 870 (2012).
298. X. Ma, C. Huang, M. Pu, C. Hu, Q. Feng, and X. Luo, "Multi-band circular polarizer using planar spiral metamaterial structure," Opt. Express **20**, 16050–16058 (2012).
299. X. Ma, C. Huang, M. Pu, Y. Wang, Z. Zhao, C. Wang, and X. Luo, "Dual-band asymmetry chiral metamaterial based on planar spiral structure," Appl. Phys. Lett. **101**, 161901 (2012).
300. J. Kaschke and M. Wegener, "Gold triple-helix mid-infrared metamaterial by STED-inspired laser lithography," Opt. Lett. **40**, 3986–3989 (2015).
301. Y. Cui, L. Kang, S. Lan, S. Rodrigues, and W. Cai, "Giant chiral optical response from a twisted-arc metamaterial," Nano Lett. **14**, 1021–1025 (2014).
302. S. P. Rodrigues, S. Lan, L. Kang, Y. Cui, and W. Cai, "Nonlinear imaging and spectroscopy of chiral metamaterials," Adv. Mater. **26**, 6157–6162 (2014).
303. M. Saba, M. Thiel, M. D. Turner, S. T. Hyde, M. Gu, K. Grosse-Brauckmann, D. N. Neshev, K. Mecke, and G. E. Schröder-Turk, "Circular dichroism in biological photonic crystals and cubic chiral nets," Phys. Rev. Lett. **106**, 103902 (2011).
304. K. Robbie, M. J. Brett, and A. Lakhtakia, "Chiral sculptured thin films," Nature **384**, 616 (1996).
305. F. Capasso, "The future and promise of flat optics: a personal perspective," Nanophotonics **7**, 953–957 (2018).
306. M. L. Tseng, H.-H. Hsiao, C. H. Chu, M. K. Chen, G. Sun, A.-Q. Liu, and D. P. Tsai, "Metalenses: advances and applications," Adv. Opt. Mater. **6**, 1800554 (2018).
307. F. Aieta, M. A. Kats, P. Genevet, and F. Capasso, "Multiwavelength achromatic metasurfaces by dispersive phase compensation," Science **347**, 1342–1345 (2015).
308. Z.-L. Deng, S. Zhang, and G. P. Wang, "Wide-angled off-axis achromatic metasurfaces for visible light," Opt. Express **24**, 23118–23128 (2016).

309. M. Khorasaninejad, F. Aieta, P. Kanhaiya, M. A. Kats, P. Genevet, D. Rousso, and F. Capasso, "Achromatic metasurface lens at telecommunication wavelengths," Nano Lett. **15**, 5358–5362 (2015).
310. M. Khorasaninejad, Z. Shi, A. Y. Zhu, W. T. Chen, V. Sanjeev, A. Zaidi, and F. Capasso, "Achromatic metalens over 60 nm bandwidth in the visible and metalens with reverse chromatic dispersion," Nano Lett. **17**, 1819–1824 (2017).
311. S. Wang, P. C. Wu, V.-C. Su, Y.-C. Lai, C. H. Chu, J.-W. Chen, S.-H. Lu, J. Chen, B. Xu, C.-H. Kuan, T. Li, S. Zhu, and D. P. Tsai, "Broadband achromatic optical metasurface devices," Nat. Commun. **8**, 187 (2017).
312. H. Hsiao, Y. H. Chen, R. J. Lin, P. C. Wu, S. Wang, B. H. Chen, and D. P. Tsai, "Integrated resonant unit of metasurfaces for broadband efficiency and phase manipulation," Adv. Opt. Mater. **6**, 1800031 (2018).
313. W. T. Chen, A. Y. Zhu, V. Sanjeev, M. Khorasaninejad, Z. Shi, E. Lee, and F. Capasso, "A broadband achromatic metalens for focusing and imaging in the visible," Nat. Nanotechnol. **13**, 220–226 (2018).
314. F. Aieta, P. Genevet, M. Kats, and F. Capasso, "Aberrations of flat lenses and aplanatic metasurfaces," Opt. Express **21**, 31530–31539 (2013).
315. A. Kalvach and Z. Szabó, "Aberration-free flat lens design for a wide range of incident angles," J. Opt. Soc. Am. B **33**, A66–A71 (2016).
316. M. Born and E. Wolf, *Principles of Optics: Electromagnetic Theory of Propagation, Interference and Diffraction of Light*, 7th ed. (Cambridge University, 1999).
317. D. R. Smith, S. Schultz, P. Markoš, and C. M. Soukoulis, "Determination of effective permittivity and permeability of metamaterials from reflection and transmission coefficients," Phys. Rev. B **65**, 195104 (2002).
318. H. Ma and T. Cui, "Three-dimensional broadband and broad-angle transformation-optics lens," Nat. Commun. **1**, 124 (2010).
319. Y.-Y. Zhao, Y.-L. Zhang, M.-L. Zheng, X.-Z. Dong, X.-M. Duan, and Z.-S. Zhao, "Three-dimensional Luneburg lens at optical frequencies," Laser Photon. Rev. **10**, 665–672 (2016).
320. N. Kundtz and D. R. Smith, "Extreme-angle broadband metamaterial lens," Nat. Mater. **9**, 129–132 (2010).
321. J. Hunt, T. Tyler, S. Dhar, Y.-J. Tsai, P. Bowen, S. Larouche, N. M. Jokerst, and D. R. Smith, "Planar, flattened Luneburg lens at infrared wavelengths," Opt. Express **20**, 1706–1713 (2012).
322. A. Arbabi, E. Arbabi, S. M. Kamali, Y. Horie, S. Han, and A. Faraon, "Miniature optical planar camera based on a wide-angle metasurface doublet corrected for monochromatic aberrations," Nat. Commun. **7**, 13682 (2016).
323. B. Groever, W. T. Chen, and F. Capasso, "Meta-lens doublet in the visible region," Nano Lett. **17**, 4902–4907 (2017).
324. T. Gissibl, S. Thiele, A. Herkommer, and H. Giessen, "Two-photon direct laser writing of ultracompact multi-lens objectives," Nat. Photonics **10**, 554–560 (2016).
325. M. Pu, X. Li, Y. Guo, X. Ma, and X. Luo, "Nanoapertures with ordered rotations: symmetry transformation and wide-angle flat lensing," Opt. Express **25**, 31471–31477 (2017).
326. W. Liu, Z. Li, H. Cheng, C. Tang, J. Li, S. Zhang, S. Chen, and J. Tian, "Metasurface enabled wide-angle Fourier lens," Adv. Mater. **30**, 1706368 (2018).
327. Y. Guo, X. Ma, M. Pu, X. Li, Z. Zhao, and X. Luo, "High-efficiency and wide-angle beam steering based on catenary optical fields in ultrathin metalens," Adv. Opt. Mater. **6**, 1800592 (2018).

328. L. B. Lesem, P. M. Hirsch, and J. A. Jordan, "The kinoform: a new wavefront reconstruction device," IBM J. Res. Dev. **13**, 150–155 (1969).
329. B. R. Brown and A. W. Lohmann, "Computer-generated binary holograms," IBM J. Res. Dev. **13**, 160–168 (1969).
330. C. Min, J. Liu, T. Lei, G. Si, Z. Xie, J. Lin, L. Du, and X. Yuan, "Plasmonic nano-slits assisted polarization selective detour phase meta-hologram," Laser Photon. Rev. **10**, 978–985 (2016).
331. M. Khorasaninejad, A. Ambrosio, P. Kanhaiya, and F. Capasso, "Broadband and chiral binary dielectric meta-holograms," Sci. Adv. **2**, e1501258 (2016).
332. Y.-W. Huang, W. T. Chen, W.-Y. Tsai, P. C. Wu, C.-M. Wang, G. Sun, and D. P. Tsai, "Aluminum plasmonic multicolor meta-hologram," Nano Lett. **15**, 3122–3127 (2015).
333. A. Pors, M. G. Nielsen, R. L. Eriksen, and S. I. Bozhevolnyi, "Broadband focusing flat mirrors based on plasmonic gradient metasurfaces," Nano Lett. **13**, 829–834 (2013).
334. X. Li, H. Ren, X. Chen, J. Liu, Q. Li, C. Li, G. Xue, J. Jia, L. Cao, A. Sahu, B. Hu, Y. Wang, G. Jin, and M. Gu, "Athermally photoreduced graphene oxides for three-dimensional holographic images," Nat. Commun. **6**, 6984 (2015).
335. E. Almeida, G. Shalem, and Y. Prior, "Subwavelength nonlinear phase control and anomalous phase matching in plasmonic metasurfaces," Nat. Commun. **7**, 10367 (2016).
336. G. Li, S. Chen, N. Pholchai, B. Reineke, P. W. H. Wong, E. Y. B. Pun, K. W. Cheah, T. Zentgraf, and S. Zhang, "Continuous control of the nonlinearity phase for harmonic generations," Nat. Mater. **14**, 607–612 (2015).
337. W. Ye, F. Zeuner, X. Li, B. Reineke, S. He, C.-W. Qiu, J. Liu, Y. Wang, S. Zhang, and T. Zentgraf, "Spin and wavelength multiplexed nonlinear metasurface holography," Nat. Commun. **7**, 11930 (2016).
338. S. Franke-Arnold, L. Allen, and M. Padgett, "Advances in optical angular momentum," Laser Photon. Rev. **2**, 299–313 (2008).
339. R. A. Beth, "Mechanical detection and measurement of the angular momentum of light," Phys. Rev. **50**, 115–125 (1936).
340. L. Allen, M. W. Beijersbergen, R. J. C. Spreeuw, and J. P. Woerdman, "Orbital angular-momentum of light and the transformation of Laguerre-Gaussian laser modes," Phys. Rev. A **45**, 8185–8189 (1992).
341. F. Tamburini, G. Anzolin, G. Umbriaco, A. Bianchini, and C. Barbieri, "Overcoming the Rayleigh criterion limit with optical vortices," Phys. Rev. Lett. **97**, 163903 (2006).
342. K. Dholakia, P. Reece, and M. Gu, "Optical micromanipulation," Chem. Soc. Rev. **37**, 42–55 (2008).
343. N. Bozinovic, Y. Yue, Y. Ren, M. Tur, P. Kristensen, H. Huang, A. E. Willner, and S. Ramachandran, "Terabit-scale orbital angular momentum mode division multiplexing in fibers," Science **340**, 1545–1548 (2013).
344. M. P. J. Lavery, F. C. Speirits, S. M. Barnett, and M. J. Padgett, "Detection of a spinning object using light's orbital angular momentum," Science **341**, 537–540 (2013).
345. A. E. Willner, H. Huang, Y. Yan, Y. Ren, N. Ahmed, G. Xie, C. Bao, L. Li, Y. Cao, Z. Zhao, J. Wang, M. P. J. Lavery, M. Tur, S. Ramachandran, A. F. Molisch, N. Ashrafi, and S. Ashrafi, "Optical communications using orbital angular momentum beams," Adv. Opt. Photon. **7**, 66–106 (2015).
346. H. Liu, M. Q. Mehmood, K. Huang, L. Ke, H. Ye, P. Genevet, M. Zhang, A. Danner, S. P. Yeo, C.-W. Qiu, and J. Teng, "Twisted focusing of optical vortices with broadband flat spiral zone plates," Adv. Opt. Mater. **2**, 1193–1198 (2014).

347. J. Zeng, L. Li, X. Yang, and J. Gao, "Generating and separating twisted light by gradient-rotation split-ring antenna metasurfaces," Nano Lett. **16**, 3101–3108 (2016).
348. Y. Li, X. Li, L. Chen, M. Pu, J. Jin, M. Hong, and X. Luo, "Orbital angular momentum multiplexing and demultiplexing by a single metasurface," Adv. Opt. Mater. **5**, 1600502 (2017).
349. H. Ren, X. Li, Q. Zhang, and M. Gu, "On-chip noninterference angular momentum multiplexing of broadband light," Science **352**, 805–809 (2016).
350. K. Y. Bliokh, "Geometrical optics of beams with vortices: Berry phase and orbital angular momentum Hall effect," Phys. Rev. Lett. **97**, 043901 (2006).
351. K. Y. Bliokh, Y. Gorodetski, V. Kleiner, and E. Hasman, "Coriolis effect in optics: unified geometric phase and spin-Hall effect," Phys. Rev. Lett. **101**, 030404 (2008).
352. G. Yuan, X.-C. Yuan, J. Bu, P. S. Tan, and Q. Wang, "Manipulation of surface plasmon polaritons by phase modulation of incident light," Opt. Express **19**, 224–229 (2011).
353. J. Durnin, "Exact solutions for nondiffracting beams. I. The scalar theory," J. Opt. Soc. Am. A **4**, 651–654 (1987).
354. C. Snoeyink and S. Wereley, "Single-image far-field subdiffraction limit imaging with axicon," Opt. Lett. **38**, 625–627 (2013).
355. H. Gao, M. Pu, X. Li, X. Ma, Z. Zhao, Y. Guo, and X. Luo, "Super-resolution imaging with a Bessel lens realized by a geometric metasurface," Opt. Express **25**, 13933–13943 (2017).
356. K. Lindfors, D. Dregely, M. Lippitz, N. Engheta, M. Totzeck, and H. Giessen, "Imaging and steering unidirectional emission from nanoantenna array metasurfaces," ACS Photon. **3**, 286–292 (2016).
357. J. P. Balthasar Mueller, N. A. Rubin, R. C. Devlin, B. Groever, and F. Capasso, "Metasurface polarization optics: independent phase control of arbitrary orthogonal states of polarization," Phys. Rev. Lett. **118**, 113901 (2017).
358. F. Zhang, M. Pu, J. Luo, H. Yu, and X. Luo, "Symmetry breaking of photonic spin-orbit interactions in metasurfaces," Opto-Electron. Eng. **44**, 319–325 (2017).
359. Q. Tan, Q. Guo, H. Liu, X. Huang, and S. Zhang, "Controlling the plasmonic orbital angular momentum by combining the geometric and dynamic phases," Nanoscale **9**, 4944–4949 (2017).
360. A. Shaltout, J. Liu, V. M. Shalaev, and A. V. Kildishev, "Optically active metasurface with non-chiral plasmonic nanoantennas," Nano Lett. **14**, 4426–4431 (2014).
361. N. Yu, F. Aieta, P. Genevet, M. A. Kats, Z. Gaburro, and F. Capasso, "A broadband, background-free quarter-wave plate based on plasmonic metasurfaces," Nano Lett. **12**, 6328–6333 (2012).
362. P. C. Wu, W.-Y. Tsai, W. T. Chen, Y.-W. Huang, T.-Y. Chen, J.-W. Chen, C. Y. Liao, C. H. Chu, G. Sun, and D. P. Tsai, "Versatile polarization generation with an aluminum plasmonic metasurface," Nano Lett. **17**, 445–452 (2017).
363. J. P. Balthasar Mueller, K. Leosson, and F. Capasso, "Ultracompact metasurface in-line polarimeter," Optica **3**, 42–47 (2016).
364. F. Ding, A. Pors, Y. Chen, V. A. Zenin, and S. I. Bozhevolnyi, "Beam-size-invariant spectropolarimeters using gap-plasmon metasurfaces," ACS Photon. **4**, 943–949 (2017).
365. J. R. Swandic, *Bandwidth Limits and Other Considerations for Monostatic RCS Reduction by Virtual Shaping* (Naval Surface Warfare Center, 2004).

366. J. B. Pendry, D. Schurig, and D. R. Smith, "Controlling electromagnetic fields," Science **312**, 1780–1782 (2006).
367. J. Li and J. B. Pendry, "Hiding under the carpet: a new strategy for cloaking," Phys. Rev. Lett. **101**, 203901 (2008).
368. X. Luo, M. Pu, X. Ma, and X. Li, "Taming the electromagnetic boundaries via metasurfaces: from theory and fabrication to functional devices," Int. J. Antennas Propag. **2015**, 204127 (2015).
369. C. J. David, *Radar and Laser Cross Section Engineering*, 2nd ed. (AIAA, 2005).
370. E. Doumanis, G. Goussetis, G. Papageorgiou, V. Fusco, R. Cahill, and D. Linton, "Design of engineered reflectors for radar cross section modification," IEEE Trans. Antennas Propag. **61**, 232–239 (2013).
371. X. Ni, Z. J. Wong, M. Mrejen, Y. Wang, and X. Zhang, "An ultrathin invisibility skin cloak for visible light," Science **349**, 1310–1314 (2015).
372. S. M. Kamali, A. Arbabi, E. Arbabi, and A. Faraon, "Decoupling optical function and geometrical form using conformal flexible dielectric metasurfaces," Nat. Commun. **7**, 11618 (2016).
373. B. Zhao and J. Yang, "New effects in an ultracompact Young's double nanoslit with plasmon hybridization," New J. Phys. **15**, 073024 (2013).
374. R. Zia and M. L. Brongersma, "Surface plasmon polariton analogue to Young's double-slit experiment," Nat. Nanotechnol. **2**, 426–429 (2007).
375. T. Yang, X. Bai, D. Gao, L. Wu, B. Li, J. T. L. Thong, and C.-W. Qiu, "Invisible sensors: simultaneous sensing and camouflaging in multiphysical fields," Adv. Mater. **27**, 7752–7758 (2015).
376. Z. Zhao, M. Pu, H. Gao, J. Jin, X. Li, X. Ma, Y. Wang, P. Gao, and X. Luo, "Multispectral optical metasurfaces enabled by achromatic phase transition," Sci. Rep. **5**, 15781 (2015).
377. C. Min, P. Wang, X. Jiao, Y. Deng, and H. Ming, "Beam manipulating by metallic nano-optic lens containing nonlinear media," Opt. Express **15**, 9541–9546 (2007).
378. Y. Chen, X. Li, Y. Sonnefraud, A. I. Fernández-Domínguez, X. Luo, M. Hong, and S. A. Maier, "Engineering the phase front of light with phase-change material based planar lenses," Sci. Rep. **5**, 8660 (2015).
379. Q. Wang, E. T. F. Rogers, B. Gholipour, C.-M. Wang, G. Yuan, J. Teng, and N. I. Zheludev, "Optically reconfigurable metasurfaces and photonic devices based on phase change materials," Nat. Photonics **10**, 60–65 (2016).
380. M. Zhang, M. Pu, F. Zhang, Y. Guo, Q. He, X. Ma, Y. Huang, X. Li, H. Yu, and X. Luo, "Plasmonic metasurfaces for switchable photonic spin-orbit interactions based on phase change materials," Adv. Sci. 1800835 (2018), doi: 10.1002/advs.201800835.
381. J. Hong, E. Chan, T. Chang, T.-C. Fung, B. Hong, C. Kim, J. Ma, Y. Pan, R. V. Lier, S. Wang, B. Wen, and L. Zhou, "Continuous color reflective displays using interferometric absorption," Optica **2**, 589–597 (2015).
382. E. Arbabi, A. Arbabi, S. M. Kamali, Y. Horie, M. Faraji-Dana, and A. Faraon, "MEMS-tunable dielectric metasurface lens," Nat. Commun. **9**, 812 (2018).
383. S. Song, X. Ma, M. Pu, X. Li, K. Liu, P. Gao, Z. Zhao, Y. Wang, C. Wang, and X. Luo, "Actively tunable structural color rendering with tensile substrate," Adv. Opt. Mater. **5**, 1600829 (2017).
384. C. Huang, W. Pan, X. Ma, B. Zhao, J. Cui, and X. Luo, "Using reconfigurable transmitarray to achieve beam-steering and polarization manipulation applications," IEEE Trans. Antennas Propag. **63**, 4801–4810 (2015).
385. A. Tennant and B. Chambers, "A single-layer tuneable microwave absorber using an active FSS," IEEE Microw. Wireless. Compon. Lett. **14**, 46–47 (2004).

386. A. Nemati, Q. Wang, M. Hong, and J. Teng, "Tunable and reconfigurable metasurfaces and metadevices," Opto-Electron. Adv. **1**, 18000901 (2018).
387. Y. Guo, M. Pu, X. Ma, X. Li, and X. Luo, "Advances of dispersion-engineered metamaterials," Opto-Electron. Eng. **44**, 3–22 (2017).
388. X. Li, M. Pu, X. Ma, Y. Guo, P. Gao, and X. Luo, "Dispersion engineering in metamaterials and metasurfaces," J. Phys. D **51**, 054002 (2018).
389. Z. Liu, D. Zhu, S. P. Rodrigues, K. T. Lee, and W. Cai, "A generative model for inverse design of metamaterials," arXiv: 180510181 (2018).

Prof. Xiangang Luo is currently the director of the State Key Laboratory of Optical Technologies on Nano-fabrication and Micro-engineering (SKLOTNM) in the Institute of Optics and Electronics (IOE), Chinese Academy of Sciences (CAS). He received his Ph.D. from the Chinese Academy of Sciences in 2001. He was a Research Scientist at The Institute of Physical and Chemical Research (RIKEN) of Japan. His research interests are micro/nano-optics, plasmonics, subwavelength electromagnetics, and catenary optics. He has published more than 300 scientific papers and 100 patents in optics and related fields. He is a Fellow of the Optical Society of America (OSA), the International Society for Optical Engineering (SPIE), and the International Academy of Photonics and Laser Engineering (IAPLE).

DinPing Tsai received his Ph.D. degree in Physics from the University of Cincinnati, USA, in 1990. He has been the Director and Distinguished Research Fellow of the Research Center for Applied Sciences, Academia Sinica, since 2012. He is also a Distinguished Professor of the Department of Physics at National Taiwan University. He is a Fellow of AAAS, APS, IEEE, JSAP, OSA, SPIE, and EMA. His current research interests are nano-photonics, plasmonics, meta-materials, green photonics, quantum photonics, and their applications.

Professor Min Gu is a Distinguished Professor and Associate Deputy Vice-Chancellor at RMIT University and was a Laureate Fellow of the Australian Research Council. He is an author of four standard reference books and has more than 500 publications in nano/biophotonics. He is an elected Fellow of the Australian Academy of Science and the Australian Academy of Technological Sciences and Engineering as well as Foreign Fellow of the Chinese Academy of Engineering. He is also an elected fellow of the AIP, the OSA, the SPIE, the InstP, and the IEEE. He was President of the International Society of Optics within Life Sciences, Vice President of the Board of the International Commission for Optics (ICO) (Chair of the ICO Prize Committee), and a Director of the Board of the Optical Society of America (Chair of the International Council). He was awarded the Einstein Professorship, the W. H. (Beattie) Steel Medal, the Ian Wark Medal, the Boas Medal, and the Victoria Prize for Science and Innovation.

Prof. Minghui Hong specializes in Laser Microprocessing and Nanofabrication, Optical Engineering, and Laser Applications. He has been a member of organizing committees for the Laser Precision Micromachining International Conference (2001–2019) and the International Symposium of Functional Materials (2005, 2007, and 2014), Chair of the International Workshop of Plasmonics and Applications in Nanotechnologies (2006), Chair of the Conference on Laser Ablation (2009), and Chair of the Asia-Pacific Near-Field Optics Conference (2013 and 2019). He has been invited to serve as an Editor of *Light: Science and Applications*, Associate Editor of *Science China G*, Editor of *Laser Micro/nanoengineering*, and Executive Editor-in-Chief of Opto-Electronic Advances. He is a Fellow of the Academy of Engineering, Singapore (FSEng), Fellow of the Optical Society of America (OSA), Fellow of the International Society for Optics and Photonics (SPIE), Fellow and Vice President of the International Academy of Photonics and Laser Engineering (IAPLE), and Fellow and Council Member of the Institute of Engineers, Singapore (IES). He is currently a Full Professor and the Director of the Optical Science and Engineering Centre (OSEC), Department of Electrical and Computer Engineering, National University of Singapore. He is also the Chairman of an NUS spin-off company, Phaos Technology Pte. Ltd.

159.226.167.12 (a 2021-12-10 05:02:30)